

1995

# Ultrasonic measurement of drawability (r-values) of low carbon steel sheets

Kaveh Forouraghi  
Iowa State University

Follow this and additional works at: <https://lib.dr.iastate.edu/rtd>

 Part of the [Mechanical Engineering Commons](#), and the [Metallurgy Commons](#)

## Recommended Citation

Forouraghi, Kaveh, "Ultrasonic measurement of drawability (r-values) of low carbon steel sheets " (1995). *Retrospective Theses and Dissertations*. 10903.

<https://lib.dr.iastate.edu/rtd/10903>

This Dissertation is brought to you for free and open access by the Iowa State University Capstones, Theses and Dissertations at Iowa State University Digital Repository. It has been accepted for inclusion in Retrospective Theses and Dissertations by an authorized administrator of Iowa State University Digital Repository. For more information, please contact [digirep@iastate.edu](mailto:digirep@iastate.edu).

## **INFORMATION TO USERS**

**This manuscript has been reproduced from the microfilm master. UMI films the text directly from the original or copy submitted. Thus, some thesis and dissertation copies are in typewriter face, while others may be from any type of computer printer.**

**The quality of this reproduction is dependent upon the quality of the copy submitted. Broken or indistinct print, colored or poor quality illustrations and photographs, print bleedthrough, substandard margins, and improper alignment can adversely affect reproduction.**

**In the unlikely event that the author did not send UMI a complete manuscript and there are missing pages, these will be noted. Also, if unauthorized copyright material had to be removed, a note will indicate the deletion.**

**Oversize materials (e.g., maps, drawings, charts) are reproduced by sectioning the original, beginning at the upper left-hand corner and continuing from left to right in equal sections with small overlaps. Each original is also photographed in one exposure and is included in reduced form at the back of the book.**

**Photographs included in the original manuscript have been reproduced xerographically in this copy. Higher quality 6" x 9" black and white photographic prints are available for any photographs or illustrations appearing in this copy for an additional charge. Contact UMI directly to order.**

# **UMI**

**A Bell & Howell Information Company  
300 North Zeeb Road, Ann Arbor, MI 48106-1346 USA  
313/761-4700 800/521-0600**



**Ultrasonic measurement of drawability (r-values) of low carbon steel sheets**

**by**

**Kaveh Forouraghi**

**A Dissertation Submitted to the  
Graduate Faculty in Partial Fulfillment of the  
Requirements for the Degree of  
DOCTOR OF PHILOSOPHY**

**Department: Mechanical Engineering  
Major: Mechanical Engineering**

**Approved:**

Signature was redacted for privacy.

Signature was redacted for privacy.

**In Charge of Major Work**

Signature was redacted for privacy.

**For the Major Department**

Signature was redacted for privacy.

**For the Graduate College**

**Iowa State University  
Ames, Iowa**

**1995**

---

**UMI Number: 9531739**

---

**UMI Microform 9531739**

**Copyright 1995, by UMI Company. All rights reserved.**

**This microform edition is protected against unauthorized  
copying under Title 17, United States Code.**

---

**UMI**

**300 North Zeeb Road  
Ann Arbor, MI 48103**

---

*I dedicate this work to my wife, Amy, for her unconditional love and unlimited patience; and,*

*In the memory of my brother, Farzam.*

*There was the Door to which I found no key;  
There was the Veil through which I might not see:  
Some little talk awhile of ME and THEE  
There was-and then, no more of THEE and ME.*

*Omar Khayyam  
(Rubaiyat)*

---

## TABLE OF CONTENTS

<b>CHAPTER 1. INTRODUCTION</b>	<b>1</b>
1.1 The Forming Process: Overview	3
1.2 The Forming process: Problems	5
1.3 Forming Properties of Steel	9
1.3.1 Stretchability Index: n-values	11
1.3.2 Drawability index: r-values	14
1.4 Ultrasonic Measurements of r-values: Ultra-Form	19
1.4.1 Review	19
1.4.2 Ultra-Form's Description	22
1.4.3 Other Recent Advances	24
1.5 The Present Research	24
<b>CHAPTER 2. LOW CARBON STEELS</b>	<b>28</b>
2.1 Steel Making and Mill Practices	32
2.1.1 Steel Making	32
2.1.2 Mill Practices	34
2.2 Preferred Orientation (Texture)	37
2.2.1 Texture Representation	37
2.2.2 Experimental Texture Analysis	42
2.2.3 Common Textures In Low Carbon Steels	55
<b>CHAPTER 3. DESTRUCTIVE R MEASUREMENT TECHNIQUES</b>	<b>62</b>
3.1 Tensile Test	62
3.1.1 Test Procedure	64

---

3.1.2 Factors Affecting Tensile Measurements of $r$	67
3.1.3 Limitations	71
3.2 Magnetostrictive Technique: Modul-r Instrument	74
3.2.1 The Procedure and the Equipment	74
3.2.2 Limitations	76
CHAPTER 4. ULTRASONIC MEASUREMENT OF DRAWABILITY	79
4.1 Theory	79
4.1.1 Series Expansion Technique	82
4.1.2 Calculation of Elastic Properties	87
4.1.3 Speed of Ultrasonic Waves and Texture	91
4.1.4 Calculation of Plastic Properties	98
CHAPTER 5. EXPERIMENTAL TECHNIQUES AND RESULTS	111
5.1 Approach	111
5.2 Steel Samples	112
5.3 Tensile Tests	118
5.4 Neutron Diffraction measurements	120
5.5 Ultrasonic Velocity Measurements	120
5.5.1 Selection of The Operating Frequency for the EMAT Transducers	120
5.5.2 The Signal processing Technique and The Dispersion Correction	124
5.5.3 Coating Effects	126
5.6 Repeatability Data	131
5.7 Experimental Correlations	134
5.8 Data on Elastic Anisotropy	139
5.8.1 Young's Modulus Predictions	139

---

5.8.2 Effects of Single Crystal Data	148
5.9 Data on Plastic Anisotropy	156
5.9.1 The RC Model	156
5.9.2 r-value Predictions and Ideal Orientations	161
5.9.3 The Effects of Higher Order ODC's in the Prediction of r-values	166
5.9.4 Comparison of The Experimental r-value Predictions with Tensile Results	173
5.9.5 Correlations between $C_6^{\mu\nu}(W_{6mn})$ and Tensile Data	182
 CHAPTER 6. CONCLUSIONS	 190
6.1 The Accuracy and Repeatability of Ultrasonic measurements	191
6.2 Sensitivity to the Microstructure (Texture)	192
6.3 The Factors that Affect Ultrasonic Predictions of Plastic Properties	193
6.3.1 Effects of Coatings	193
6.3.2 Effects of Accurate Set of Elastic Constants	193
6.3.3 Effects of Early Truncation of Higher Order ODC's	194
6.4 Choice of Modeling in Ultrasonic Prediction of Plastic Properties	195
 BIBLIOGRAPHY	 197

---

## ACKNOWLEDGMENTS

I am sincerely indebted to my major professor, Dr. R. B. Thompson for providing me an opportunity to work on this challenging and interesting task. He followed my progress with interest and gave me encouragement and valuable guidance throughout this work. I am grateful for his precise and thorough review of this thesis. I would also like to express appreciations to my co-major professors Drs. Scrutton and Molian for their support of this work. Dr. Scrutton enriched this research with numerous papers published by the previous researchers in this field. I am grateful for his generous efforts and his input. I would like to extend my appreciations to the members of my graduate committee, Drs. Izworski, Papadakis and Hall. I am indebted to Dr. Izworski for providing me a chance to visit the Dearborn Stamping Plant at Ford Motor Company and his valuable input regarding the practical industrial problems in the forming industry. I would also like to thank Dr. Papadakis for many useful discussions regarding the ultrasonic device, Ultra-Form.

I am greatly indebted to Dr. Fritz Reis at LTV Steel Company and Dr. Ming Shi at National Steel Corporation for providing the steel samples and the tensile data. I am also grateful for their most valuable discussions and ideas regarding this research.

I would like to express my appreciations to Drs. Okiishi and Bathi in Mechanical Engineering Department for their financial support of my graduate studies.

I would like to thank my wife, Amy, and my children, Aria, Farhad and Lailei for their patience and support.

I am indebted to my brother, Dr. Babak Forouraghi, for his constant encouragement throughout this research.

Finally, the last but not the least, to my parents, Ali and Homa, whose valuable support and encouragements have been the inspiration behind my graduate studies.

---

**ABSTRACT**

The present research was designed to evaluate an ultrasonic technique for measuring the drawability of low carbon steel sheets nondestructively. This technique, which uses electromagnetic acoustic transducers (EMAT's) is embodied in a fully automatic ultrasonic device called Ultra-Form, which was developed at Iowa State University (by the Center For Nondestructive Evaluation) in 1990. EMAT transducers generate the ultrasonic pulses in the sheet (without any need for a coupling medium) whose velocities are then related to the microstructural factors (crystallographic texture) that control drawability in rolled sheets. Drawability (usually interpreted by measuring r-values of low carbon steels) is an important property indicative of the formability of steel sheets used in the auto and appliance industries. It is measured by the destructive tension test which is sensitive to the experimental errors and is time consuming. From a quality control perspective, there is a considerable industrial interest in further development of nondestructive on-line measurements of r-values during production (at the steel mill, or during the stamping operations). Towards this end, a collaborative research between LTV Steel Company, National Steel Corporation, Ford Motor Company and Ames Laboratory was conducted. This included theoretical and experimental research on a total of 260 steel samples cut from 26 lifts (~10-12 samples of 20 in. by 20 in. (50 by 50 cm) per lift) of 5 types of commercially produced steels of Interstitially Free (IF), Aluminum-Killed Drawing Quality (AKDQ), Bake Hardenable (BH), High Strength Low Alloy (HSLA) and Phosphorus High Strength (HS) grades. These investigations also included tensile measurements on the steels (one per lift) and neutron diffraction (one per lift for 10 selected lifts). This research evaluated the ultrasonic technique with respect to its accuracy and reproducibility, sensitivity to the microstructure of the steel sheets (texture), and the factors that may affect the relative value of its predictions of plastic properties. The experimental correlations and the repeatability data (obtained from sequential ultrasonic meas-

---

urements carried out on the nominally identical samples, 10-12 per lift) point to an excellent sensitivity of ultrasonic waves to the texture of the steels, and a sound electromagnetic coupling between the EMAT's and the sheets, which is important for an on-line system. The data also indicate that the most important factor affecting the ultrasonic r-value predictions is the accuracy of the single crystal elastic constants (which should be representative of the chemical composition of the steels under study). The choice of modeling (in prediction of plastic properties) also plays an important role. Here the relaxed constraint model provided a significant improvement over the empirical correlations of Mould-Johnson. The diffraction data indicate that the 6th order coefficients (mostly  $W_{600}$  and  $W_{620}$ ) improve predictions of r-values (mostly for the IF steels) and that they should be included in the analysis for future use.

---

## **CHAPTER 1**

### **INTRODUCTION**

Low carbon steel sheet is one of the most important products of the steel industry today. It has this pre-eminence since it not only provides strength and rigidity but can also be formed easily into the intricate shapes desired for consumer products. No other material has yet offered, at low cost, properties such as strength, the ability of being readily formed into various shapes, attractive surface finish and easy weldability.

Formability of rolled steel sheets is usually determined by the two important properties of drawability and stretchability. Drawability is indicated by the plastic strain ratio known as the  $r$ -value (ratio of strain in width to the thickness direction of a steel specimen pulled in uniaxial tension to ~10-20%), while stretchability is indicated by the strain hardening factor,  $n$ -values (the slope of the true stress-strain plots of steels). Over the past two decades, these two parameters have been found to correlate very well with the performance of low carbon steels in press shops with the frequency of their measurement (as a quality control check) increasing. Their roles and meanings will be described in the following sections within the general frame work of the forming and stamping process which is at the heart of forming engineering operations in industries such as automotive and appliances. From a quality assurance perspective, therefore, on both the supply side (i.e. steel companies) and OEM side (i.e. automotive and appliance industries), the need exists for a rapid and on-the-spot nondestructive inspection of the rolled steel's essential press properties such as  $r$  and  $n$ -values to evaluate the drawability and stretchability of the steel.

The inspection systems for drawability ( $r$ -values) assessment of steel sheets include both destructive measurements such as tensile testing and Modul- $r$ , and the recently developed nondestructive techniques utilizing X-ray diffraction and ultrasonics. The nondestructive

---

techniques provide a more attractive alternative since they are potentially cost effective, they require fewer man-hours, and they do not damage the material. Of these, ultrasonics appears to have an advantage over X-ray techniques due to safety considerations with respect to radiation as well as the potential for lower cost instrumentation.

Both the ultrasonic and X-ray technologies have evolved in recent years to the point that automated, microprocessor-based, instruments for assessment of sheet steels drawability ( $r$ -values) have been designed and evaluated (1-7). These include prototypes of inspection systems for use as both in static (2) and on-line modes (1, 3-7). One such system, which is a static instrument and is the topic of the present work, is called Ultra-Form. It was designed and developed in 1990 at Iowa State University by the Center For Nondestructive Evaluation, in Cooperation with Ames Laboratory under funding by the Department of Commerce (2). During the course of a field trial to evaluate its performance, Ultra-Form's capabilities were put to test in a series of on-site 'blind' measurements on samples selected from among the variety of processing conditions provided by 3 steel manufacturing plants, Weirton, Wheeling-Pittsburg and Inland Steel. Other tests were performed at Ford Motor Company and included steel sheets provided by 6 manufacturers. The preliminary data collected on 39 commercially produced low carbon steels proved that the ultrasonic technology to assess the drawability of steel as manifested in this instrument is feasible and realistic. The present work was originated to further examine the capabilities of this instrument as well as the factors that may affect its measurement values and their accuracy in a more controlled set of experiments than the one carried out in 1990.

Therefore, a collaborative project between Iowa State University, Ford Motor Company, National Steel Corporation and LTV Steel Company was designed to support the present research. This mixture of participants proved to be very beneficial, since the composition of the participating companies is representative of both sides of the forming industry (supply

---

and OEM). Having technical inputs from these partners enabled this work to represent the overall view of the forming industry and its current practical problems, in the context of which a material characterization technology such as the one used in the present instrument can be of benefit.

The following background sections will attempt to give a general perspective on the sheet metal forming process along with the definition of the pertinent formability properties of rolled steel sheets. This will naturally lead to the identification of the role that ultrasonic technology can play in the forming and stamping industry and to the description of Ultra-Form. The last section of this chapter will outline the specific fundamental objectives of the present work.

### **1.1 The Forming Process: Overview**

The sheet metal forming process has many aspects, depending on the product and the industry. The conventional processes include deep drawing, stretching, bending and roll forming. The nonconventional ones include processes such as explosive and blow forming, hydroforming and superplastic forming (8). A stamping operation (as is most commonly used in the automobile and appliance industries) can be viewed as a way of producing the final product through use of a number of the aforementioned forming processes such as drawing, bending or stretching in one or a multistage operation. Generally speaking, the stamping operation involves four major types of equipment, presses and dies, feed and safeguard mechanisms, (9). Each one of these elements must be considered in the design stage. For instance, tonnage capacity of presses will have to be selected based on the blank size and the shearing strength of the material, or the dies will have to be designed to meet the specified blueprints set by the design, the material will have to be chosen keeping its forming properties in mind and so on. The process flow may be manual with the operator feed-

---

ing the material or it may be fully automatic.

Traditionally sheet metal stamping has been an art rather than a science as explained by Keeler (10). Even with the major technological advances in this century, which have enabled press shops to produce highly complicated products, the die and tooling are still mostly designed and built through prototyping or trial-and-error methods. Product, process and tooling are designed based on the precedent designs and the judgment and skills of the industry personnel, the die and tool makers or 'artisans'. The designs are then refined in what is called a tryout process where successive tests and modifications take place. Needless to say, the tryouts are non-value added activities that greatly increase the lead time and costs of introducing new designs or productions. Even when tryouts are complete, there are no guarantees that the process has been optimized or the final product will meet the design specifications (11).

Although the conventional forming processes have been in use since the nineteenth century, the scientific study of the forming process and its technology has not been able to produce a comprehensive and valid predictive formability analysis to solve the problems encountered in the press shop. This is due to the extremely complicated nature of the deformation mechanism of metals and the number of variables that are involved in the stamping process itself. A comprehensive formability analysis requires the interaction of many concepts from a heterogeneous group of disciplines including engineering, mathematics, metallurgy and physics. The complexity of forming a product can be appreciated by examining Fig. 1.1 which demonstrates the cover of a power cruise control unit stamped from a blank of rolled sheet in nineteen operations and threaded at the end (10).

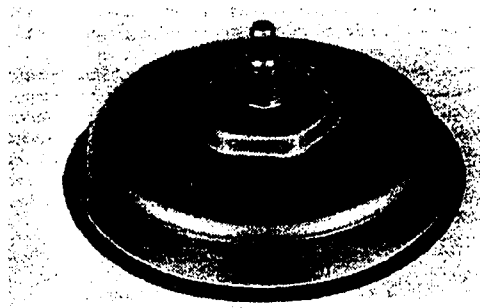


Fig. 1.1 The cover of a power cruise control unit (10)

### **1.2 The Forming Process: Problems**

The most common problem in forming is failure of the material due to localized strains and geometrical defects. The former includes necking, cracking and tearing while the latter includes wrinkling, puckering and elastic recovery or springback. The cause for any or all of these could be a culmination of a number of factors such as instability in the deformation process caused by the uneven distribution of strains, material behavior as related to its tensile properties and forming limit strains, effects of lubrication and tooling on the deformation process, design variables such as punch force and binding pressure, punch and die radii and so on. The goal of industry has been to reduce these problems by developing a predictive capability, preferably in the design room, to prevent the failure from occurring in the press shop.

In order to demonstrate the approaches that may be taken in analyzing a forming prob-

lem, one may use the analogy of a 'generalized' deformation system presented by W.A. Backofen in his 1964 keynote speech to the 9th Sagamore Conference on Deformation Processing (12). Figure 1.2 shows such a system where incoming metal is being deformed in a narrow channel which is shaded dark in the figure. This 'generalized' system is intended not to be concerned with the specifics of any one process, but it rather attempts to identify the different problem areas which are common to a number of deformation processes such as rolling, drawing, extruding, forging and the like.

There are 5 problem areas that are identified. Area 1 is the zone where the incoming metal is being dynamically deformed. This is the zone where the deformation itself is analyzed with respect to problems such as instability, homogenous or inhomogeneous deformation and yielding under a biaxial or triaxial stress state. The Phenomenological plasticity based on continuum mechanics theories (anisotropy theory and yield criteria based on Hill and Von Mises findings) are used to acquire information about first order effects such as distributions of displacements and stresses or strains. The properties are given and no specific reference is made to the microstructure.

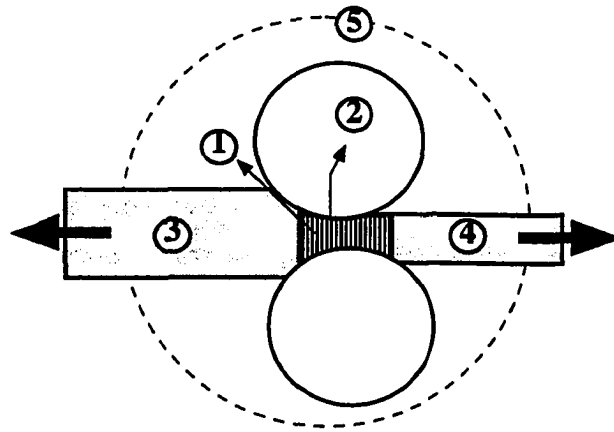


Fig. 1.2 Problem areas of a generalized system (12)

Area 2 is the tool-metal (elastic-plastic) interface. Here the questions of friction, and tool wear are discussed. Such effects as the restriction of the stress flow by the tool (thus creating a boundary condition) and the impact of lubrication on forming and deformation is of interest.

Area 3 is concerned with the mechanical behavior of material under service conditions or under conditions of processing as the incoming metal is being deformed. Constitutive relations, strain hardening, recrystallization, fracture and related problems are of concern. However, due to the unknown state of properties during service conditions the laboratory simulative tests such as tensile and Swift tests are only limited rough approximations of the real behavior of the deforming material under stamping.

Area 4 is essentially a metallurgical interest. Here, the resulting microstructure is representative of all of the deformation history. Matters such as grain refinement and recrystallization, formation of slip bands due to the cold work, texture development and etc. are the microstructural factors influencing the performance of the final product. Area 5 is loosely the overall system which is the focus of input and information from the other areas. It includes the primary tools and equipment (dies and presses) and all the instrumentation for the process control to control temperature, speed, humidity and so on. This is the realm where the designer responds to the needs set by the new shapes and materials used in the production.

It is evident that all of these problem areas are interrelated. The particular strain-time-temperature path in area 1 as influenced by the boundary conditions in area 2 along with the metallurgical factors in area 3 will influence the final microstructure for the application in area 4 which can be predicted only if the understanding in other problem areas of 1-3 is comprehensive. There has been a great deal of recent improvement in predicting formability problems with the development of powerful finite element codes using macroscopic plastic-

---

ity theories (e.g. ABAQUS). However, due to the complexity of the forming designs and the time restraints on computations and number of mesh elements, the solutions are limited to idealized stress states or specific stamping processes (11). In most of these packages, designs are evaluated through numerical calculation of strain or thickness distribution under a set of assumptions regarding the stress/strain state and plasticity and constitutive laws. This distribution is then checked with the forming limits of the material (forming limit diagrams) to determine whether the design is feasible or not.

Another aspect of stamping problems experienced in the press shop are the unknown variables that affect the formability. As Keeler points out, this is the most severe problem that faces press shop personnel on a day to day basis (10). This leads to questions of process and quality control and efforts have been made to have a 'robust stamping or forming process'. Examples include statistical distribution of properties in the steel material or the lubrication materials supplied by the supplier caused by variations in the processing conditions at the production level. Variations in the conditions of the stamping process itself, such as press speed, die wear, blank thickness quality, humidity and temperature can also have a significant influence. The list goes on and on, keeping in mind that the final product is sensitive more to some factors than others.

One way of obtaining robustness in the operation is by seeking a 'forming window' where the maximum and minimum values of formability properties such as  $r$  and  $n$  throughout the steel coils are known *a priori* (9). This allows the process designer to take into account otherwise 'unknown' information: the variability in steel forming properties which may lead to downtime during the operation. Here, a nondestructive ultrasonic detection of determining these properties throughout the entire coils, becomes beneficial in contributing to the robustness of the forming operation as a whole. Similar use of ultrasonics in the mill would also be beneficial to the steel supplier, where continuous feedback information re-

garding the microstructure of rolling steel can be used to optimize properties during the rolling process. Currently such characterization of the properties through the entire coils are impossible due to the time and cost involved with traditional tensile testing. Therefore, it is apparent that a material characterization technique such as the one which is the topic of the present work, the ultrasonic measurement of drawability, can be used in problem area 3 and 4 with possible contributions to area 5 (Fig. 1.2).

The following sections will, therefore, discuss formability as related to the properties of the incoming material (area 3 in Fig. 1.2).

### **1.3 Forming Properties of Steel**

As the previous sections illustrate, various factors are involved in a successful stamping operation. No single factor is totally responsible for success or failure in a complex stamping. The deformation modes generally include drawing, stretching, draw-stretching, bending or a combination of the four. Figure 1.3 demonstrates a sketch of a product of a complex forming operation with all the three major modes of deformation present to some degree (plain strain being a special case of drawing or stretching) (51).

Properties of interest in steel with respect to forming are the  $r$ -values,  $n$ -values and to some extent yield and tensile strength and total elongation. A number of simulative biaxial stress tests were designed in the fifties and sixties to study the formability of sheets. Some of the more well known ones include Swift, Fukui (for deep drawing), Jovignot, and Bulge testing (for stretching) (13). In most of these tests, the drawability or stretchability is characterized with respect to a maximum blank diameter (or a maximum cup height) that can be drawn or stretched without failure. Examples include limiting blank diameter or limiting drawing ratio, LDR in the Swift test or the conical cup wall, CCV in the Fukui test or the limiting stretch ratio in stretching tests. These tests do not, however, obtain properties such

as tensile and yield strength or elongations numerically, as obtained in a tension test.

Prior to the pioneering investigations of Nelson et al. (14) and Lankford et al. (15) in the fifties, such properties as yield strength and total elongation were used to explain the press performance of steels. However, measurement of these properties through uniaxial tension tests is ambiguous and depends on the testing procedure (e.g. total elongation includes the deformation both before and after the fracture has taken place which is the ground for rejection of the parts in press shops. It is also dependent on gage length of the tensile specimen). Further details regarding the tension test and its limitations may be found in Chapter 3.

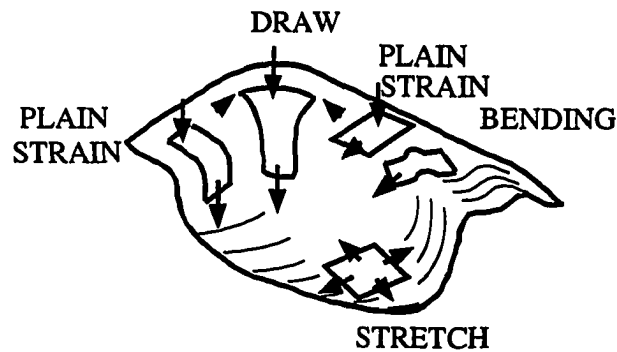


Fig. 1.3 Various deformation modes in a complex part (51)

As mentioned previously, it has been found that the parameters  $n$  and  $r$ , in some combination, are important measures of sheet formability. Nelson et al. (14) found that for operations that involved almost pure stretching, steels with higher  $n$ -values performed much better than those with lower  $n$ -values. Lankford et al. (15) emphasized the role of the strain hardening factor, and also discovered and defined the plastic strain ratio, the  $r$ -value, of steel sheets. His experiments, which involved the actual press forming of a number of low carbon aluminum-killed steels with seemingly uniform properties (such as tensile, yield

strength and elongation), showed that in deep drawing operations, materials with high  $r$ -values exhibited a better drawing performance and attributed this to the presence of plastic anisotropy in the rolled sheets which he tested. His results ignited great interest which led to a number of later examinations of the role of anisotropy in drawing operations. The next section describes these two parameters in more detail.

### 1.3.1 Stretchability Index: $n$ -values

Figure 1.4 demonstrates an idealized stretching operation. Here, a firm normal pressure keeps the blank from moving into the die cavity and, therefore, all the deformation occurs across the nose of the hemispherical punch. The stress state is biaxial with both major and minor components present. Failure is generally due to necking or localized strain distribution. The ability of the steel to maintain a uniform strain distribution is related to the work hardening coefficient or  $n$ -value. Figure 1.4 also shows a sequence of events leading to the failure. Although stretching is a biaxial stress state, the results of a uniaxial tensile test serve to illustrate this point well as suggested by Blickwede (16). As the material is stretched beyond the elastic regime into the plastic regime, due to the process of work hardening, the stress increases with increasing deformation. The material elements elongate and thin uniformly, passing the strain to the adjoining elements until the stress reaches the ultimate strength or the limits of uniform elongation are exceeded. Here, the strain becomes localized (leading to necking), and fracture then occurs.

The  $n$ -value is usually calculated from the results of a typical tensile test by obtaining the slope of the true stress-strain curve (i.e. log-log plots) as approximated by the power law of  $\sigma = K\epsilon^n$  where  $K$  is a material-specific constant determined empirically. The work hardening factor is in fact numerically equal to the strain at maximum load or for uniform elongation at the onset of necking,  $\epsilon_u$ . It also relates to the ratio of tensile strength to yield strength. The

higher the  $n$ -value, the higher is this ratio. The peaks in the strain distribution plots of materials with higher  $n$  are less pronounced than the ones in materials with smaller  $n$ -values, thus indicating a more uniform strain distribution (17).

The microstructural factors affecting  $n$ -values are the presence of substitutional alloying elements, dissolved interstitials, excess phases and grain size as indicated by Blickwede (16). Gensamer (18) established that there is a relationship between flow strength and  $n$ . He showed that the substitutional elements such as copper, silicon, manganese, and nickel tend to increase the flow strength and thus reduce the  $n$ -values of low carbon steels. The degree of increase in flow strength changes with the degree of solubility of these elements (i.e. elements with less solubility lower  $n$  more). The effects of interstitial elements (small amounts of carbon or nitrogen in solution) on  $n$  are indirect. They affect strain aging significantly which, in turn, adversely affects  $n$ . Excess phases such as carbides also lower  $n$  (19, 20). The grain size of low carbon steels is the dominant and controlling factor in obtaining a good strain hardenability. Increasing grain size increases  $n$ -values and in fact an empirical relationship between  $n$  and grain size was obtained by Morrison (21) which was confirmed by Blickwede (16) :

$$(1.1) \quad n = \frac{5}{10+d^{-0.5}}$$

where  $d$  is the average grain diameter in millimeters.

The typical range of  $n$ -values for most of low carbon steels is between 0.15 to 0.25 range. Blickwede (16) has shown that, for the typical range of grain sizes of annealed sheets (0.022-0.045 mm), the variation in  $n$  would be  $\sim 0.04$  (from 0.29 to 0.33) using Eqn. 1.1.

This variation is appreciable, and it may spell the difference between success and failure in stretching operations.

### 1.3.2 Drawability Index: r-value

The drawability of a steel sheet is determined by its ability to flow easily in the flange area when drawn into the die cavity and its resistance to thinning near the cup wall inside the die. Figure 1.5a shows an idealized drawing. Here, the clamping or binder pressure is just enough to permit the blank to move with the punch into the die cavity without any buckling. The flange elements experience circumferential stresses and in the die cavity the material is subject to radial tension, Fig. 1.5b. The punch is flat nosed and does not allow the sheet to deform in the lateral directions. Therefore, deformation basically occurs through thinning.

The important capability of the material is to have low flow strength in all directions of the plane of the sheet (the flange area) and high flow strength in the side wall (resist deformation through thickness), (16). The ratio of the two stresses in the flange area and the side wall is related to the r-value, or plastic strain ratio, which is commonly obtained through determining the true strains in the thickness,  $\epsilon_t$ , and width direction,  $\epsilon_w$  of steel specimens pulled in a tensile test:

$$(1.2) \quad r = \frac{\epsilon_w}{\epsilon_t}$$

Since measurement of thickness strain is sensitive to errors, the strain in the gage length and width of the specimen is usually measured instead and used in calculations. This is possible

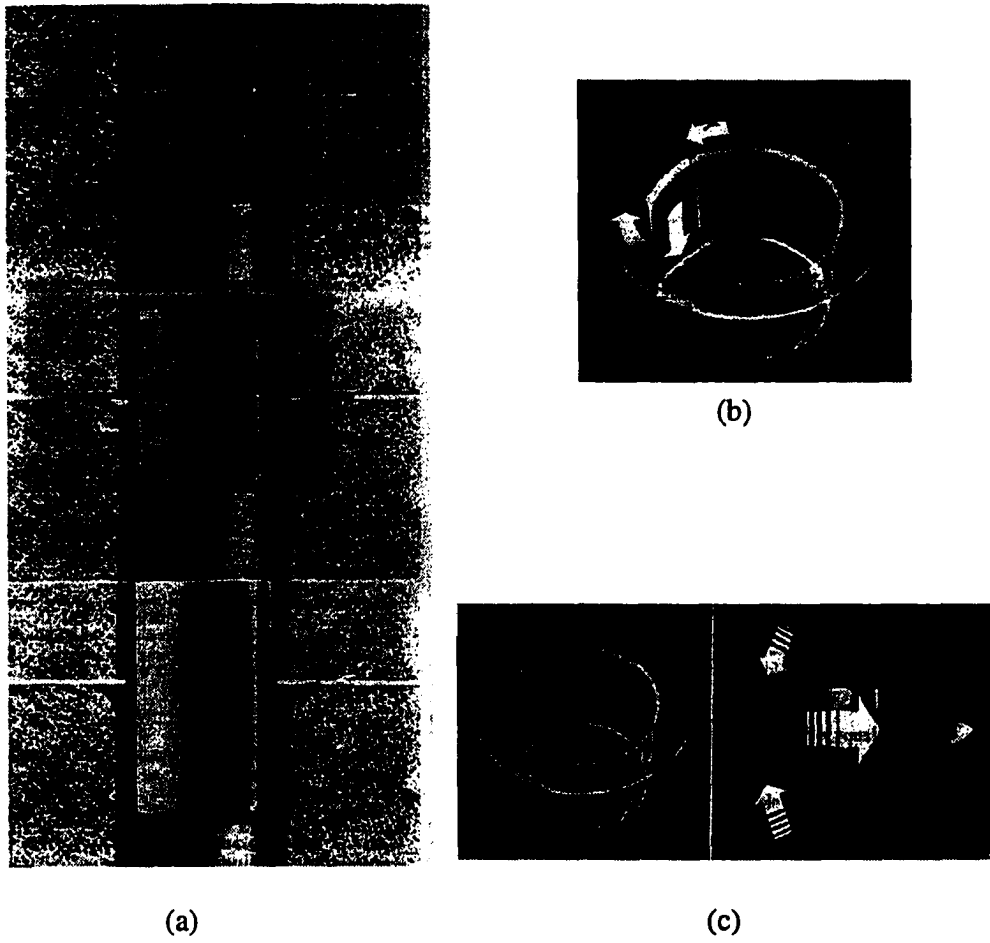


**Fig. 1.5 An idealized drawing operation (16)**

**(a) The drawing sequence**

**(b) The flange and the stresses**

**(c) The cross section of the flange**

due to the principle of constancy of volume in the plastic deformation regime:

$$(1.3) \quad \epsilon_l + \epsilon_w + \epsilon_t = 0$$

and, therefore,  $r$  can be expressed in the following way:

$$(1.4) \quad r = \frac{\epsilon_w}{-(\epsilon_l + \epsilon_w)}$$

or, in terms of the true strain:

$$(1.5) \quad r = \frac{\ln \frac{w}{w_0}}{\ln \left( \frac{w_0 l_0}{w l} \right)}$$

where  $w_0$  and  $l_0$  refer to the original dimensions of the tensile coupons.

Rolled sheets of steel exhibit anisotropy in their properties. This is due to the preferred orientation of their grains which they obtain during rolling. Therefore,  $r$  changes with the orientation of the coupon relative to the rolling direction. It is customary to calculate a weighted average value using  $r$ 's measured on coupons cut at 0, 45 and 90 degrees relative to the rolling direction:

$$(1.6) \quad \bar{r} = \frac{[r(0)+2r(45)+r(90)]}{4}$$

This parameter, known as the average normal anisotropy, represents the resistance to thin-

ning in the side wall. The planar variation of  $r$ , denoted by  $\Delta r$ , represents the degree of anisotropy in the plane of the sheet (flow strength in the flange plane), and is defined by:

$$(1.7) \quad \Delta r = \frac{[r(0)+r(90)-2r(45)]}{2}$$

$\Delta r$  has been shown to correlate with the amount of earing in drawn cups.

The average strain ratio,  $\bar{r}$ , changes between less than 1 (special cases of only hot rolled sheets), to 1.6-1.8 and above 2 for deep drawing grade steels.

Theoretical investigations of the deep drawing operations using continuum mechanics plasticity theories have been extensive, (for a review see reference 22). However, historically, the role of anisotropy in plastic properties and its influence on drawability was not understood until the investigations of Lankford et al. (15). In fact up to that point, anisotropy was considered detrimental to good drawability and isotropy was considered desirable. Lankford recognized the advantages of plastic anisotropy when steels with high  $r$ 's (i.e. at 0, 45 and 90 degrees) performed well in press. He attributed the observed anisotropy to the preferred orientation of grains or their crystallographic texture through magnetic torque experiments. Extensive subsequent works by Whitely (23), Whitely, Wise and Blickwede (24) and Whiteley and Wise (25) using X-ray diffraction techniques to investigate the effects of mill processing on texture induced anisotropy and  $r$ , further supported this conclusion. Chapter 2 discusses crystallographic texture and its importance in obtaining a superior  $r$ -value in more detail.

The early investigations of relations between  $r$ -values and the parameters of biaxial stress cupping tests such as LDR were not successful, as explained by Atkinson (26). However, his own results, which he obtained through closely controlled experiments (particularly with respect to lubrication) on low carbon steels by performing tensile and Swift tests resulted in strong correlation between  $\bar{r}$  and LDR. He attributed the early lack of success in the work of previous investigators to variations in lubricating material which is important in cupping tests. Whiteley et al. (24) had earlier demonstrated the strong influence of normal plastic anisotropy on the Swift test. He also developed a theoretical relation between the ratio of the stresses in the side wall and flange area, ( $\beta = \sigma_w / \sigma_f$ ) to LDR and between LDR and  $\bar{r}$  based on continuum mechanics theories. The general effect is that the larger the  $\bar{r}$ , the larger the value of LDR. The same trend has been reported with respect to the relationship between  $\bar{r}$  and  $\beta$ , where the larger  $\bar{r}$ -values are associated with larger values of the stress ratio.

The tensile testing techniques commonly used to obtain  $r$ -values are problematic and hypersensitive to measurement errors. Despite the practical and theoretical importance of this parameter, relatively little effort has been made to develop alternative drawability tests (26). From the perspective of both industrial control of drawability and the need for a more reliable measurement technique, an on-line characterization of this important parameter is critical to stamping or milling operations. As mentioned previously, crystallographic texture is the most important property of the material influencing anisotropy in rolled sheets of ordinary low carbon steel. As will be discussed in the next subsection and Chapter 4, it is this property that can be sensed by and correlated with acoustic properties (propagating velocity of ultrasonic pulses) making the ultrasonic technique a candidate for measuring drawability.

---

## 1.4 Ultrasonic Measurements of r-values: Ultra-Form

### 1.4.1 Review

The basis for the ultrasonic measurement of drawability lies in the fact that the preferred orientation of grains in sheet metal result in anisotropy of the elastic properties as well as the plastic properties. It is, therefore, possible to relate the variations of an elastic property such as Young's modulus,  $E$ , to variations in the plastic strain ratio,  $r$ . The practical utilization of a relation between Young's modulus and texture was first demonstrated by Alers and Liu (27). Papadakis et al. (28) demonstrated the same idea using ultrasonic measurements. Stickles and Mould (29) related the variation in  $E$  to plastic strain ratio for a limited number of commercially available low carbon steels. Later, an empirical correlation was obtained based on a larger number of samples (30), forming the basis for the Module-r device, marketed by Tinius Olson. The data of Mould and Johnson is shown in Fig. 1.6 with the experimental correlations having the form:

$$(1.8) \quad \bar{r} = \frac{101.44}{(38.88 - \bar{E})^2} - 0.564$$

and

$$(1.9) \quad \Delta r = .031 - 0.323\Delta E$$

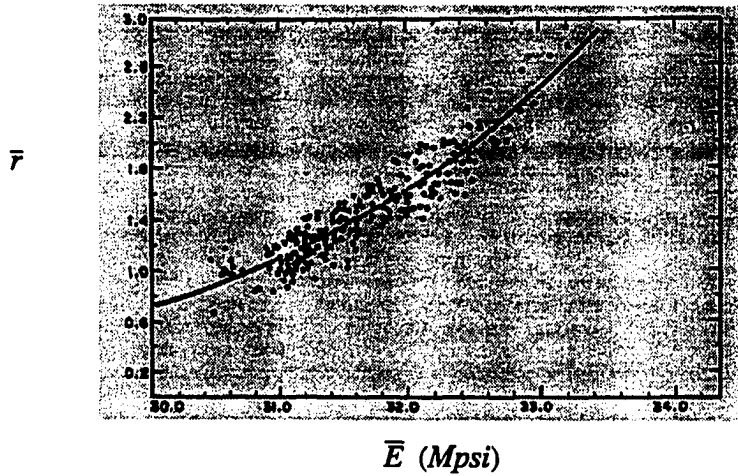


Fig. 1.6 Mould-Johnson correlation (30)

Quantitative texture analysis developed by Roe (31) in the U.S. and Bunge in Germany (32), provided a mathematical formalism used by Davies et al. (33) to lay a theoretical foundation for the above empirical correlations. In particular, the grain orientation of a rolled sheet can be described in terms of orientation distribution functions (ODF) which are represented by a series of generalized spherical harmonics (in a manner similar to the representation of a function by a Fourier series):

$$(1.10) \quad w(\xi, \psi, \phi) = \sum_{l=0}^{\infty} \sum_{m=-l}^l \sum_{n=-l}^l W_{lmn}(\psi) Z_{lmn} e^{-m\psi} e^{-n\phi}$$

where  $\xi = \cos(\theta)$ , and  $\theta$ ,  $\psi$  and  $\phi$  are the Euler angles (expressed in Roe's terminology (31)) describing the orientation of the crystallites in the polycrystal. The concept of ODF's will be explored further in detail in Chapter 2. The coefficients of these spherical harmonics (orientation distribution coefficients, ODC's) act as weighting functions. When combined with information concerning the orientation dependence of the physical properties of crystallites, they provide data as to how well a particular grain orientation affects properties of the sheet material, such as E and the r-value. It was noted by Davies et.al (33), that the ODC,  $W_{400}$ , was closely related to the drawability, while coefficients  $W_{420}$  and  $W_{440}$  correlated with the tendency to form two-fold and four fold ears, respectively.

Based on these foundations, rapid progress has been made in the past decade towards an ultrasonic instrument to predict r-values. In 1985, Thompson et al. (34) proposed the concept of the EMAT approach. EMAT's (electromagnetic acoustic transducers) differ from the traditional ultrasonic piezoelectric transducers in that they do not require any coupling medium (such as water or gel) to generate the waves in the metal. This makes them very attractive for on-line characterization of steels. It was shown as early as 1973 that the presence of texture-induced anisotropy in the plate wave speeds could be sensed by EMAT's (35). In 1987, the correct equations relating the measured velocities to the ODC's  $W_{400}$ ,  $W_{420}$  and  $W_{440}$  were reported by Thompson et al. (36). Also corrections to compensate for both the thickness of the sheet and its coating effects were devised (37, 38).

All of the above developments have led to the design and fabrication of Ultra-Form, an automatic, microprocessor-based ultrasonic instrument in 1990. The details of its design and development have been reported previously (2). This instrument uses the measured velocities to obtain ODC's, from which Young's modulus can be calculated and subsequently fed into the Mould-Johnson correlation, Eqn. 1.8, to obtain  $\bar{r}$ .

## 1.4.2 Ultra-Form's Description

**1.4.2.1 Sensors (EMATS)** Figure 1.7 includes a photograph of the Ultra-Form instrument and the probe head of the EMAT sensor array. The probes consist of a coil of wire through which a radio-frequency, high current burst is passed. In the presence of a magnetic field (produced by permanent or pulsed magnets), Lorentz forces cause an ultrasonic pulse to be launched in the metal. In some cases, magnetostrictive mechanisms also play a role. The wave can be detected by reciprocal processes in a receiving EMAT sensor. Ultra-Form has three arrays of such EMATS consisting of two transmitters separated by 4.5 in (11.4 cm) and one remote receiver. The three pairs of transmitting EMATs are housed in a central octagonal region with the three receivers located in the arms of the probe, which are built to be aligned with the rolling direction, 45 degree to the rolling direction and the transverse direction. The probe head is, therefore, positioned on the sheet in such a way that the arms are aligned properly with the three axes of the plate. The period of the meander coils in these EMATs is approximately 0.4 in. (1.02 cm), with an operating center frequency of 450-550 kHz depending on the thickness of the plate and its properties. The reason for this dependence of frequency on plate characteristics is due to the nature of the propagation of ultrasonic waves in a bounded media, i.e. a guided wave propagation. For a given set of density and elastic constants, the waves travel with a speed which is dependent on the combination of frequency and plate thickness, and the transducer operation is most efficient when the wavelength (frequency divided by speed) equals the EMAT period.

**1.4.2.2 Main Controller** As Fig. 1.7 demonstrates, operator interfacing with Ultra-Form is achieved through a touch screen unit with a number of input screens for the operator to enter the desired commands. The main inputs by the operator are the plate thickness and its material (steel, aluminum), the thickness of any coating on the sheet, and the outputs which are desired to be seen. The latter could include  $\bar{r}$ ,  $\Delta r$ , Young's modulus in three

directions its average value and  $\Delta E$ , and the velocities of the ultrasonic waves. The central processor of this instrument consists of a controller unit with three microprocessor chips which are used to activate the analog modules in order to provide the necessary magnetic field and radio frequency signals for the transmitting EMAT probes. These chips also control the adjustment of gains of the receiving amplifiers and their analog to digital conversion. The output can be sent to a printer via a serial connection or it can be down-loaded directly to a personal computer for further analysis.

#### **1.4.3 Other Recent Advances**

There have been other new improved developments in instrumentation technology desiring for the routine industrial use of the ultrasonic on-line measurement of r-value (5). With respect to the relations between elastic and plastic anisotropy, several groups have reported correlations between ultrasonic measurements and plastic strain ratio. In Japan, new correlations as well as an extension of the Mould-Johnson correlation have been examined (39). In Canada, ODC's obtained from ultrasonic velocity data have been used as input data into microscopic deformation models based on single crystal and polycrystal plasticity theories (40). These deformation models (relaxed constraints models) which are all variations of the original deformation theory of Taylor (41) have presented alternatives to the empirical correlations such as the one of Mould and Johnson.

#### **1.5 The Present Research**

The major objective of the present study has been to investigate the capabilities and accuracy of the instrument, Ultra-Form, in a more controlled manner than has been done previously (as reported in (2)). In addition to the industrial interest in pursuing future developments of an on-line nondestructive measurements of r-values, this work was primarily

---

motivated by the desire to further explain the agreement which was obtained between the ultrasonic data and the traditional tensile tests data of 1990. At that time, this instrument was physically transported to the plants of interested industrial partners and a series of 'blind' ultrasonic tests was performed on sheets of interest with average  $r$ -values ranging from 0.9 to 2.4 with steels processed under a variety of conditions (hot rolled, cold rolled and annealed, coated or uncoated). The ultrasonic predictions of  $\bar{r}$  and  $\Delta r$  were compared with the values inferred from tensile results provided by the host steel and auto companies. The agreement between ultrasonic and tensile measurements on 39 samples proved to be excellent for lower to high middle range  $\bar{r}$  steels (less than 1.8). However, there was a significant deviation and scatter for steels with  $\bar{r}$ -values greater than 1.8. Figure 1.8 demonstrates the results on the 39 samples with the solid line showing a perfect fit between ultrasonic and tensile results.

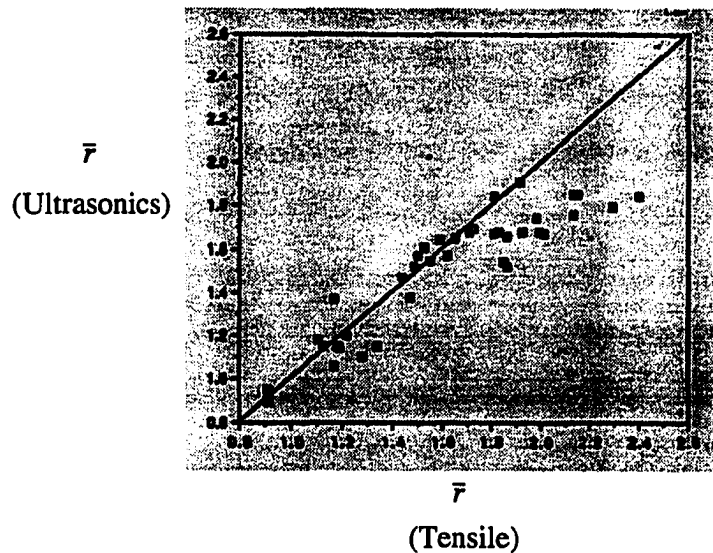


Fig. 1.8 The previous agreement between ultrasonic and tensile measurements (2)

A number of candidate explanations for this error were considered. These included: 1) Inadequacies of the experimental correlation of Mould and Johnson or alternatively, lack of a suitable deformation model that could use ultrasonic information as input. The empirical data of Mould and Johnson were obtained in the late sixties on 230 steel samples manufactured by U.S. Steel Corporation over a period of two years. The samples included a variety of low carbon steel sheets such as cold rolled aluminum-killed drawing quality (AKDQ), rimmed steels, tin-plate, enameling steels and some experimental steels (30). There is a certain amount of scatter in the data ( $\pm 0.2$ ) about the correlation fit, which the authors attributed to the experimental spread in the mechanical measurements of  $r$ -values (due to different details of tensile tests and operator to operator variation). Although the large number of steel samples involved in this study increased the statistical confidence of its correlations, it is still an empirical correlation which is subject to a limited data base, 2) The limitations of ultrasonics in quantifying crystallographic texture and its lack of sensitivity to the particular texture of high  $r$  steels. This factor was considered since the ultrasonic technique is only sensitive to 3 ODC's ( $W_{400}$ ,  $W_{420}$  and  $W_{440}$ ). This means that the influence of higher order coefficients such as sixth order terms,  $W_{6mn}$  would have been missed. It is thought that the fourth order ODC's have primary significance on texture characterization of steel sheets (33). However, Daniel et al. (40) have observed that in some cases such as interstitially free (IF) and aluminum-killed steels with high  $\bar{r}$ , higher order ODC's such as  $W_{6mn}$  are needed in order to provide a more complete description of the textures involved and thus a better prediction of  $r$ -values, 3) Limitations and errors inherent in traditional tensile tests. This has been the subject of intense research, and as stated previously, tensile  $r$ -value measurements are hypersensitive to experimental errors especially in the high  $r$ -value range (26), 4) Lack of reproducibility of ultrasonic measurements in the observed  $r$  range due to an instrumentation problem.

The determination of the relative importance of these factors is an important specific objective of this research. Moreover, two general basic goals were targeted: 1) an improved fundamental understanding of the mechanism underlying the plastic deformation of sheets that takes place in the drawing operation as it relates to the plastic strain ratios, and, 2) an improved fundamental understanding of the relationship of ultrasonic measurements to plastic properties through a theoretical and experimental investigation involving steel samples with properties and textures that are used frequently in forming operations.

In order to proceed with the investigation of all of the above, a collaborative academic-industrial work was designed to carry out the research. The details of these investigations will be presented in the following chapters. Chapter 2 discusses the general topic of low carbon steels and their properties and processing and the importance of their microstructure (texture). Chapter 3 is exclusively allocated to the discussion of destructive techniques for measuring drawability which include the tension test and Modul-r instrument. Chapter 4 is concerned with the ultrasonic technique and the theory underlying it. Chapter 5 deals with the experimental procedures of the present study and presents all the associated results, with Chapter 6 drawing conclusions from these results.

---

## CHAPTER 2

### LOW CARBON STEELS

Plain carbon steels accounted for 77% of the steel produced in the U.S. in 1988 (42). Some of the major applications involving these steels include products such as sheets and strips, bars, structural parts, tubes and castings. The chemical compositions and properties vary depending on the application. The carbon content, which is the most important alloying element in these steels, can be up to a maximum of 1.03% (1095 steels designated according to the AISI system) (42). Included in this classification of plain carbon steels are the low carbon steels which are mostly produced in sheet form. As mentioned in Chapter 1, rolled sheets have large forming applications in auto and appliance industries. The desired properties in these steels are good formability (high  $r$  and  $n$ -values which means low yield strength), high percentages of uniform elongation, good weldability and surface finish. For applications in the auto industry where the sheets are used for the outer door panels of automobiles, a good dent resistance (which implies a higher yield strength) is also required. The carbon and manganese contents in these steels can be as high as 0.1% and 0.3-0.5%, respectively (16). Generally, the final gage thicknesses are no more than ~0.23 in. (~58 mm).

With various degrees of demand for formability and strength, several grades of low carbon steels are produced depending on the chemical composition and processing conditions. The American Iron and Steel Institute, AISI, has categorized these steels according to the following name convention (43): a) Commercial Quality Rimmed grades (CQ), b) Drawing Quality grades (DQ), c) Drawing Quality Specially Killed (DQSK), and, d) High Strength grades. DQ and DQSK groups include the well known aluminum-killed steels. DQSK steels which also include interstitially free steels have superior formability to the ones in the CQ and DQ grades. The high strength grades include High Strength Low Alloy (HSLA), steels

which also include some dual phase steels, bake hardenable grades and tin-plated grades used in the can industry. Tables 2.1 and 2.2 show some typical compositions and properties of the steels that have the most usage in forming and deep drawing operations (43, 44). The name conventions used in these tables are the ones commonly used by academic and industrial organizations. In this work, from this point on, the terms DQSK and AKDQ will be used interchangeably to denote aluminum-killed steels, while IF and BH notations will denote the interstitially free and bake hardenable grades.

All of these steels are generally hot rolled, cold rolled and annealed. Depending on application, they may be coated to resist corrosion (tin, zinc, nickel or chromium). The details of the processing conditions are carefully controlled or varied to obtain the desired properties. Among the various steels, AKDQ and IF steels possess excellent formabilities ( $\bar{r}$  of 1.4-1.8 for AKDQ and 1.8-2.5 for IF steels). The good formability of these steels is due to the formation of a favorable preferred orientation of their crystallites (crystallographic texture). The mechanisms underlying the texture formation (due to the specific processing conditions) in these steels have been investigated extensively, and they are reasonably-well understood. Reviews may be found in references 16, 44-46. The most important stage of the processing for AKDQ steels is the heat treatment or annealing stage (after cold rolling) which is done usually by a batch annealing process. The details of this process have been optimized (through years of experience) to give high  $r$ -values (although continuous annealing is also possible). The carbon contents of IF steels are usually lowered by vacuum degassing prior to casting. The relatively pure matrix and the addition of stabilizing elements such as titanium and niobium coupled with high hot and cold reductions contribute to the development of optimal texture and excellent formability. Due to their chemistry, these IF steels are insensitive to heat treating conditions and can be annealed by batch or continuous annealing processes (45).

Table. 2.1 Typical carbon contents of low carbon steels, (43,44)

<b>Steel Grade</b>	<b>(%w) Carbon</b>
IF	0.002-.01
AKDQ	0.01-0.05
BH	0.01-0.05
HSLA	up to 0.1

Table. 2.2 Typical properties of low carbon steels (43, 47, 48)

<b>Steel Grade</b>	<b>Yield Strength (Ksi)</b>	<b>Tensile strength (Ksi)</b>	<b>% Elongation</b>	$\bar{r}$	$\bar{n}$
IF	25	48	46	2	0.24
AKDQ	30	46	41	1.6	0.21
BH	35	56	36	1.4	0.20
HSLA	55	68	28	1.1	0.16

A new generation of aluminum-killed steels has been designed with comparable formabilities and superior yield strengths. These also exhibit bake hardenability during the paint baking operations. Baking is done to cure the paint on the exterior parts of automobiles during the assembly operations. The as-received yield strength of these steels, which is higher by 5-20 ksi than those of AKDQ's, can increase by as much as 10 ksi after the forming and curing cycle is over (47, 48). These steels which have been in use in Japan since seventies (49), were put to practical use in the U.S. in 1986 at Ford Motor Company (48). Although the chemistry is very similar to that found in AKDQ steels (Table. 2.1), different hot rolling and coiling temperatures allow the carbon to remain in solution (in contrast to AKDQ steels where almost all of the carbon precipitates during the slow heating rates in batch annealing). During the curing cycle, carbon atoms then pin down the dislocations caused by the rolling deformations, thus increasing the final yield strength of the formed steel. The  $\bar{r}$  of these steels can vary from 1 to 1.9 depending on the processing. These steels are usually heat treated in continuous annealing (CA) lines.

The HSLA steels are produced through careful additions of alloying elements such as phosphorous, manganese, vanadium and titanium. The strength is the primary objective here. By judicious combinations of composition and processing method, the strength levels can be increased to a desired level (43). However their formability is offset by the resulting high yield strengths obtained, ( $\bar{r}$  of 1.1-1.2). There are also dual phase grades with ferrite and martensite with small amounts of pearlite and bainite also present (50). With stringent fuel economy standards applied to the auto industry, these steels are finding increasing use for weight reduction in automobiles by down-gaging the steel blanks used.

Although an optimum grade and its properties is selected based on the specifications of a particular design and the corresponding deformation mode, a good formability is perhaps always desired where a high formability may not always be required. For instance, the severity

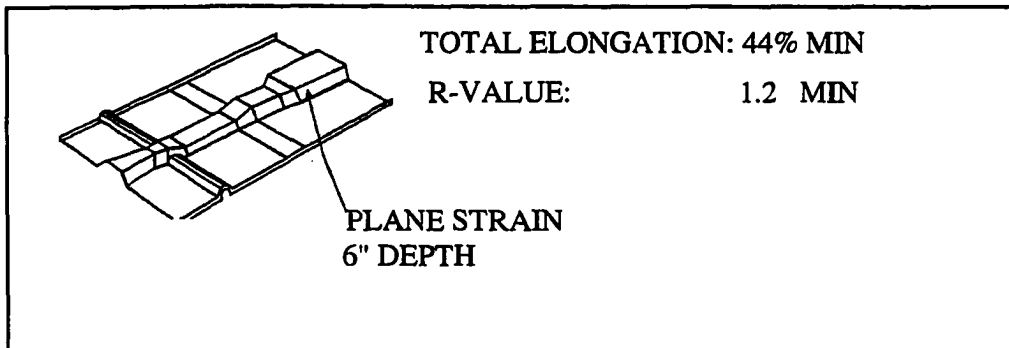
---

of deformation modes in forming operations may be divided in three groups of easy, moderate and severe, Fig. 2.1 (51). For easy to severe drawings or stretches, depending on the yield strength requirements, HSLA, BH, AKDQ and IF steels can be used. Due to the importance of formability requirements, however, almost all of the processing details of low carbon steels have been optimized to yield high  $r$ -values. The following sections will describe the steel making process and mill practices for low carbon steels in general terms applicable to all of the aforementioned steel grades. Following this description will be a definition and description of the most important microstructural factor influencing the formability of low carbon steels: the crystallographic texture.

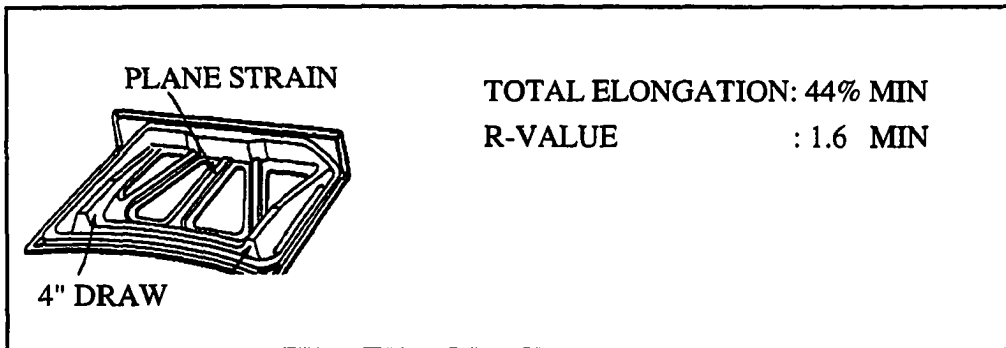
## 2.1 Steel Making and Mill Practices

### 2.1.1 Steel Making

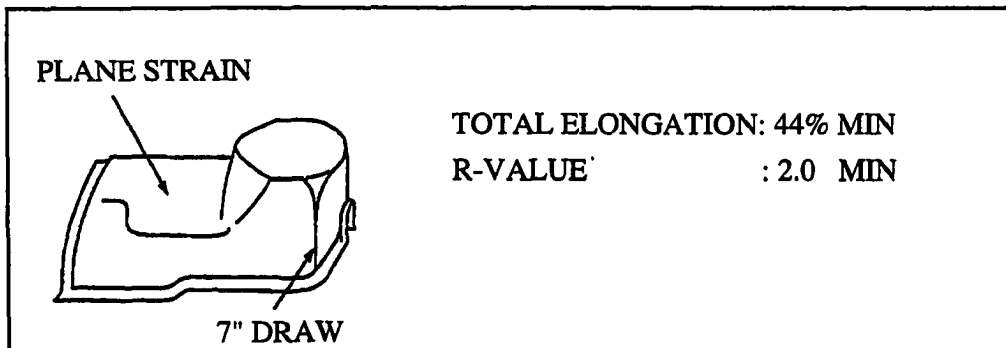
**2.1.1.1 Crude Steel** The iron compounds (iron oxides,  $\text{Fe}_2\text{O}_3$ ) are combined with coke in blast furnaces to produce molten or pig iron which contains about 3-4.5% carbon. To reduce the carbon levels, the molten iron is then oxidized in either electric arc furnaces or in what is called the Basic-Oxygen Process, BOP. Nearly 55.9% of crude steel is now processed using this technique. Here, an oxygen lance is inserted into the liquid bath (pig iron and scrap steel) where a chemical reaction between oxygen and pig iron reduces the carbon levels dramatically. Shortly after the reaction starts, slag-forming fluxes (lime) are added in controlled amounts. The reaction is very rapid and a large amount of steel is produced in less than an hour. The level of impurities such as carbon, silicon or manganese can be easily controlled by the duration of the reaction. These impurities decrease very rapidly with increasing holding times. For example carbon levels can be lowered to less than 1% in 22 minutes (42).



a) Automotive floor pan, with no draw deformation



c) Automotive deck lid inner, with moderate draw deformation



b) Automotive oil pan, with severe draw deformation

Fig. 2.1 Deformation modes (Courtesy of LTV Steel Company,(51))

**2.1.1.2 Casting** Casting is carried out either continuously or through ingots. Most modern steels, however, are cast continuously. This provides a superior cast quality in terms of surface quality of the casts, lack of blow holes or pinholes (caused by residual oxygen), and uniformity of chemical composition. Significant time and cost savings are also obtained. Before the casting operation starts, the crude steel is further refined in ladles where the molten steel is poured directly into the ladle from the furnace. The most important refinements here are the additions of manganese to react with sulfur (forming MnS), addition of aluminum to deoxidize the steel and vacuum degassing to lower carbon levels. The addition of aluminum is quite significant for continuously cast steels since aluminum rids the steel of oxygen thereby reducing the number of defects in casts due to the formation of blow holes.

## **2.1.2 Mill Practices**

**2.1.2.1 Hot Rolling** If the steel is cast in ingots, it is first hot rolled to slabs before it is sent to the hot rolling mill that produces sheets. However, in continuously cast operations, the steel is sent directly to the hot roll mills and, in fact, this is one of the advantages of the continuous casting operation. Hot rolling parameters are vital in terms of generating the appropriate 'hot band' conditions which later influence the microstructure of the steels in the cold rolling stage or more importantly, the annealing cycle. In fact, hot rolling and cold rolling practices are all carefully tailored to the final annealing process (45). The important considerations in hot rolling are the finishing and coiling temperatures. Generally speaking, a deformed ferrite structure is not desirable after hot rolling is terminated. Therefore, finishing temperatures are maintained high enough to keep the steel in the austenitic regime before transformation to ferrite (44). The coiling temperatures are important with respect to precipitation hardening that may take place. This is particularly important for AKDQ steels where the steel is cooled rapidly to temperatures of about 1050-1150<sup>o</sup>F before being coiled. This

---

allows the aluminum nitride (AlN) to remain in solid solution and to later precipitate during annealing, thereby influencing the final grain growth and formability of the steel. It is well known that the good formability of aluminum-killed steels is mainly due to this effect (16, 44-46). Similar considerations apply to bake hardenable steels where it is also vital to keep the carbon in solid solution. The rolling and coiling temperatures for bake hardenable steels are higher than for conventional AKDQ steels (47). The IF steels are processed with heavy reductions, low finishing temperatures and high rolling speeds to obtain a fine grain structure during hot rolling (45).

**2.1.2.2 Pickling and Cold Rolling** The pickling which takes place in acid baths (continuous immersion in HCL or H<sub>2</sub>SO<sub>4</sub> baths at 200<sup>o</sup>F) is carried out to remove the scale from the hot rolling operation. The sheets are then rinsed with water, air dried, oiled and coiled (42). The important considerations in cold rolling are the amount of percent reduction per pass, the number of passes and the total final reduction. For AKDQ steels, the common practice is to reduce the thickness by about 70-80% whose value has been found to yield good r-values. For stabilized IF steels, the total reduction can be as large as 90% (44-46).

**2.1.2.3 Annealing** Annealing is most important in the processing of rolled steel sheets (45). Here, the cold worked steel is heated to recover the ductility that it lost during the cold working process. The important considerations here are the heating rates and the annealing temperatures. Depending on the annealing process, the heating rates can be slow (batch annealing) or fast (continuous annealing).

Batch annealing is the most common heat treatment for rolled steels. Coils of cold worked steels are heated at slow rates generally taking 2 to 3 days. The slow rate of heating is particularly important for AKDQ steels because it allows the aluminum nitride to precipitate. Through a complex interaction between AlN precipitates and the recrystallization process, a favorable texture is developed which leads to the elongated (pancake) grain structure

(Fig. 2.2). This slow rate, however, is not suitable for BH steels where the carbon needs to remain in the solution in order to generate bake hardenability. Therefore, continuous annealing with rapid heating rates and high annealing temperatures is more suitable for BH steels (47). For IF steels, high annealing temperatures and the presence of titanium or niobium carbides along with a relatively pure matrix leads to the formation of a favorable texture with correspondingly high strain ratios (45).

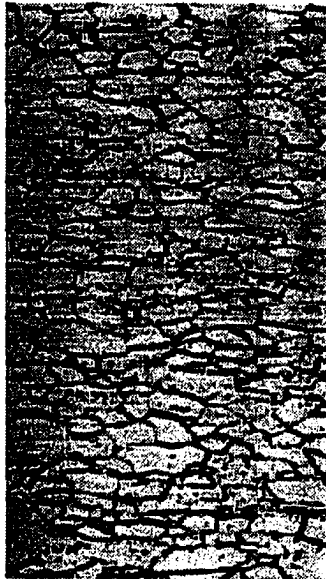


Fig. 2.2 Grain structure of AKDQ steels (42)

## 2.2 Preferred Orientation (Texture)

The drawability of steel sheets is, to a large extent, dependent on the preferred orientation of their grains. The fact that plastic anisotropy has its origins in crystallographic texture has long been proven and established (15, 23-25). As is evident from the proceeding discussions, the mill practices for rolled low carbon steel sheets have been optimized to obtain a certain favorable crystallographic texture resulting in an improved formability. Although this optimization has been achieved independent of modern laboratory and mathematical texture analysis, the importance of such an analysis and its role in improving the quality control of the final product is being increasingly recognized. This is evident from the scope of the work reported in the the literature regarding the evolution of modern texture analysis and its measurements (52, 53). With modern, on-line texture monitoring devices being designed to address quality control issues pertaining to rolled products, this mathematical approach is also finding use in industrial operations (6, 7).

Textures in materials have been studied extensively since the thirties, following the pioneering work of Wassermann (53). Schultz initiated the modern experimental measurement of textures in 1949 when he developed the pole figure technique using X-ray diffraction technology. The more recent evolution of texture analysis includes a mathematical pole figure inversion technique which leads to the description of texture by orientation distribution functions (ODF). This approach was invented by Roe (31) and Bunge (32) in the United States and Germany in the late sixties.

### 2.2.1 Texture Representation

Rolled sheet steels (considered polycrystalline) consist of a collection of grains which may be considered to be single crystals. Single crystals exhibit anisotropy in their elastic and plastic properties, i.e. their properties change depending on the direction with respect to

---

the crystallographic axes. However, in an ideal isotropic polycrystalline aggregate, the grains would be randomly oriented with respect to each other, thus averaging the differences that exist in their properties. In practice, due to metallurgical or processing treatments, the grains will acquire a certain degree of preferred orientation, Fig. 2.3a and b (44).

It is rare that one family of orientations is dominant for all the grains. Instead, a certain fraction of grains has a certain orientation and another fraction has a different one. The texture of the sheet can then be described in terms of the major or ideal family of orientations that are present. Fig. 2.4 demonstrates some of the typical textures that are encountered in rolled steel sheets (44).

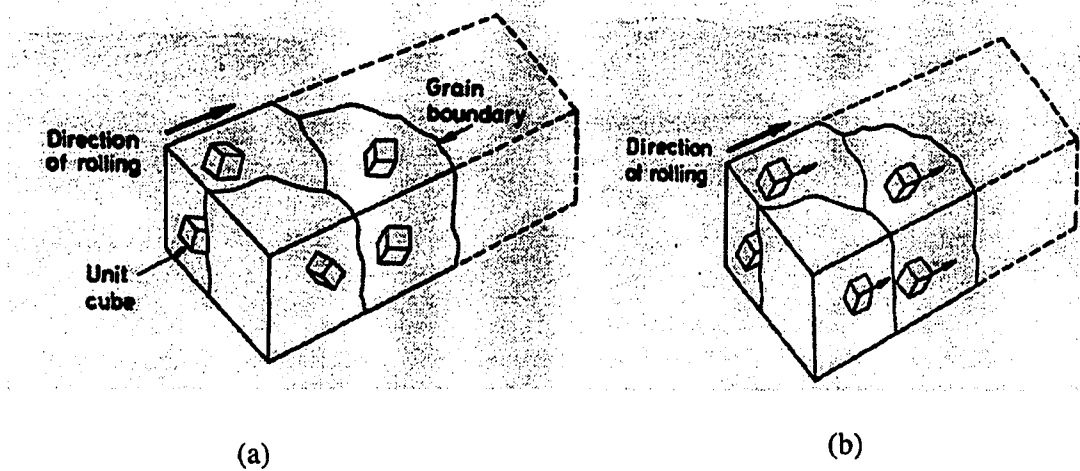


Fig. 2.3 Texture in rolled sheets

- (a) Random orientations
- (b) Preferred Orientations

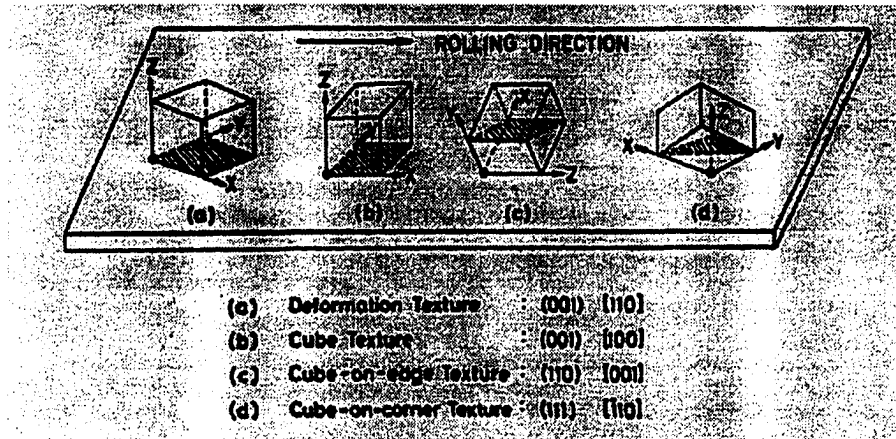


Fig. 2.4 Common textures in low carbon steels (44)

The convention in texture analysis is to specify the preferred orientations of the grains of rolled sheets by the orientations of faces and directions of an ideal single crystal (Fig. 2.5a) with respect to the plane of the sheet and its rolling direction. Crystals frequently have polyhedral shapes bounded by flat faces which they acquire during the solidification process. The fact that these faces have different orientations is a consequence of the periodicity of crystal's internal arrangement of molecules or atoms. This periodicity is the key feature of all crystals and forms their basic definition (a crystal is defined as consisting of atoms arranged in a pattern that repeats itself periodically in three dimensional space (54)).

As an example, Fig. 2.5b demonstrates the geometrical arrangements of atoms in the sodium-chloride structure, where the patterned arrangement of sodium and chloride ions re-

peats itself over and over again throughout the three dimensional space of the crystal. The crystal faces, therefore, can be thought of as sets of crystallographic planes representing the stacking of layers of atoms. During crystal growth, it is easier for the crystal to add molecules on some planes than others, and the corresponding crystal faces, therefore, experience greater development (54).

The face orientations are expressed in terms of Miller indices which describe the directions of crystallographic planes in a crystallite coordinate system. For cubic materials, this coordinate system is formed by placing three mutually perpendicular axes through one of the corners of a unit cube called a unit cell (Fig. 2.5c), which can be considered as a 'template' representing the atomic arrangement of the crystal. A crystallographic plane is specified in terms of the length of its intercepts on the three axes, measured from the origin of the crystallite coordinate system (Fig. 2.5d).

The Miller indices of a plane (hkl) are the reciprocals of the intercepts reduced to their lowest common denominator. The plane ABCD in Fig. 2.5d is, therefore, (010). Due to symmetry of atomic arrangements in the crystal (and consequently in the unit cell), a group of crystallographic planes can be considered equivalent. For instance, there are six equivalent planes of the type (100), having the indices (100), (010), (001), ( $\bar{1}00$ ), ( $0\bar{1}0$ ), ( $00\bar{1}$ ). The family of equivalent planes is indicated by the notation {100}. In cubic crystals, the crystallographic directions are defined as normals to their corresponding planes and are shown by integers in brackets [uvw] with the family of equivalent directions being indicated by <uvw>. As mentioned previously, textures of rolled sheets are specified with respect to the orientation of an ideal single crystal. This orientation is defined by the crystallographic plane that is parallel to the plane of the sheet and the direction which is parallel to the rolling direction. For example, the ideal cube-on-corner texture shown in Fig. 2.4 is indicated by (111)[110]. This means that grains (or crystals) in the sheet have gained a preferred



orientation or have been rotated in such a way that their (111) faces (as shown in Figure 2.5a) are now in the plane of the sheet (i.e. parallel to the rolling direction) and their [110] directions are parallel to the rolling direction.

## 2.2.2 Experimental Texture Analysis

**2.2.2.1 Pole Figures** The main objective behind generating a pole figure is to map the distribution of grain orientations over as complete a section of orientation space as possible. In other words, it is recognized that real materials contain other than the ideal orientations, and one wishes to quantify the relative probability of occurrence of all possible orientations, ideal or not. There are several techniques available to accomplish this (53, 55). The most common one involves X-ray diffraction using the Schultz-reflection method. Here, a small, typically a 1 in. square sample (2.5 x 2.5 cm cut out of the sheet of interest), with polished or etched surfaces is placed in a goniometer, which contains the X-ray transmitter and the receiver. The diffracting normal, which is the normal to the reflecting crystallographic planes of interest ( $\{hkl\}$ ) is fixed by the goniometer, and it bisects the angle between the incident and diffracted X-rays (Fig. 2.6a). The Bragg angle which defines the separation between the transmitter and the receiver (by the distance between the  $\{hkl\}$  planes) is also fixed. The variations of the diffracted X-ray intensities are then measured as a function of the relative orientation of the steel sample with respect to the diffractometer geometry, with the intensity being proportional to the number of crystallites whose orientation in the sample is such that they contribute to the diffraction at a particular orientation of the sample with respect to the goniometer.

Essentially, two simultaneous rotations takes place. The sample is tilted through an angle  $\alpha$  (in 5 degree increments usually up to 75-85 degrees (53)) to align the rolling direction with the diffracting normal. This generates a 'radial scan' of the orientations of the grains on

---

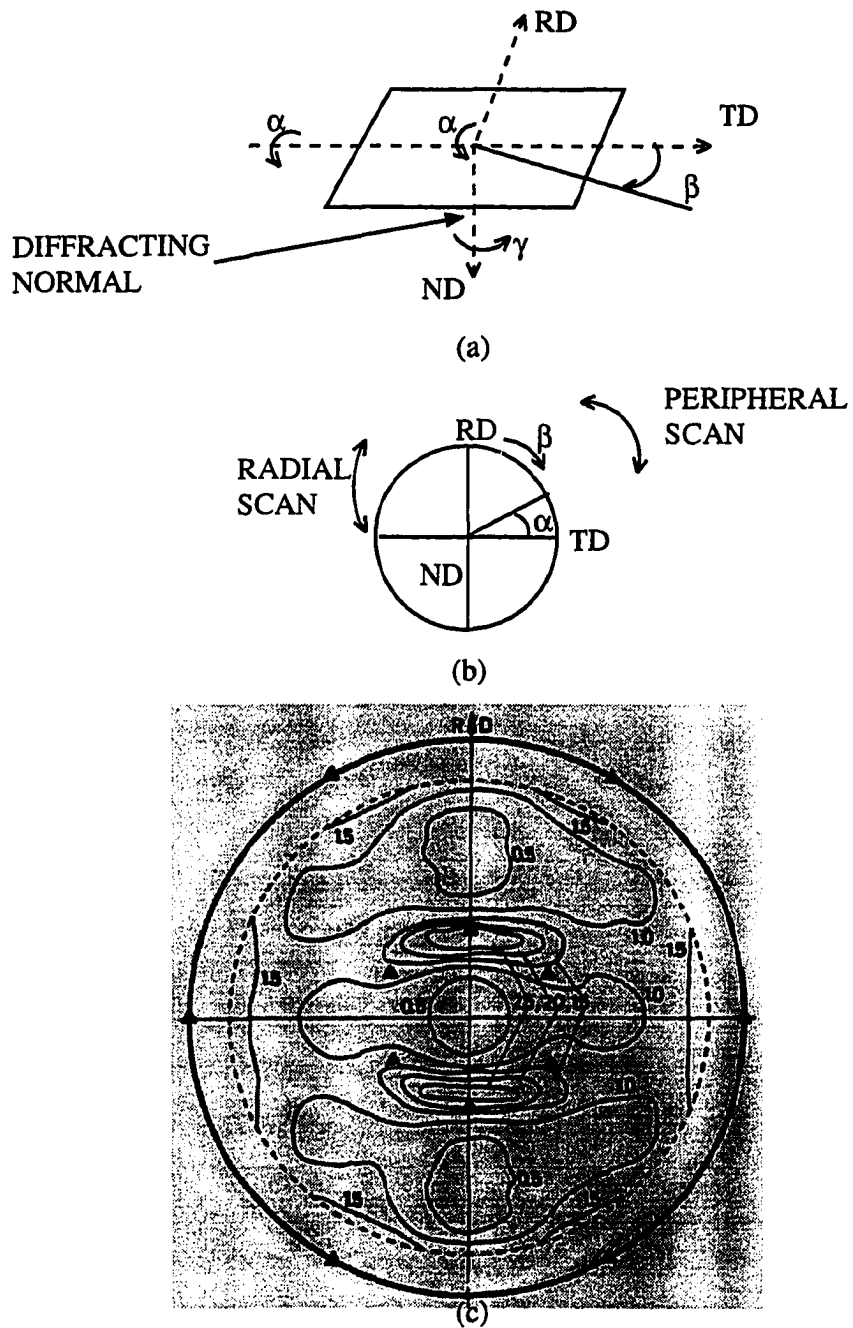


Fig. 2.6 Pole figures:

(a) Sample coordinate, (b) Pole figure scans, (c) (110) pole figure (44)

the two dimensional projection of the orientations (poles) on the stereographic circle from rolling direction (RD) to normal direction (ND), Fig. 2.6b. The second rotation takes place through the angle  $\beta$ , to align the transverse direction of the sample with the diffracting normal. In so doing, a peripheral scan of the orientation of grains takes place on the stereographic circle. The simultaneous scanning of  $\alpha$  and  $\beta$  allows the iso-intensity contour lines to be plotted on the stereographic circle. A typical pole figure is shown in Fig. 2.6c (44). The degree of sharpness of texture is determined by comparing the intensities measured with the intensities of the material with a random texture and are indicated on the contour lines within the stereographic circle by ( $\times$  random) notation. It is customary to carry out standard data reduction techniques including some corrections for background effects, beam narrowing and normalizing procedures (53).

Pole figures are essentially a statistical, 2-D representation of the 3-D orientation of grains and, therefore, are incomplete and subject to interpretation. The experimental pole figures are usually interpreted by comparing them with the 'ideal' pole figures. Here, various  $\{hkl\}$  reflecting pole figures (i.e. (110), (111), etc.) have been theoretically determined for ideal crystal orientations. By directly comparing the high intensity locations of the experimental pole figures with the ideal ones, the degree and type of texture can be interpreted. For instance, the (110) pole figure shown in Fig. 2.6c reveals the  $\{111\}\langle 112\rangle$  texture in the AKDQ sample that was used. The ideal positions are shown by black triangles in the figure.

**2.2.2.2 Orientation Distribution Functions (ODF)** In order to overcome the shortcomings of pole figures, an approach using a statistical distribution technique has been developed. This technique uses the orientation distribution function (ODF), which is a three dimensional representation of the rolled sheet's texture. Theoretically, in order to have a complete representation of grain orientations, a six dimensional space is needed: an xyz reference frame for the rolled sheet and an hkl reference frame for the crystals. However, it is

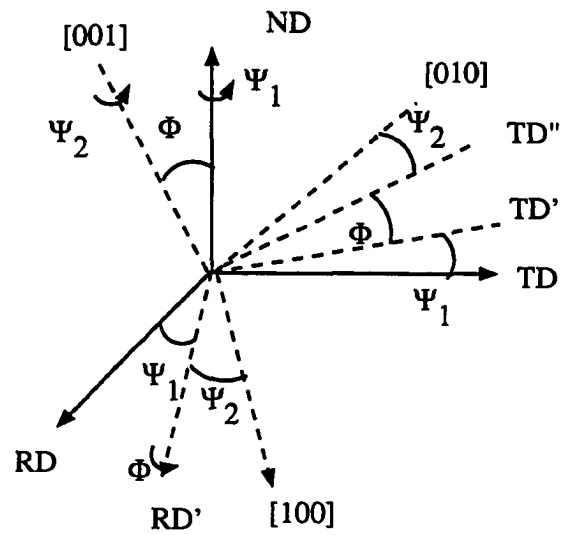
possible to transform the sample (rolled sheet) coordinate system into the crystallite coordinate system through three rotations defined by the Euler angles. As a result, characterization of the texture takes place in a three dimensional space of the crystallite with respect to the sample.

As mentioned before, this technique was developed independently by Roe (31) and Bunge (32). The two approaches are essentially identical. The differences are due to variations in a) the definition of Euler angles used; b) the norm conventions of the ODF and pole figures; c) the phase and norm conventions of polynomials which appear in the representation of the ODF and d) the way the crystal and sample symmetries are handled (56). In this work, from this point on, the two terminologies will be used interchangeably. In this section, however, the Bunge's approach will be used almost exclusively to describe the basic fundamentals behind the technique. In Chapter 4 where the ultrasonic approach is described, Roe's terminology will also be used.

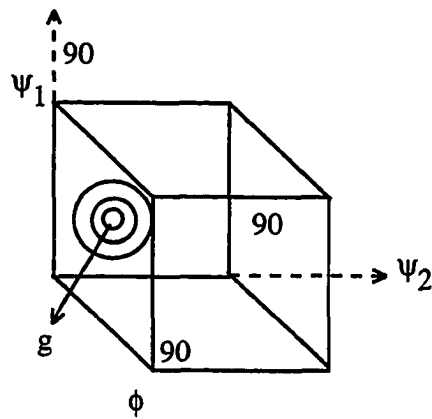
Figure 2.7a shows a set of three rotations that transform the sample coordinate system into the crystal coordinate system. These rotations define the Euler space. The ODF is defined as the volume fractions of the crystallites with a particular orientation  $g$ , which is defined by the three Euler angles of  $(\Psi_1, \Phi, \Psi_2)$ :

$$(2.1) \quad ODF = \frac{(dV/V)}{(dg)} = f(g) = f(\varphi_1, \Phi, \psi_2)$$

where  $dV/V$  is the volume fraction of grains with orientation  $g$  within an infinitesimal element of the Euler space,  $dg$ , and  $f(g)$  is the ODF. The Euler orientation,  $g$ , for one crystallite is, therefore, a point in the Euler space. For an aggregate of crystallites, values of  $g$  with equal probability (i.e. constant values of  $f(g)$ ) will be represented by contour lines



(a)



(b)

**Fig. 2.7 Euler space transformation:**  
 (a) Transformation from sample into crystallite coordinate system  
 (b) Representation of a single crystallite or an aggregate of crystallites

(Fig. 2.7b). The ODF,  $f(g)$ , is normalized in multiples of the random density and it is expressed in random units. The ODF for a random texture is thus 1:

$$(2.2) \quad \int f(g) dg = 1$$

There are two basic classes of symmetries involved in ODF analysis for polycrystals. One is the crystal symmetry (e.g. cubic for bcc and fcc crystals) and the other is the symmetry due to the sample. For the rolled sheets of interest in this work, the latter is generally assumed to be orthorhombic. Section 2.2.1 gave a brief description of the cubic symmetry where a number of crystallographic planes may be equivalent. For cubic materials, there are 24 different ways of representing the same crystal (depending on where the crystal coordinate system is placed). For rolled sheets, the orthorhombic symmetry (3 perpendicular mirror planes) yields 4 different ways of representation. These symmetries combined, result in 96 regions of Euler space where the ODF's are equivalent. This range, however, is usually reduced by considering only the regions of  $\Psi_1 \geq 0$  and  $(\Phi, \Psi_2 \leq 90)$ . Therefore, the analysis is essentially carried out over the mentioned range (0-90) shown in Fig. 2.7b.

Usually three pole figures (obtained through X-ray or neutron diffraction techniques) are used as inputs to calculate the ODF. To extract the texture data from pole figures, a technique, called pole figure inversion is used. The most common technique is the series expansion approach (31, 32), where the known pole densities,  $P_{hkl}(\alpha\beta)$ , are measured on an (hkl) pole figure with  $\alpha$  and  $\beta$  being the sample coordinate angles (Fig. 2.6a) and the unknown ODF's are expanded in terms of spherical harmonics (31, 32). Spherical harmonics are orthogonal functions which may be expressed as polynomials of trigonometric functions of the

Euler angles. They represent the 3-D ODF in much the same way as a Fourier series represents a function of a single variable. In Bunge's notation (32):

$$(2.3) \quad f(g) = \sum_{\lambda=0}^L \sum_{\mu=1}^{M(\lambda)} \sum_{\nu=1}^{N(\lambda)} C_{\lambda}^{\mu\nu} T_{\lambda}^{\cdot\cdot\mu\nu}(g)$$

where  $T_{\lambda}^{\cdot\cdot\mu\nu}$  are the generalized spherical harmonics which are invariant with respect to the crystal and sample symmetries (the two dots on the top left denote the sample symmetry and the dot to the right denotes the crystal symmetry).  $M(\lambda)$  and  $N(\lambda)$  are the number of independent symmetrical harmonics which Bunge has indexed for different crystal structures (32). With these parameters as *a priori*, the independent harmonics are in effect 'selected' and the computation time is reduced. The  $C_{\lambda}^{\mu\nu}$  terms are the coefficients of the expansion and are to be calculated from the texture data obtained from pole figures. Once calculated, they play an important role in ODF analysis. This role will be discussed further in later sections and in Chapter 4.

In order to calculate the coefficients (referred as texture coefficients in what follows), an (hkl) pole figure can be represented as a series of surface spherical harmonics of the rolled sheet symmetry:

$$(2.4) \quad P_{hkl}(\alpha\beta) = \sum_{\lambda=0}^L \sum_{\nu=1}^{N(\lambda)} F_{\lambda}^{\nu}(hkl) K_{\lambda}^{\nu}(\alpha\beta)$$

where,  $F_{\lambda}^{\nu}(hkl)$  are the coefficient of the expansion and  $K_{\lambda}^{\nu}(\alpha\beta)$  are the surface spherical harmonics. The texture data obtained from pole figures is related to the ODF's by recognizing that the pole figure is essentially a two dimensional projection of the ODF. In other words, the pole densities are the integral of ODF:

$$(2.5) \quad P_{hkl}(\alpha\beta) = \frac{1}{2\pi} \int_0^{2\pi} f(g) d\gamma$$

Equation 2.5 is true as a result of the main shortcoming of the characterization of texture by pole figures. This shortcoming is due to the fact that the diffraction process 'misses' some of the possible orientations of crystals since no information is obtained by the rotation of the sample around the normal to reflecting planes (angle  $\gamma$  in Fig. 2.6a) (32). By incorporating Eqn. 2.3 and 2.4 in Eqn. 2.5, one obtains a system of linear equations between the known coefficients,  $F_{\lambda}^{\nu}(hkl)$  and the texture coefficients:

$$(2.6) \quad F_{\lambda}^{\nu}(hkl) = \frac{4\pi}{2\lambda+1} \sum_{\mu=1}^{M(\lambda)} C_{\lambda}^{\mu\nu} K_{\lambda}^{\mu}(hkl)$$

Having experimentally obtained  $F_{\lambda}^{\nu}(hkl)$  from the pole densities through Eqn. 2.4, a least

---

square technique is usually used to solve this equation and calculate the texture coefficients and the ODF's. Computer programs are now routinely used in the calculation of the ODF's and they are gaining increasing use in industrial texture control operations (56).

**2.2.2.2.1 Texture Interpretation using ODF's** Figure 2.8 shows a typical ODF calculated for a 95% cold rolled steel sample (32). The computed ODF's can be used in three basic ways to interpret the texture of the sheet: a) By examination of the full ODF (by examining the orthogonal projections of the 'texture tube' in Euler space), b) By examination of the ideal fiber tubes, and c) By examining the so-called 'skeleton' line. These approaches are discussed in more detail below.

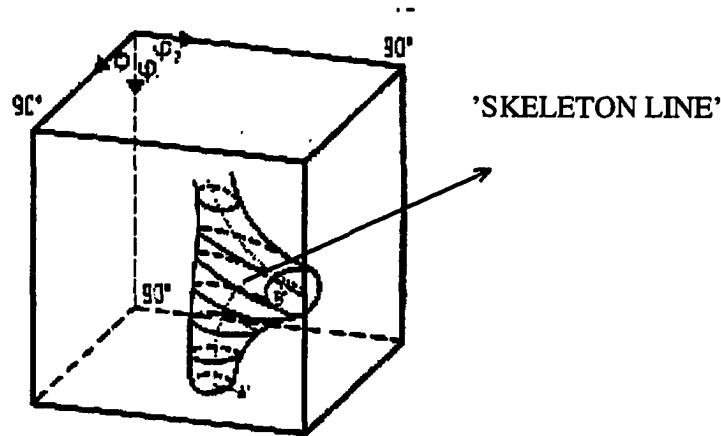


Fig. 2.8 A 3-D ODF of a cold rolled steel sample (32)

The first approach involves study of the cross sections of the measured 'texture tube' on polar plots and comparing them with the determined ideal ones. These orthogonal projections are usually called by the Euler angle of interest at which the cross section was selected. For the commonly observed textures of rolled sheets, it is customary to examine the  $\Psi_2=45^\circ$  section of the ODF since the important  $\{111\}$  textures (which cause the rolled textures to be



tubular in Euler space) are located there. Figure 2.9 shows the  $\phi=45^\circ$  section (in Roe's terminology, this is equivalent to the  $\Psi_2=45^\circ$  section in Bunge's notation) of the ODF for an AKDQ steel which was measured by Morris et al. (57). The theoretically predicted ideal orientations are also shown on the same figure. Using the calculated intensities of the main orientations and locating their positions in the Euler space using the ideal plots, the type and degree of texture of the sheet is readily obtained. It is evident that this texture is very strong around the line running parallel to  $\Psi$  at  $\theta=55^\circ$ , which includes all the orientations with their (111) planes parallel to the rolling direction (their [111] normals are parallel to the normal direction). This line which is denoted as [111] || ND on the ideal diagram, is one of the ideal fiber lines, and is the so-called  $\gamma$ -fiber. This matter will now be discussed further.

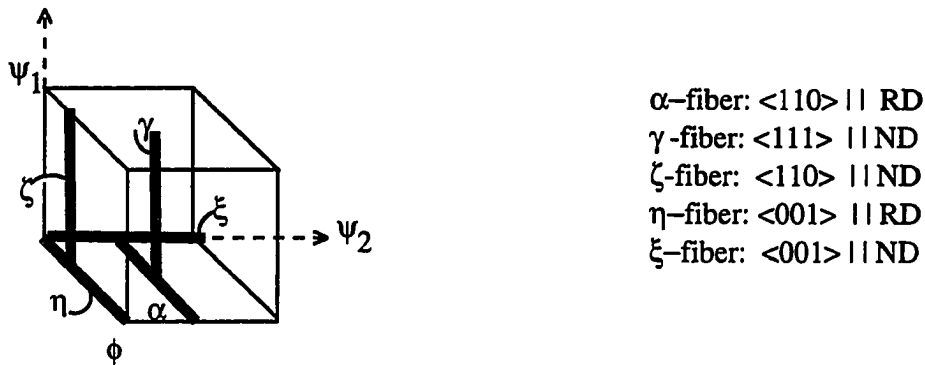


Fig. 2.10 Ideal fibers in Euler space (58)

Figure 2.10 shows an overview of these lines which have been identified for low carbon steels (58). Some of the more important fibers for rolled sheets are the  $\gamma$ -fiber and the  $\alpha$ -fiber. The  $\gamma$ -fiber is located in the  $\Psi_2=45^\circ$  section at  $\phi=55^\circ$  and runs along  $\Psi_1$ . It describes rotations around the [111] axis parallel to the normal direction (it represents all the orientations with their (111) planes parallel to the rolling directions, the so called cube-on-corner

textures). This fiber is useful in characterizing the rolled and recrystallization textures. The  $\alpha$ -fiber is located in the  $\Psi_1=0^\circ$  section at  $\Psi_2=45^\circ$  running along  $\phi$ . It represents the so-called RD fiber or all the orientations obtained by rotation around the [110] axis parallel to the rolling direction. This fiber is useful in studying hot and cold rolled textures as well as recrystallization textures. By rotating the sheet through appropriate Euler angles pertinent to these fibers (by moving along these fiber lines or tubes, Fig. 2.8 and Fig. 2.10) and identifying the orientations with significant intensities, important quantitative information regarding the texture, its main orientations and also the secondary components around the main orientations can be obtained.

In the third approach, which is not entirely independent from the above, the maximum intensity points in the  $\Psi_1$  sections are connected in order to elucidate the principal features of the texture. This forms a line in the Euler space which is called a 'skeleton' line. 'Skeleton' line is shown as dotted lines within the 'texture-tube' in Fig. 2.8 (32). Each point on this line represents a certain preferred orientation. The orientation density along the 'Skeleton' line varies and this may be seen by plotting the peak intensities versus  $\Psi_1$ . The 'Skeleton' line is usually compared with the measured  $\gamma$ -fiber in order to detect deviations from this fiber. These deviations are due to the spread caused by the secondary components that may also be of significance. Figure 2.11 shows the 'Skeleton' line of an AKDQ steel which Bunge generated in one of his pioneering works (59). As can be seen from the figure, the main feature of the texture is a (111)[110] texture with intensity of 6.5x random. However, the skeleton line deviates from the  $\gamma$ -fiber (not shown here) at an orientation which is 5 degrees away from the (111)[121] orientation (also see the  $\gamma$ -fiber in the ideal section in Fig. 2.9). This secondary component which in later works by other investigators has been denoted as (554)[225], is an important orientation in AKDQ steels and particularly in some types of stabilized IF steels where it plays an important role in their earing behavior.

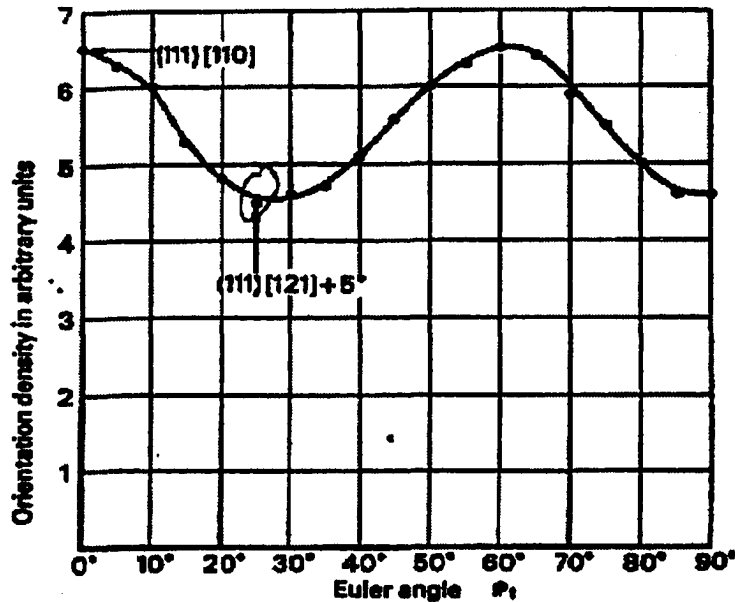


Fig. 2.11 "skeleton line of an AKDQ steel sample (59)

**2.2.2.2.2 ODF and Texture-Dependent Properties** The power of the ODF analysis is not limited merely to quantitative texture characterization. It has a broader application when the texture-dependent properties are considered. As mentioned in Chapter 1, texture creates anisotropy in both the plastic and elastic properties. These properties include Young's modulus, plasticity, magnetism and thermal or electrical conductivity (32). The texture information carried by the ODF can be used as a weighting function in calculating the average macroscopic anisotropic properties. This information is obtained through the texture coefficients,  $C_{\lambda}^{\mu\nu}$ , in Eqn. 2.3, described briefly in previous sections. These coefficients charac-

terize the symmetry of the texture in a complex way. For example they can be used to describe the normal anisotropy, or the degree of 2-fold and 4-fold symmetries of r-values or Young's modulus in the plane of the sheet (  $C_4^{11}$ ,  $C_4^{12}$  and  $C_4^{13}$  ). It has been known that only these three texture coefficients are needed in order to describe the angular variations of elastic and plastic properties of rolled sheets (32). Chapter 4 will describe this aspect of the ODF analysis in more detail, and relate it to the ultrasonic technique where the series expansion of texture is truncated at the fourth term ( $l=4$ , with only  $C_4^{11}$ ,  $C_4^{12}$  and  $C_4^{13}$  present for cubic materials).

### 2.2.3 Common Textures In Low Carbon Steels

The final texture of annealed low carbon steel sheets is composed mainly of the {111} fiber. Although every stage of processing is important in development of this fiber, this texture is mainly the parent texture which is developed during the cold rolling operation and it is only modified by changes during annealing. These changes occur over the course of recovery, recrystallization and grain growth (16,44-46).

During the cold rolling process, the texture of ferrite becomes stronger and sharper with increasing deformation and it is developed most easily to accommodate the complex slip process (16). As a result, one of the major orientation spreads observed in cold rolled steels, is a partial  $\alpha$ -fiber with {001}, {112} and {111} planes with their  $\langle 110 \rangle$  directions parallel to the rolling direction. The second major fiber is the  $\gamma$ -fiber of {111} $\langle 110 \rangle$ ,  $\langle 123 \rangle$  and  $\langle 112 \rangle$  components, Fig. 2.9 (46).

Annealing involves the three major stages of recovery, recrystallization and grain growth or secondary recrystallization. During recovery, the steel reverts to a condition in which the

mechanical and physical properties tend toward the undeformed state, but no major change in texture takes place with a decrease in dislocation density and their eventual annihilation (16). When the process of recrystallization (nucleation of new perfect, dislocation-free, grains) starts, in addition to changes in properties, a major change in texture also occurs whose origin is not well understood and still disputed. A review of this matter can be found in reference (44).

Essentially, the process leads to a substantial growth of the  $\{111\}$  components, and to a lesser degree, the  $\{110\}$  components at the expense of others. There are three basic theories of oriented nucleation, oriented growth nucleation and a mix of the two which are used to explain this change. It seems that the latter agrees best with the experimental observation (16). According to this theory, the internal stored energy and dislocation structure, present in the various deformed grains of the cold rolled sheets, provide the driving force for recrystallization. The level of these factors varies according to the orientation of the deformed grains. This orientation dependence, therefore, is responsible for biasing the recrystallization process in favor of the growth of certain texture components (46).

Figure 2.12 shows some of the common orientations traditionally observed and reported in annealed low carbon steels (44). As mentioned in the beginning of this section, the texture in all of these steels is essentially fibrous, resembling an almost ideal  $\gamma$ -fiber (especially in IF and AKDQ steels). The specific dominant orientation generally includes  $\{111\}\langle 110\rangle$  components with strong secondary components of  $\{112\}\langle 110\rangle$ ,  $\{111\}\langle 112\rangle$  (not shown in the figure), and  $\{554\}\langle 225\rangle$  and  $\{223\}\langle 472\rangle$  (the latter mostly in some IF steels (60)). Other common orientations include  $\{100\}\langle 001\rangle$  and  $\{110\}\langle 001\rangle$  (called deformation and Goss components, the latter not shown in Fig. 2.12).

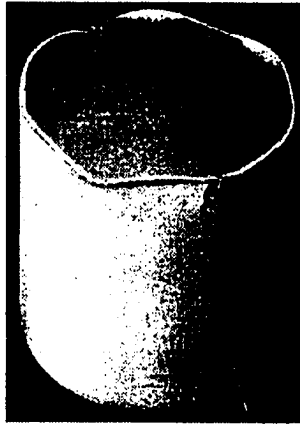
As far as the magnitude of the average plastic strain ratio (representing normal

anisotropy) is concerned, the strong effect of all of these orientations on  $\bar{r}$  is well known and understood (16, 25, 44-46). The strong  $\{111\}$  fiber is responsible for sharp textures and high  $\bar{r}$  in AKDQ and IF steels. The  $\bar{r}$  decreases from IF steels (being the highest) to HSLA steels (being the lowest) in accordance with the decreasing trends of sharpness in texture of IF and AKDQ steels (the highest) to that of HSLA (the weakest). This is due to the growth of the deformation and Goss components in the latter (due to the particular processing of HSLA steels) which has a negative effect on the average plastic strain ratio,  $\bar{r}$ .

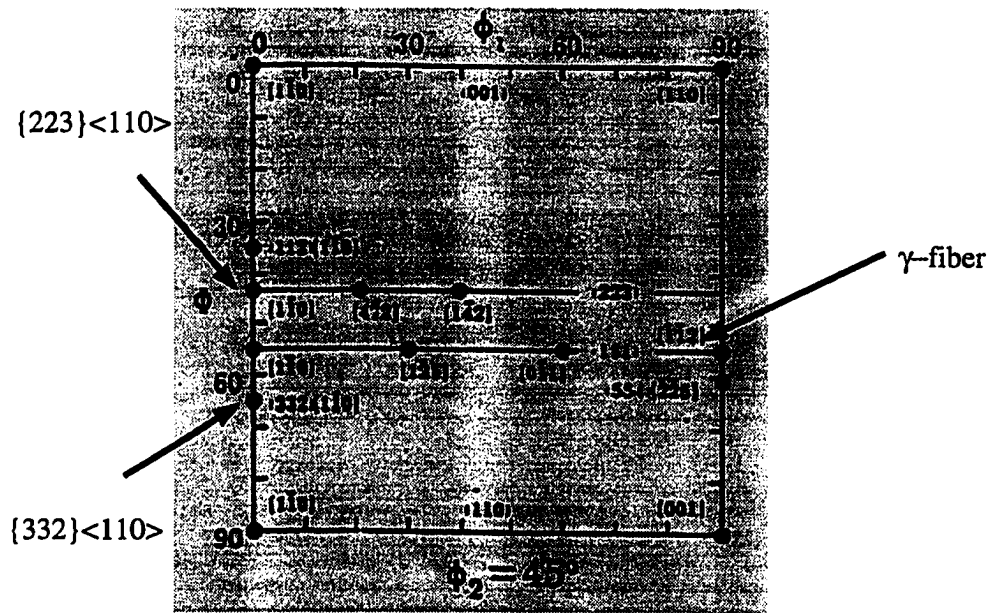


Fig. 2.12 X-ray intensities of the commonly observed textures in low carbon steels (44)

The earing phenomenon, which is the manifestation of planar anisotropy and which is usually characterized by  $\Delta r$ , is not as well understood (40, 60). It has been observed to commonly occur at 0 and 90 degrees with respect to the rolling direction (2-fold earing) or at 0, 90, 180 and 270 degrees with respect to rolling direction (4-fold earing), (16). However, there are some uncommon cases of titanium-stabilized IF steels which also show a 6-fold symmetry (Fig. 2.13a) with 6 ears developing at 0, 60, 120, 180, 240 and 300 degrees with a



(a)



(b)

Fig. 2.13 Earing in some IF steels

(a) 6-fold earring (62)

(b) Ideal  $\psi_2=45^\circ$  plot (40)

respect to the rolling direction (62). The origin of the earing phenomenon may be explained on the basis of the nonuniformities of orientations along the  $\gamma$ -fiber of low carbon steels and the spreads around the main components of the secondary components. These secondary components (i.e.  $\{554\}\langle 225\rangle$  in AKDQ steels) contribute to the usually distorted 'texture tubes' observed in ODF of low carbon steels (Fig. 2.8). Had the  $\gamma$ -fiber been a perfect ideal fiber, the tube would have been a perfect cylinder with circular cross section (60).

Using ODF analysis, Daniel (60) and Daniel and Jonas (61), have recently examined the texture of a number of deep drawing type steels. The IF steels that were investigated included two types of the traditional ones having 4-fold earing behavior (denoted as IF1) and the type that shows a 6-fold earing phenomena (denoted as IF2 in their work). Figure 2.14a-d shows their findings as regards the main and secondary texture components of some of the steels that were investigated.

As shown in Fig. 2.14a and b, the  $\alpha$  and  $\gamma$ -fiber diagrams identify the main and secondary orientations that have been observed traditionally, as shown previously in Fig. 2.12. The  $\gamma$ -fiber data shows that these textures are essentially composed of  $\gamma$  components with texture sharpness increasing as one moves from HSLA to IF steels. The  $\{111\}\langle 110\rangle$  is the dominant component with  $\{111\}\langle 112\rangle$  also being present. The  $\alpha$ -fiber data (Fig. 2.14a) shows the same components present in Fig. 2.14b, with  $\{112\}\langle 110\rangle$  components also being present. Moreover, the  $\alpha$ -fiber data demonstrates that IF and AKDQ steels show a spread towards the secondary components of  $\{223\}\langle 110\rangle$  and  $\{332\}\langle 110\rangle$ , respectively. The 'Skeleton' lines for IF2 and AKDQ steels are shown in Fig. 2.14c and d. It can be seen that the 'Skeleton' line, depicted by the dotted lines, deviates from the  $\gamma$ -fiber at the  $\{554\}\langle 225\rangle$  orientation (shown as black triangles in the Figs. 2.14c and d). This deviation is larger in IF2 steels than for AKDQ steels.

Based on these findings, the authors attributed the 6-fold earing phenomenon to the presence of these secondary components and the sharpness of textures in IF2 steels. They reasoned that the 6-fold earing observed in IF2 steels is due to the fact that the  $\langle 111 \rangle$  single crystals exhibit 6-fold symmetry in their plastic properties, and that this is more evident in IF2 steels, since their  $\{111\}$  textures are sharper. In the case of AKDQ and IF1 steels, the 6-fold symmetry of the  $\alpha$ -fiber (RD fiber) is obscured by the larger dispersion around this fiber axis and by the presence of the secondary components such as  $\{332\}\langle 110 \rangle$  and  $\{223\}\langle 110 \rangle$ .

The foregoing may be clarified by the examination of the  $\gamma$ -fiber shown in Fig 2.13b. It can be seen that the symmetrically equivalent orientations occur at 60 degree intervals along the  $\gamma$ -fiber, (only two of  $(111)[1\bar{2}1]$  and  $(111)[\bar{1}\bar{1}2]$  at  $\Psi_1=30$  and 90 degrees and  $(111)[1\bar{1}0]$  and  $(111)[0\bar{1}1]$  at  $\Psi_1=0$  and 60 degrees are shown in the figure) which corresponds to the observed 6-fold earing in the aforementioned IF steels. A similar examination of the  $\alpha$ -fiber reveals that symmetrically equivalent orientations occur at 90 degree intervals (only one of  $(001)[1\bar{1}0]$  and  $(001)[1\bar{1}0]$  at  $\phi=0$  and 90 degrees are shown) corresponding to the traditional 4 and 2-fold symmetries observed in low carbon steels, with the secondary components of  $(332)[110]$  and  $(223)[110]$  also present.

This finding has important implications with regard to the effects of the usual early truncations on the series expansion technique which is implicit in the ultrasonic technique. As mentioned before, only three texture coefficients have been known to be sufficient in calculating the plastic properties of the rolled sheet from its texture. Daniel and Jonas (61) have concluded that in order to completely describe the 6-fold symmetry of texture in IF2 steels, more texture coefficients than those already measured with the ultrasonic technique are needed. This matter will be examined more closely in Chapter 5, where some ideal orientations will be simulated and their effects on  $r$  and its planar variations examined.

## CHAPTER 3

### DESTRUCTIVE R MEASUREMENT TECHNIQUES

The most commonly used test to measure drawability index in formability characterization tests is the tensile test. The simulative tests such as the Swift cupping test, as mentioned in Chapter 1, do not measure  $r$ -values directly. Moreover, their sensitivity to lubrication and friction considerations and the number of varying size blanks which have to be tested, make them impractical for routine drawability testing in press shops. Tensile tests, on the other hand, lead to the measurement of  $r$  through simple direct or indirect calculation of strain ratios in tensile coupons (Eqns. 1.2 and 1.4) which is suitable for routine characterization of steel formability. The tension test is also able to provide a complete measurement of the mechanical properties of the material such as strain hardening coefficient, yield and tensile strengths and total elongation at fracture. Another technique which is also in use in formability characterization of steels, involves the Modul- $r$  instrument. This instrument measures  $r$ -values through a magnetically excited, mechanical resonance technique taking advantage of a proven statistical correlation between elastic and plastic anisotropy as discussed in Section 1.4 in Chapter 1. These two techniques are described in the next section.

#### 3.1 Tensile Test

Although the tensile test is simpler and more practical than the biaxial simulative tests, the problems associated with its measurements are not compatible with the standards needed in industrial quality control operations. This is evident by the number of collaborative research and round robin test programs that various research groups have undertaken over the past three decades to explain the problems experienced by different laboratories in measuring  $r$ -values using tensile tests. A review of these tests may be found in reference (63). As a

result, there is a considerable amount of data in the literature regarding various aspects of tensile measurement of the plastic strain ratio.

These problems can be divided into two basic groups. The first group is concerned with the variability in  $r$  measurements and the experimental errors commonly seen from laboratory to laboratory. More specifically, this entails the questions of procedures in preparing samples, the choice of geometry, and the limitations of accurate strain-reading devices (micrometers, microscopes, extensometers), operator skills and test procedures and conditions (13, 63). These are demonstrated by the results of a round robin test program which was performed by 13 participating laboratories (from Europe and the U.S.), Fig. 3.1.

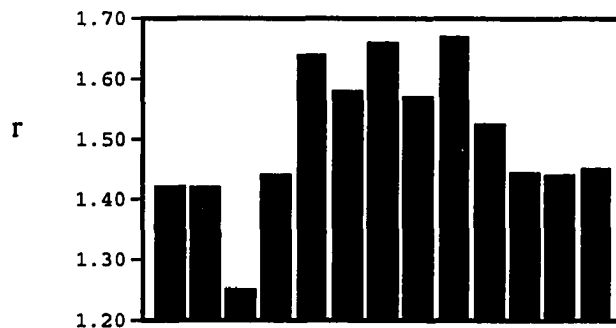


Fig. 3.1 Variability in tensile measurements of  $r(0)$ , (13)

This program was sponsored by the Materials' Working Group of the International Deep Drawing Research Group, I.D.D.R.G., in 1967 (13). Samples were cut out of the same batch of a uniform steel sheet and were distributed among the laboratories to perform the tensile tests according to their own procedures. As Fig. 3.1 demonstrates, a considerable amount of variation from laboratory to laboratory was obtained with the maximum difference for  $r$ -

values measured in the rolling direction being 0.43 and 0.38 for  $\bar{r}$ . Similar variations were seen in a round robin test sponsored by The North American Deep Drawing Research Group, N.A.D.D.R.G. in 1988 (60).

The second group of problems involves issues such as the evolution of anisotropy during the early straining in a tension test and its impact on  $r$ , the strain dependence of  $r$  over various elongation ranges and the differences between direct and indirect calculations of  $r$  (64, 65). There have also been discussions regarding the appropriateness of the present definitions of  $r$  as a measure of normal anisotropy with alternative definitions suggested (66).

### 3.1.1 Test Procedure

The general procedure in tensile  $r$ -value measurements includes the careful preparation of sample geometries with appropriate gage marks or indentations, the straining of the samples to a specified strain state in a tensile machine and the reading of the prestrained and poststrained dimensions.

Three specimen are usually sheared or cut from steel sheets in the three directions 0, 45 and 90 degrees with respect to the rolling direction duplicates being preferred. The geometry of specimen varies depending on the particular standard used. Figure 3.2 shows the suggested ASTM geometries of standard A, B and C samples (67). Generally, the samples are sheared or cut in a rectangular shape with parallel sides (samples B and C) or they can be machined to have reduced test sections (sample A). The ASTM recommended indentation technique is the Vickers diamond test, although other techniques are also used.

A common loading equipment used is a 10000 or 5000 lb. (4530 or 2265 kg) capacity Instron machine (51). The specimen is inserted into the grips which are connected to the cross head of the tensile machine. As the cross head moves, the specimen is strained with loads being measured by a load cell (Fig. 3.3). In general, the speed of the cross head and,

therefore, the strain rate chosen depends on the material. However, for  $r$  measurements on low carbon steels, the recommended ASTM traverse rate is a maximum of 0.008 in/s (0.2 mm/s). The usual elongations for  $r$  measurements in a tensile test are between 10 and 20%, depending on the steel grade. The ASTM suggested practice emphasizes that the measurement should take place in the uniform elongation regime (with loads less than the maximum load). This is with the assumption that  $r$  is independent of strain in this regime. The tests can be conducted by removing the sample and measuring the strains, or it can be continuous, using an extensometer to monitor the strains continuously until fracture occurs (Fig 3.4). For interrupted test procedures (the manual method), depending on the gage length and width, multiple or single measurements of final dimensions are taken using traveling microscopes and precision micrometers. The calculation of  $r$  is performed through either direct or indirect techniques (Eqns. 1.2 and 1.4), however, the indirect technique is preferred, due to the difficulty of accurately measuring thicknesses.

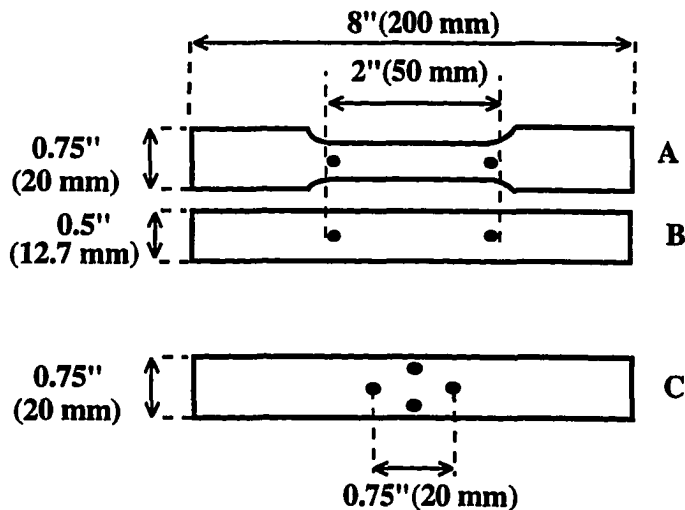


Fig. 3.2 ASTM specifications for sample types A, B and C (67)  
(The dots indicate indentations used in the strain measurements)

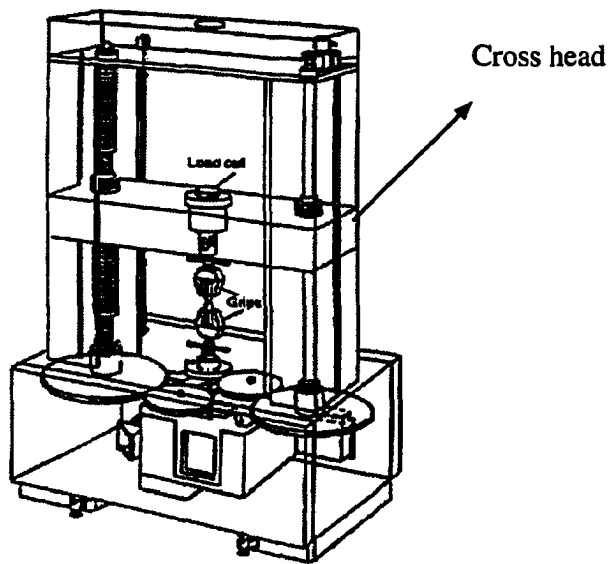


Fig. 3.3 Tensile machine, Courtesy of LTV Steel Company (51)

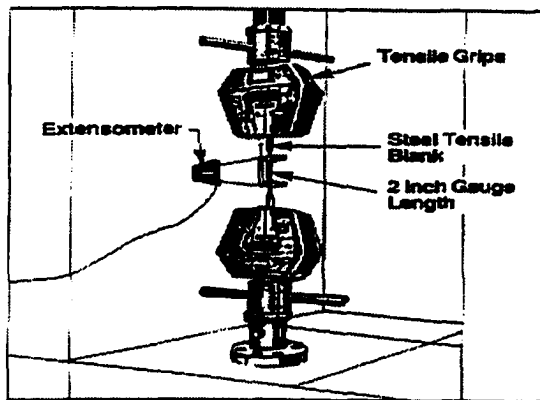


Fig. 3.4 An extensometer, Courtesy of LTV Steel Company (51)

### 3.1.2 Factors Affecting Tensile Measurements of $r$

**3.1.2.1 Specimen Geometry** The slight dimensional differences in ASTM sample geometries seem to have been designed to provide the investigator options in the location of gage marks, the number of length and width measurements that would have to be taken to calculate strains, and the distance of the gage marks from the edges. For instance, the advantage of using specimen C is the fact that the width gage marks are inside the test section and away from the specimen edges which reduces errors in width measurements due to any non-uniformities in the edges. The variation in sample geometries between different standards is, however, large, as summarized by Duncan et al. (63). The effect of this variation on  $r$  measurements has been investigated but it is not clearly known. The main consideration, however, seems to be the lateral restraint on the deformation of the gage section caused by the machine grips or the end of the test specimen. This has led to some observed differences in  $r$  measurements between parallel sided and shouldered specimens. In order to avoid this problem, it has been suggested that the specimens should conform to certain geometrical proportions such as the ratio of their total lengths to their widths and certain minimums in widths. For practical purposes, however, it can be assumed that  $r$  is independent of geometry given that the samples are carefully prepared (63).

**3.1.2.2 Strain Rates and Elongations** According to the review by Duncan et al. (63), there is no evidence that the  $r$ -value is strain rate-sensitive for the range of elongations involved. The strain rates recommended by various standards (ASTM, I.D.D.R.G. and others) and also the ones used by independent researchers (61, 64, 65), all point to the need for a fairly slow rate of no more than .005-.008 in/s (0.1-0.2 mm/s). However, low carbon steels are in general sensitive to the rate of deformation encountered in actual biaxial forming operations (68). Although a high strain rate may have more influence on  $n$  rather than  $r$ , its influence on  $r$  measurements should be investigated. With respect to elongation, it has been

known that the  $r$ -value is in general higher at 10% elongation than at 20% elongation (26). This may be explained on the basis of the strain dependency of  $r$  in the initial straining period. This will be considered further later in this chapter.

**3.1.2.3 Variation of  $r$  with Location in the Test Section** Atkinson (26) measured  $r$  on 15 locations along his test specimen and concluded that the variation can be as much as 0.1 to 0.2. Although others have attributed this observation to experimental error (63), this author concluded the effect was due to variations in local strain hardening behavior of the material. This factor may be more important for manual techniques where interrupted procedures are used.

**3.1.2.4 Changes of Anisotropy during the Tensile test** It has been observed that  $r$  changes with strain in the initial stages of transition to uniform plastic deformation between 0 to 10% strain (Fig. 3.5). There is a considerable amount of data available related to this issue, some of which can be found in references (61), (64) and (65). Although the initial reports were contradictory, it is now generally believed that this dependence is due to instability caused by the formation of Luders bands in steels which show yield point elongation(64).

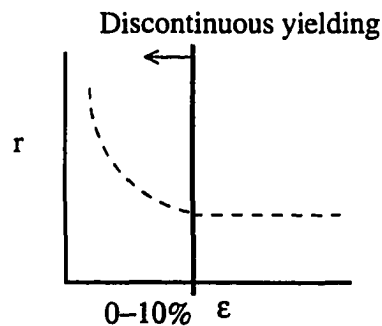


Fig. 3.5 Strain dependence of  $r$

Also some of this instability is thought to be due to the change in strain path that takes place during the tension test relative to the strain paths that were taken during the rolling process (60). The effect of this phenomenon on the accuracy of tensile  $r$  measurements may be significant, particularly when manual tests are done with only one set of strains measured at 15 or 20% elongations.

To examine this effect more closely, one can consider the conventional formula used in the calculation of  $r$ :

$$(3.1) \quad r = \frac{\epsilon_w}{\epsilon_t} = \frac{\ln(w_o/w)}{\ln(t_o/t)}$$

where  $w_o$  and  $t_o$  are the original width and lengths of the sample.

This equation is an approximation to the formula originally proposed by Lankford et al. (15). They observed that the plots of width and thickness strains ( $\epsilon_w$ - $\epsilon_t$ ) were linear over various elongations (i.e. various strains,  $\epsilon_w$ ). They, therefore, considered  $r$  to be the slope of the strain plots and thus an average value of anisotropy. Equation 3.1 which only includes the zero strain state and the strain at 15 or 20% elongation, at best, can only be considered to be a reasonable approximation to the average value. In view of the problems associated with the transition regime, it is obvious that this formula or its variation will not reflect the true slope of the width-thickness or width-length strains. In order to overcome this difficulty, use of linear regression techniques over an appropriate strain range have been suggested by Lake et al. (64) and Liu (65). In this technique,  $r$  is calculated from the slope of the width and length strain plots:

$$(3.2) \quad r = \frac{a}{1-a}$$

where  $a$  is the slope of the strain plots derived from:

$$(3.3) \quad \epsilon_l = b + a\epsilon_w$$

In fact  $a$  is the so called contraction ratio,  $q$ . Therefore,

$$(3.4) \quad a = q = \frac{\epsilon_w}{\epsilon_l} = \frac{r}{r+1}$$

Figure 3.6 is an exaggerated schematic of this effect and shows the different slopes that would be obtained from using conventional and regression methods.

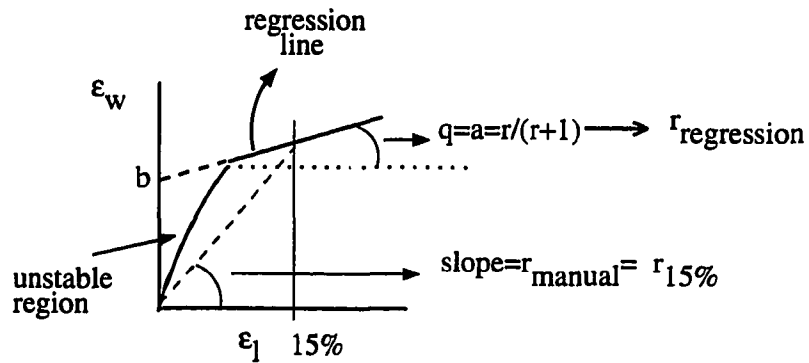


Fig. 3.6 Differences between regression and conventional  $r$ 's at 15% elongation

### 3.1.3 Limitations

**3.1.3.1 Experimental Error** In addition to the destructive nature of this test and the time involved in its measurements, its major disadvantage is its hypersensitivity to experimental errors (26). A simple propagation of error analysis may be used to show the best possible errors that can occur in a manual interrupted tensile test where the indirect formula is commonly used. Using this equation:

$$(3.5) \quad r = -\frac{\epsilon_w}{\epsilon_l + \epsilon_w}$$

and assuming that there is no error in reading the initial dimensions,  $w_0$  and  $l_0$ , one has the following expression for the uncertainty in  $r$ :

$$(3.6) \quad u_r = \left[\frac{r+1}{\epsilon_l}\right] \left[r \frac{u_l}{l} + (r+1) \frac{u_w}{w}\right]$$

where  $\epsilon_l$  is the axial strain and  $u_l$  and  $u_w$  are the uncertainties in final length and width measurements. It is evident that, in addition to errors in the final measurements of length and width, the error in  $r$  is also a function of the level of elongation and  $r$  itself. The error is, therefore, larger at 20% elongation than at 15%, and similarly it is larger for larger values of  $r$  ( $>2$ ). Figure 3.7 shows the plot of Eqn. 3.6 versus  $r$ . Here, a typical gage length of 2 in. (50 mm) and a gage width of 0.75 in. (20 mm) is selected with the maximum elongation being 20%. The effect of varying errors of 0.0003-0.001 in. (0.007-0.025 mm) in final width measurements is shown with solid lines where the error in length is taken to be 0.001 in. (0.025

mm) as used by Atkinson (26). These errors are essentially the accuracy of the common reading devices which are used, such as traveling microscopes or precision micrometers. The broken line pertains to the ASTM suggested maximum error of 0.002 in. (0.05 mm) in length measurements and 0.0005 in. (0.01 mm) in width measurements. These calculations predict errors of the order of  $\pm 0.03$  to  $\pm 0.07$  for an  $r$ -value of 2. Also if one takes into account the error in the measurements of initial length and width, and assumes that they are the same as the error in the final width and length measurements, the best possible error actually doubles, with the range being  $\pm 0.06$  to  $\pm 0.14$  for  $r$  at 2 and 20% elongation. In fact as shown by a similar analysis presented in section E517-8 of the ASTM standard, the error in  $r$  is very sensitive to accuracy of the initial width measurement (67). Also not every material can be tested at 20% elongation, so a best possible experimental error range of  $\pm 0.2$  when  $r$  equals 2 is quite realistic.

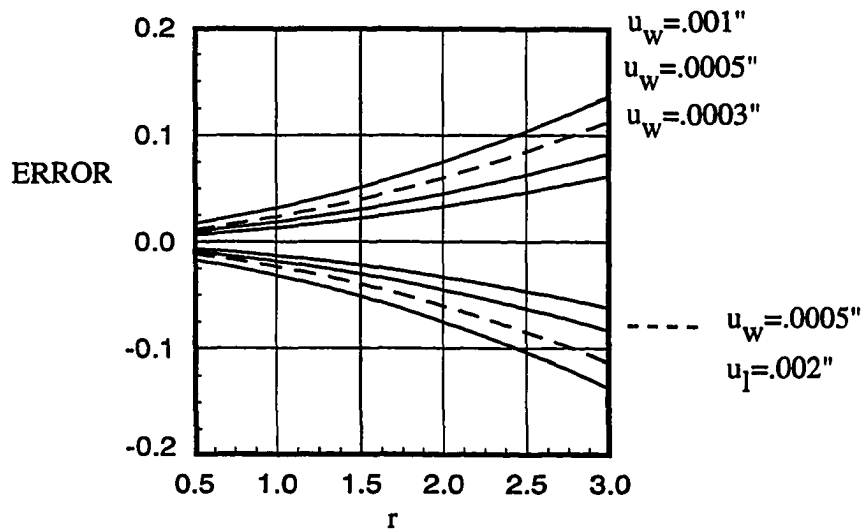


Fig. 3.7 error in  $r$  at 20% elongation

In practice the errors can be very large as shown in Fig. 3.1 where the maximum difference between 13 measurements for a given direction of  $r$  on the same sheet was 0.43. As reported by Duncan et al. (63), for strain ratios of 2, accuracy of  $\pm 0.13$  can not be readily achieved. In fact, Liu (65) has suggested that, due to these limitations of the tensile technique, for  $r$ -values in and above the 2 range, the final result should only include the first digit (i.e. after decimal) while the second digit after decimal has no significance.

To reduce these errors, automatic tensile testing has been introduced as an alternative to manual measurement (64, 69). Here, an extensometer is used to monitor the strains continuously and a regression analysis is performed to obtain an average  $r$ -value over a suitable range, as discussed in Section 3.1.2.4. The automatic regression analysis method certainly is more reliable than the manual method due to the increased number of data points which are employed, (usually 9-12 points), (61, 64 and 65). Also the extensometer used in these tests seems to be more accurate than the common reading devices used in the manual technique. However, as reported by Lake et al. (64, 69) the extensometers may be mismounted or their readings may be affected by nonuniformities of the machined edges of the samples. The comparison between the automatic and manual measurements of  $r$  on the same steel samples in the above work showed a large systematic deviation which could not be accounted for. Initially, they attributed the difference to stress relaxation effects, although their later work did not prove it. It may be postulated that the  $r$ -values are larger in dynamic tests than in quasi-static manual tests. This difference between automatic and manual results should be investigated further.

**3.1.3.2 Suitability of the current definition of  $r$**  There has been some discussion regarding the definition of  $r$  itself as being another disadvantage of the tension test. This point was discussed in Section 3.1.2.4 with respect to differences between regression  $r$  and conventional  $r$ . In general, the regression  $r$  is considered to be closer to the true representation of

---

anisotropy in rolled sheets.

Based on previous findings in the literature, Welch, Ratke and Bunge (66) have suggested another anisotropy parameter,  $\rho(\epsilon)$ , which represents the instantaneous anisotropy of the sheet,  $\rho(\epsilon)=(dw/w)/(dt/t)$ . This parameter is the slope of the tangent to the  $\epsilon_w-\epsilon_t$  or  $\epsilon_w-\epsilon_l$  plots and can be integrated over a desired interval to obtain the integral anisotropy of the sheet. They have shown that the conventional  $r$  and regression  $r$  are in fact approximations to this parameter.

Another parameter which is considered to be even better than regression and conventional  $r$ 's and  $\rho(\epsilon)$ , is the contraction ratio,  $q$ , which was defined previously as  $r/(r+1)$ . This parameter is more well-behaved than the others since it varies between 0 and 1 whereas the others theoretically vary between 0 and infinity. Analysis shows that the error in the contraction ratio,  $q$ , is insensitive to its magnitude.

### **3.2 Magnetostrictive Technique: Modul-r Instrument**

As part of a two year development program at U.S. Steel Corporation, a drawability testing instrument was designed and developed in 1968, which predicts  $\bar{r}$  and  $\Delta r$  through a magnetostrictive technique (30). The main objective behind the development of this instrument was to provide a faster, more reliable and a less operator-dependent technique than the tensile technique in measurement of plastic strain ratio and the earing tendencies of low carbon steel sheets.

#### **3.2.1 The Procedure and the Equipment**

Figure 3.8 shows a photograph of the instrument and the samples. Three parallel sided coupons, approximately 4 in. by 0.25 in. (100 mm by 6 mm) are punched using a special press at 0, 45 and 90 degrees with respect to the rolling direction of the rolled sheet. The

specimens are then inserted into the instrument where their resonant frequencies are measured. Based on the theory of guided wave propagation, the frequency of the sample is related to the Young's modulus by  $E=4dl^2f^2$ , where  $d$  is the density,  $l$  is the length of specimen and  $f$  is the resonant frequency of the sample. By calculating the  $\bar{E}$  and  $\Delta E$  from the directional  $E$ 's, the  $\bar{r}$  and  $\Delta r$ , can be obtained through using Eqns. 1.8 and 1.9 as described in Chapter 1.

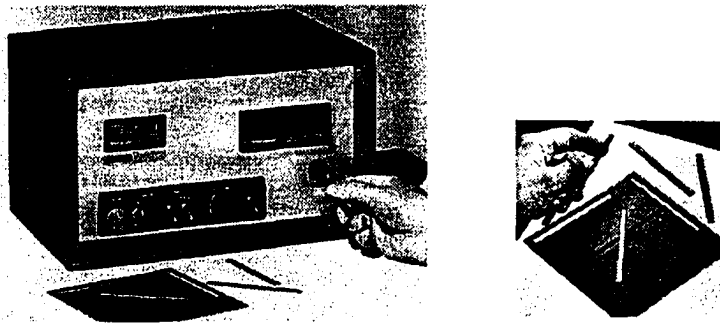


Fig. 3.8 Modul-r instrument

The basic components of the system consist of three axially-aligned encircling coils surrounding the specimen, an amplifier and an electronic counter to measure the resonant frequency of the sample (Fig. 3.9). As the sample is placed in the system, an alternating current in the drive coil produces an alternating magnetic field. In the presence of this field, there are longitudinal vibrations produced in the specimen, due to magnetostriction. These travel with the characteristic speed of sound for the material. These vibrations, appearing as alternating compressive and tensile strains in the other end of specimen, are picked up by the pickup coil. The received signal is then amplified and sent back to the drive coil. Starting from a value below resonance, the frequency of oscillations is increased until the maximum

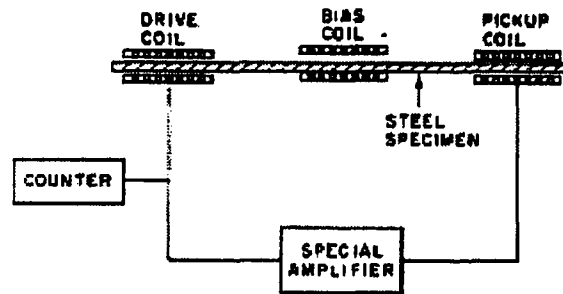


Fig. 3.9 The electronics behind the Modul-r instrument

amplitude is obtained, which is at the resonant frequency of the sample.

### 3.2.2 Limitations

**3.2.2.1 Coating of the samples and surface roughness** Some of the limitations of this technique are caused by its sensitivity to the surface roughness (there is, however, a correction formula to be used by the operator to account for the effects of surface roughness) and the presence of coatings on the steel sheets (30). The effect of surface roughness is to increase the mass with little contribution to the restoring force. Therefore, the resonant frequency decreases with increasing roughness, particularly for thin sheets. The effects of coating are similar, decreasing the frequencies and thus decreasing the apparent Young's modulus. The coatings are, therefore, removed using chemical means which can contribute significantly to the time involved in sample preparation.

**3.2.2.2 Capability in measuring directional  $r$ 's** The main outputs of this instrument do not include the directional  $r$ 's and the capability to measure  $r$ 's at 0, 45 and 90 degrees is not readily available for the user. In addition to Eqns. 1.8 and 1.9, Stickles and Mould (29), in their original work, reported an experimental correlation between directional moduli (i.e.  $E(0)$ ,  $E(45)$ , and  $E(90)$ ) and the anisotropy in the rolling plane,  $r(90)-r(0)$ . However, the correlation coefficient reported was not high enough for reliable directional  $r$  calculations from these correlations. This will be considered further in the following section.

**3.2.2.3. The experimental error** In this technique, sample geometry is simple and sample preparation is simplified by using the recommended punch and press which seems to provide sufficient tolerances, thus reducing the usual uncertainties associated with machining processes. There is the question of the effects of the finite size of the samples on the guided mode wave propagation relation. However, this effect is small (30). The error in measuring the frequency is reported to be 0.07% obtained on 179 samples (30). This leads to an error of approximately 0.14% in measuring Young's modulus which is quite small.

The main error in the calculation of the strain ratio when using this technique is inherent in its experimental correlations (Eqns. 1.8 and 1.9). This error is largely due to the errors of the associated tensile results on 230 steel samples which the authors collected from a variety of laboratories within the U.S. Steel Corporation. The tensile  $r$ 's so obtained were directly used in their statistical analysis in establishing Eqns. 1.8 and 1.9. Although, the correlation coefficients reported for these two equations were significant (0.92 and 0.87), in view of the previous discussions in this chapter, the variability errors and the limitations inherent in tensile testing can lead to a significant scatter in the statistical relations between average  $E$  and  $r$ .

More recently, a study involving 85 low carbon steel sheets including vacuum degassed interstitial free steels has led to correlations very similar to the ones used in the Modul- $r$  in-

strument (60). A similar study involving 179 samples where Young's modulus was measured ultrasonically has resulted in comparable correlations (1). Despite the empirical errors in these correlations, they point to the sound physical foundations that govern the relationship between elastic and plastic anisotropy. These foundations will be described more closely in Chapter 4.

## CHAPTER 4

### ULTRASONIC MEASUREMENT OF DRAWABILITY

#### 4.1 Theory

The basic principle on which the ultrasonic measurement of drawability is based is the sensitivity of the speed of the guided mode ultrasonic waves to the texture of the sheet. The speed of the waves exhibits anisotropy in the plane of the sheet (from the rolling direction to the transverse direction) caused by the anisotropy in the elastic properties such as Young's Modulus which is caused by texture. The anisotropy in the plastic properties, such as  $r$ -values, are also controlled by texture; hence the relationship between the elastic and plastic properties. The ultrasonic waves play the same role that the diffracted X-rays play in construction of the pole figure. The so-obtained experimental information regarding the texture of the sheet may be used to characterize the texture in the framework of a quantitative texture analysis, the ODF technique. As mentioned in Chapter 2, the two basic aspects of such an analysis are the texture characterization (identification of major orientations) and the measurement of the average macroscopic properties of a polycrystal which are texture dependent (i.e.  $r$ -values, Young's modulus). This latter aspect is the topic of the following discussion in this Chapter.

A theoretical formalism for the relation between the speed of the guided mode Lamb waves ( $S_0$ , generated by electromagnetic acoustic transducers, EMATs) and the elastic properties of the textured sheets has been established by Thompson et al. (34, 36, 37). This theory also quantitatively relates the anisotropy of these waves to the texture coefficients,  $C_4^{\mu\nu}$  or  $W_{4mn}$  (in Roe's notation (31)). Coupled with successful development of ultrasonic instrumentation technology, this theory has led to the practical realization of ultrasonic meas-

urements of elastic and plastic properties as demonstrated by the development of the current automatic prototype, Ultra-Form (2), which has been used in the present work which was described in Chapter 1.

Fig. 4.1 shows a block diagram of the sequence of events leading to calculation of  $r$ -values from data generated by Ultra-Form. Calculating the texture coefficients (which were previously described in Chapter 2) from the anisotropy of the ultrasonic waves, two models can be used to obtain  $r$ -values. Both of these models use the properties of a single crystal to calculate the macroscopic elastic and plastic properties of the polycrystalline material. In the first model, the elastic properties of the textured sheet are calculated by averaging the single crystal's elastic properties (elastic constants). This leads to the calculation of Young's modulus of the sheet and its angular variation,  $E(\alpha)$  in the plane of the sheet. By defining an average value for Young's modulus and its anisotropy (similar to Eqns. 1.6 and 1.7),  $\bar{r}$  and  $\Delta r$  can be calculated using the Mould and Johnson correlations, Eqns. 1.8 and 1.9 (30). The second model, which is a plastic deformation model (61), calculates the plastic properties of the single crystal and averages them to obtain the macroscopic  $r$ -values. This also provides the angular variation of  $r$ -values,  $r(\alpha)$  in the plane of the sheet.

This chapter attempts to outline the basic principles of such calculations. The steps shown in Fig. 4.1 have been previously programmed in Ultra-Form in the form of a computer algorithm (Ultra-Form's program includes only Mould and Johnson correlations). This algorithm was written during the instrument's development phase when this author was also involved as a technical member of the team that developed the instrument (2). However, since the time when this author started his Ph.D program, some additional programs have also been written (on DECstations) which are not part of the Ultra-Form original codes. These include codes incorporating the previously mentioned plastic deformation model

which was tested as an alternative to the Mould and Johnson correlations (30), ideal texture simulations and Young' modulus calculations (similar to the one already programmed in Ultra-Form). These codes will also be described in this chapter.

Any attempt to describe the theoretical principles underlying the ultrasonic measurement of rolled sheet properties, necessarily entails discussion of four major topics. The first, is the theory relating the velocity of ultrasonic pulses with the elastic properties of the rolled sheet. The second and third topics comprise the theories that model the elastic and plastic behavior of a single crystal. The fourth and final topic, is a description of the series expansion technique. Since this technique plays a central role in most of the above, its description will precede the others. The theories behind ultrasonic plane wave solutions (in a plate mode) and elastic and plastic behavior of single crystals will be presented later when the description of the series expansion technique is complete.

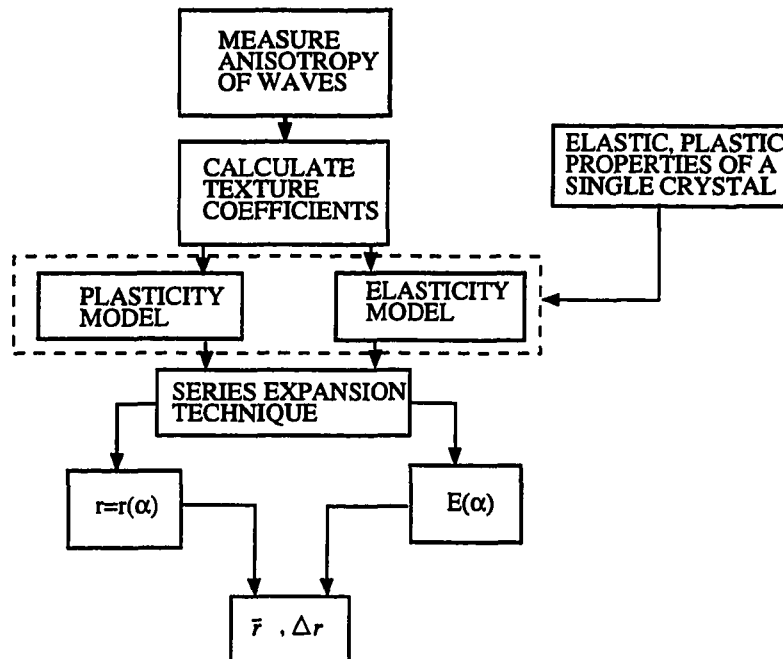


Fig. 4.1 The ultrasonic measurement of r-values

#### 4.1.1 Series Expansion Technique

Since the texture of a polycrystal is defined at a microscopic level, calculation of the macroscopic properties using texture information obtained by ultrasonics or X-rays, involves utilization of a suitable microscopic model that can predict the anisotropic elastic and plastic behavior of a single crystal. Once the single crystal properties are known, then they are averaged using texture as a weight function to arrive at the average properties of the polycrystal:

$$(4.1) \quad \bar{A} = \int A^c(g) f(g) dg$$

where  $g$  (i.e.  $\Psi_1$ ,  $\Phi$  and  $\Psi_2$ ) describes the orientation of the crystal relative to the sample coordinate system,  $f(g)$  is the measured ODF and  $A^c$  is the corresponding property of a single crystal.

The averaging scheme of Eqn. 4.1 generally involves two coordinate transformations. Since  $\bar{A}$  is desired in the sample coordinate system the starting point for calculations is the property of the single crystal with respect to the crystallite coordinate system. The first transformation is then a rotation from the crystallite coordinate system into that of the polycrystal (Fig. 4.2b). Here, the property of interest is averaged over all possible orientations of the crystallite (represented by a group of rotations,  $g$ , in Euler space). The second transformation, is a rotation from the sample coordinate system to some 1-2-3 external coordinate system (represented by  $g_0(\alpha, \beta, \gamma)$  which describes the orientation of the sample coordinate system relative to that of the external coordinate system). This 1-2-3 coordinate system might be chosen to be aligned with any imposed external field acting on the sample (strain field,

magnetic field, propagation field of ultrasonic waves, etc.). The axes of the external coordinate system may or may not be coincident with the axes of the sample, as shown in Fig. 4.2. For example, the principle axes of a strain field (represented by the strain tensor) may be coincident with the axes of the sample (i.e. orthorhombic symmetry). However, it is often of interest to evaluate the property of interest in directions which may not be coincident with the axes of the sheet (e.g. in the calculation of Young's modulus or  $r$ -values at an angle  $\alpha$  with respect to the rolling direction). A complete general discussion of this matter can be found by Bunge in reference (32).

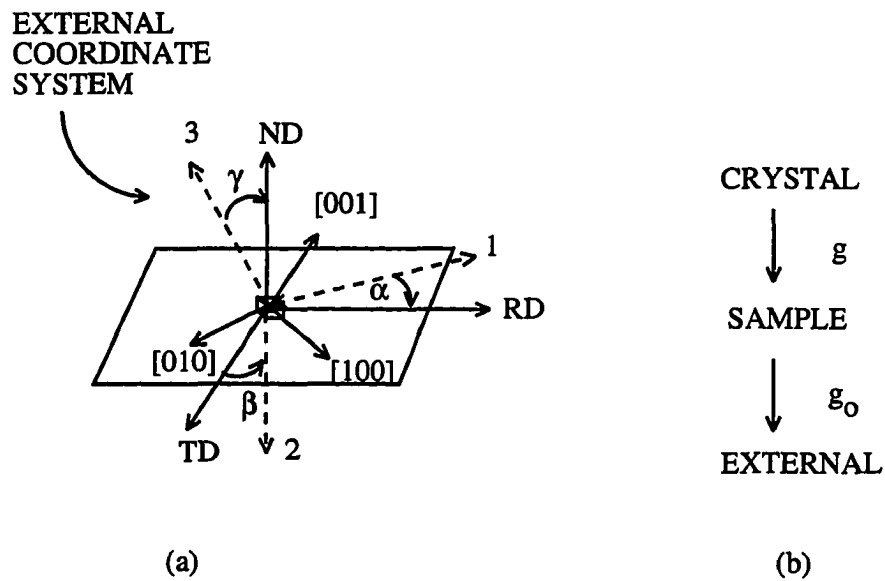


Fig. 4.2 Coordinate transformations in series expansion technique:  
 (a) External coordinate system in relation to those of sample's and crystal's  
 (b) Transformations

Most of the directional properties of rolled sheets and single crystals can be expressed in terms of tensors (e.g. elastic compliance tensor). At the microscopic level, these properties are purely dependent on the orientation of the crystal. Moreover, they follow the symmetries of the crystal structure (i.e. cubic, hexagonal). Integration of Eqn. 4.1 can readily be performed if the functional form of  $A^c(g)$  (i.e. as a function of the crystal orientation) is known. However, in the absence of any exact analytical solution,  $A^c(g)$  can be approximated reasonably well using numerical methods such as the series expansion technique.

The latter uses a statistical fitting procedure (usually a least square technique) to fit the numerically known  $A^c$  (obtained from a suitable microscopic model) to a weighted sum of generalized spherical harmonics with orthorhombic symmetry,  $T_\lambda^{\mu\nu}(g)$  as described in Chapter 2. The harmonic functions, which are linearly independent, are functions of the orientation of the crystals,  $g$ , and have been tabulated in various sources including reference (32). These functions can be readily accessed and used in computer programs.

Using the series expansion technique, the first step in carrying out Eqn. 4.1 is to express the properties of the single crystal in terms of harmonic functions, which are invariant with respect to the sample and crystal symmetries:

$$(4.2) \quad A^c(g) = \sum_{\lambda=0}^L \sum_{\mu=1}^{M(\lambda)} \sum_{\nu=1}^{N(\lambda)} a_\lambda^{\mu\nu} T_\lambda^{\mu\nu}(g)$$

here,  $a_\lambda^{\mu\nu}$  are the coefficients of expansion for the particular property of interest and are obtained using the least square method. The rotation  $g$  includes all the orientations of a sin-

gle crystal relative to the sample coordinate system, Fig. 4.1. Implicit in the steps taken to develop this equation is a tensor transformation from the crystallite coordinate system into that of the sample coordinate system. As shown by Bunge (32),  $L$  is dependent on the rank of the tensor which represents the property of interest (e.g. elastic compliance tensor is of rank 4, and thus, the series can be truncated at  $L=4$ ).

As mentioned before, the average textured macroscopic property,  $\bar{A}$ , is also a function of the second rotation as represented by  $g_o$ , which for orientations in the plane of the sheet can be represented by  $g_o(\alpha, 0, 0)$ . By taking into account this external rotation, and substituting Equations 2.3 and 4.2 in Eqn. 4.1 and performing the integration using orthogonality relations, the following relation is obtained:

$$(4.3) \quad \bar{A}(\alpha) = \sum_{\lambda=0}^L \sum_{\mu=1}^{M(\lambda)} \sum_{\nu=1}^{N(\lambda)} \frac{a_{\lambda}^{\mu\nu} C_{\lambda}^{\mu\nu}}{1+2\lambda} \cos(2\nu - 1)\alpha$$

or in Roe's notation (31):

$$(4.4) \quad \bar{A}(\alpha) = 4\pi^2 \sum_{l=0}^{\infty} \sum_{m=-l}^l \sum_{n=-l}^l A_{lmn} W_{lmn} \cos(m\alpha)$$

These two equations (which are equivalent) relate the average properties of a textured polycrystal to the properties of a single crystal through the coefficients of expansion,  $a_{\lambda}^{\mu\nu}$ , or  $A_{lmn}$  in Roe's notation (31), and the texture coefficients,  $C_{\lambda}^{\mu\nu}$  or  $W_{lmn}$  (in Roe's notation (31)). Both coefficients are obtained numerically through fitting procedures. The former is obtained by fitting the harmonic functions to the numerically calculated properties, and the latter is obtained by fitting harmonics to the experimental pole densities as described in Chapter 2. The texture coefficients are the most comprehensive representation of the crystallographic texture and their experimental measurement plays a central role in carrying the texture information into the analysis.

The number of terms needed ( $L$  or  $l$  in Eqn. 4.3 and 4.4) for convergence of the series expansion is an important consideration in an accurate approximation of the property of interest using texture data. The series expansion of the texture data (Eqn. 2.3) as obtained from X-ray diffraction measurements, is usually truncated at  $L=22$ , since the magnitudes of the texture coefficients decrease rapidly after  $L=10$  and become insignificant after  $L=22$ . However, in some instances, the series expansion of properties (Eqns. 4.3 or 4.4) can be truncated earlier depending on the type of property being considered. For example as mentioned previously, the series expansion of the elastic properties can be truncated at  $L=4$  since  $L$  is dependent on the rank of the tensor representing that particular property and for the elastic compliance or stiffness case, this tensor has a rank of 4 (32, 33). Therefore, only 3 experimental texture coefficients (in addition to the isotropic term,  $L=0$ ) are needed in order to describe the symmetries of these properties completely for cubic crystallites ( $C_4^{11}$ ,  $C_4^{12}$  and  $C_4^{13}$  or  $W_{400}$ ,  $W_{420}$  and  $W_{440}$  in Roe's notation (31)).

The truncation of the series expansion of plastic properties for cubic crystals is believed to follow the same trend. However, as mentioned in Chapter 2, some researchers (61) have argued against the early truncation ( $L=4$ ) in these cases (e.g.  $r$ -values).

#### 4.1.2. Calculation of Elastic Properties

To calculate the elastic properties of a textured sheet from the single crystal properties, two basic pieces of information are needed. One is the set of numerical values of the elastic stiffnesses,  $c_{ijkl}$ , (or elastic compliances,  $s_{ijkl}$ ) of the single crystal, the other being a model that will describe the average response of an aggregate of grains in an elastic regime. The numerical values of elastic constants for single crystals of  $\alpha$ -iron have been measured by a number of researchers and are available in the literature (70). There are three grain averaging models available that approximate the behavior of a polycrystal in an elastically deformed state: the Reuss, Voigt and Hill models. Of these three models, which are all only approximations to the elastic interaction of grains in a polycrystal, Hill's approach (71) has shown to give results which are in closer agreement with the experimental data and for this reason, it was chosen for use in this research.

At the microscopic level, the elastic properties (elastic modulus, shear modulus, Poisson's ratio etc.) are directly related to the elastic constants (or compliances). The elastic constant (compliance) tensor is a fourth rank tensor which has 81 constants when used in the most generalized form of Hooke's law:

$$(4.5) \quad \begin{aligned} \sigma_{ij} &= c_{ijkl} \epsilon_{kl} \\ \epsilon_{ij} &= s_{ijkl} \sigma_{kl} \end{aligned}$$

Here,  $\sigma_{ij}$  and  $\epsilon_{ij}$  are the stress and strain tensors, respectively. Due to various symmetries present (symmetry in stress and strain tensors and the symmetry due to elastic energy con-

siderations ), the elastic constants (compliances) obey the following relations:

$$(4.6) \quad \begin{aligned} c_{ijkl} &= c_{jikl} = c_{klij} = c_{ijlk} \\ s_{ijkl} &= s_{jikl} = s_{klij} = s_{ijlk} \end{aligned}$$

Taking advantage of these symmetries (which reduce the number of independent constants to 21), it is then possible to represent the elastic constant (compliance) tensor in the reduced notation or matrix notation,  $c_{ij}$ ; ( $s_{ij}$ ). In the case of rolled sheets, orthorombic sample symmetry lead to only 9 non-zero independent constants. For isotropic sheets, only two are independent,  $c_{11}$  and  $c_{12}$  ( $s_{11}$  and  $s_{12}$ ). This greatly simplifies the calculations of the macroscopic elastic constants (compliances) of the polycrystal.

To compute the average elastic properties of the textured polycrystal, the series expansion formalism, described in the previous section, can be readily used (Eqns. 4.1 and 4.2). As mentioned previously, a tensor transformation from the crystallite coordinate system to the sample coordinate system takes place (Fig. 4.2b):

$$(4.7) \quad \begin{aligned} s'_{ijkl} &= a_{im}a_{jn}a_{ko}a_{lp}s_{mnop} \\ c'_{ijkl} &= a_{im}a_{jn}a_{ko}a_{lp}c_{mnop} \end{aligned}$$

Here, the  $a_{ij}$  terms pertain to the directional cosines between the two coordinate systems and the primed quantities pertain to the elastic constants or compliances in the sample coordinate

system.

The choice of a polycrystal averaging model can be made here in order to carry out the averaging computations. In the Voigt model, the strain is assumed to be constant for all grains in the aggregate and the elastic constants of the single crystal,  $c_{ij}^V$  are averaged for all orientations of a crystal. In the Reuss approximation the stress is assumed to be the same for all grains in the aggregate and the elastic compliances of the single crystal are averaged,  $s_{ij}^R$ . Hill's approach (71) is the arithmetic mean of the other two:

$$(4.8) \quad s_{ij}^H = \frac{s_{ij}^R + s_{ij}^V}{2}$$

where,

$$(4.9) \quad s_{ij}^V = (c_{ij}^V)^{-1}$$

By applying the series expansion technique (Eqns. 4.1 and 4.2), and incorporating the above transformation, Eqn. 4.7, Bunge (32) has expressed the elastic stiffnesses and compliances of rolled sheet in terms of both models:

$$(4.10) \quad s_{ij}^R = s_{ij}^0 + s^r(a_0 + a_4^{11}(ij)C_4^{11} + a_4^{12}(ij)C_4^{12} + a_4^{13}(ij)C_4^{13})$$

and

$$(4.11) \quad c_{ij}^V = c_{ij}^0 + c^V(a_0 + a_4^{11}(ij)C_4^{11} + a_4^{12}(ij)C_4^{12} + a_4^{13}(ij)C_4^{13})$$

Here,  $c_{ij}^0$  and  $s_{ij}^0$  ( $ij=11, 12, 44$ ) are the elastic constants and compliances of a single cubic crystal, and  $a_4^{\mu V}(ij)$  are the coefficients of expansion as defined in Eqn. 4.2. The  $c_{ij}^V$  and  $s_{ij}^r$  terms relate to the elastic compliances of the polycrystal ( $ij=11, 12, 22, 33, 23, 31, 44, 55$  and  $66$ ).  $c^V$  and  $s^r$  are the Voigt and Reuss single crystal anisotropy parameters defined by the relations:

$$(4.12) \quad \begin{aligned} c^V &= c_{11} - c_{12} - 2c_{44} \\ s^r &= s_{11} - s_{12} - \frac{s_{44}}{2} \end{aligned}$$

Similar expressions for the textured polycrystal's elastic constants have been reported by Sayers (73) and Hirao (74). The use of Hill's approach involves carrying out computations according to Eqns. 4.10 and 4.11 in terms of both Reuss and Voigt techniques, performing a simple matrix inversion of the Voigt elastic stiffnesses (Eqn. 4.9) to elastic compliances and taking an arithmetic mean of the two. As mentioned previously, Eqns. 4.10 and 4.11 reveal that only three experimental texture coefficients are needed to calculate the elastic properties of a rolled sheet. This implies that a variety of textures with approximately the same  $C_4^{\mu V}$  can give rise to the same elastic properties in the textured rolled sheet. As a result, there is a high degree of freedom in choosing textures that form elastic properties. Therefore, a reverse analysis (determining texture from elastic measurements) will not be very complete in terms

of identifying the detailed texture of sheets.

Once the average textured elastic compliances are calculated, the angular variation of the polycrystal's modulus,  $E(\alpha)$ , in the plane of the sheet can be obtained from the following equation which arises from a tensor rotation:

$$(4.13) \quad E(\alpha) = s_{11} \cos^4(\alpha) + s_{22} \sin^4(\alpha) + \sin^2(\alpha) \cos^2(\alpha)(2s_{12} + s_{66})$$

where,  $s_{ij}$  are the elastic compliances of the textured polycrystal calculated according to Hill's approach, and  $\alpha$  is the angle with respect to the rolling direction, Fig. 4.2b. Having measured texture coefficients ultrasonically and calculated the compliances, this equation can readily be used to determine the variation of Young's modulus in the plane of the sheet. Some of the ultrasonic measurements of the moduli of a variety of steel samples which were used in this work are shown in Chapter 5.

#### 4.1.3. Speed of Ultrasonic Waves and Texture

When a force is suddenly applied to an object, the small deformations produced by the force propagate through the body of the object in the form of elastic waves. The types of elastic waves produced depend on the nature of the forces applied. In an unbounded medium, they may be longitudinal (dilatational) waves where the particles are displaced in the direction of the wave propagation or shear (distortional) waves where the particles are displaced in a direction perpendicular to the direction of propagation. At surfaces, a combination of the two, known as Rayleigh waves is observed. The practical use of ultrasonic waves

for measurements on rolled sheets involves guided mode propagation. For thin sheets or plates with two parallel surfaces as boundary conditions, longitudinal waves are modified by the surfaces of the plate and become the low frequency  $S_0$  waves (the fundamental symmetric Lamb mode). Shear waves polarized in the plane of the plate become the  $SH_0$  waves (the fundamental horizontally polarized shear mode). Figure 4.3 presents dispersion curves (plots of frequency vs wavevector) for these two types of waves, as well as illustrating the nature of the mode profiles.

The texture-induced anisotropy in the speed of these waves (generated by EMAT's) on rolled copper and aluminum alloys was measured by Thompson et al. (37). The angular dependence of these waves is shown schematically in Fig. 4.4 by solid lines (34, 37). The dots indicate the points at which experimental measurements are required in order to estimate the degree of anisotropy and the texture of the sheet. It is evident that  $S_0$  modes show a 2-fold symmetry around the rolling and transverse axis every 180 degrees. In addition, the values are equal at 45, 135, 225 and 315°. The  $SH_0$  modes have a 4-fold symmetry.

The theory which describes this 2-fold and 4-fold symmetry of  $S_0$  and  $SH_0$  waves was formulated on the basis of the general solution to the plane wave propagation problem in an unbounded medium (plane strain) (34). It was then modified to describe the guided mode propagation where the effects of the surfaces of a thin plate on the propagation of plane waves is included (plane stress), (36). For textured sheets, this theory leads to a quantification of the texture-induced anisotropy of the waves in terms of the texture coefficients in Roe's notation,  $W_{4mn}$  (31).

The velocity of elastic waves in rolled sheets is directly related to the 9 averaged polycrystalline elastic constants (i.e. Eqn. 4.11, where it gives those constants in the Voigt approximation). By allowing the external coordinate system, 1-2-3 in Fig. 4.2a, to be coincident with the axis of the rolled sheet, the plane stress model may be used for the case where

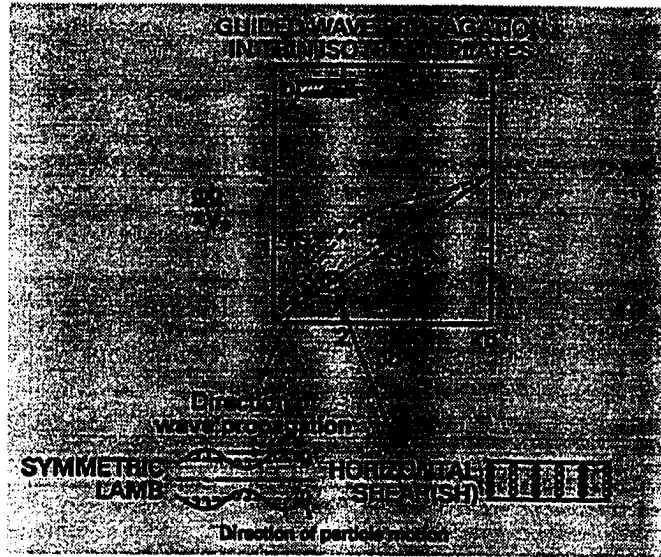


Fig. 4.3 Dispersion of ultrasonic waves (37)

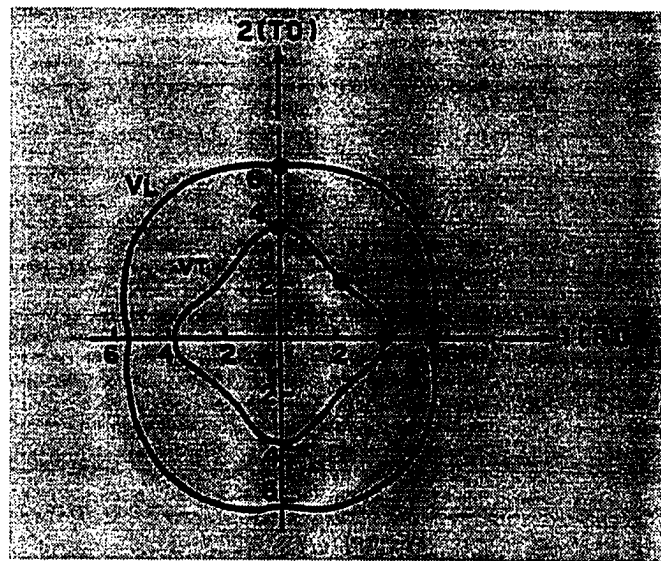


Fig. 4.4 Angular dependence of ultrasonic waves (37)

the stress in the surface of the plate is negligible. Also assuming that the wavelength of the wave is much larger than the thickness of the plate, this stress is negligible throughout the plate, and thus  $\sigma_{i3}=0$ . Taking advantage of these assumptions and using Hook's law (Eqn. 4.5), then,  $\epsilon_{23}=\epsilon_{13}=0$  and  $\epsilon_{33}=(c_{13}\epsilon_{11}+c_{23}\epsilon_{22})$ , and the resulting equations of motion will be the following (36):

$$(4.14) \quad \begin{aligned} \rho \frac{\partial^2 u_1}{\partial t^2} &= \frac{\partial}{\partial x_1} [\tilde{c}_{11} \frac{\partial u_1}{\partial x_1} + \tilde{c}_{12} \frac{\partial u_2}{\partial x_2}] + c_{66} \frac{\partial}{\partial x_2} [\frac{\partial u_2}{\partial x_1} + \frac{\partial u_1}{\partial x_2}] \\ \rho \frac{\partial^2 u_2}{\partial t^2} &= c_{66} \frac{\partial}{\partial x_1} [\frac{\partial u_2}{\partial x_1} + \frac{\partial u_1}{\partial x_2}] + \frac{\partial}{\partial x_2} [\tilde{c}_{12} \frac{\partial u_1}{\partial x_1} + \tilde{c}_{22} \frac{\partial u_2}{\partial x_2}] \end{aligned}$$

where,

$$(4.15) \quad \begin{aligned} \tilde{c}_{11} &= c_{11} - \frac{c_{13}^2}{c_{33}} \\ \tilde{c}_{12} &= c_{12} - \frac{c_{13}c_{23}}{c_{33}} \\ \tilde{c}_{22} &= c_{22} - \frac{c_{23}^2}{c_{33}} \end{aligned}$$

Here the  $\tilde{c}$  terms are the 'effective' elastic constants of the polycrystalline and the  $c_{ij}$  terms are the average polycrystal elastic constants as calculated from Eqn. 4.11.

The functional form of the angular dependence of plane wave solutions at any angle with respect to rolling direction,  $\alpha$  (Fig. 4.2a), is obtained from the Christofel equation as reported in reference (73). In general, its form is as follows:

$$(4.16) \quad \det(\Gamma_{ij} - \rho V^2 \delta_{ij})$$

In this equation, the  $\Gamma_{ij}$  depend on the elastic constants of the polycrystal, modified by the directional cosines involved in transformation to the new coordinate system, and  $V$  is the speed of wave propagation.  $\delta_{ij}$  is the Kronecker delta and  $\rho$  is the density of the material. When the elastic constants are replaced by other 'effective values', the angular dependence of guided wave propagation in the plane of the plate is obtained.

Expanding this effective solution of Eqn. 4.16, one will have the following solution for the low frequency  $S_0$  and  $SH_0$  plate mode waves:

$$(4.17) \quad \begin{aligned} V_{S_0} &= \sqrt{\frac{\hat{C}_L}{\rho}} \left[ 1 + \frac{\hat{\alpha}}{4} \cos(2\alpha) - \frac{\hat{\beta} \hat{C}_T}{4 \hat{C}_L} (1 - 2 \cos(4\alpha) + \dots) \right] \\ V_{SH_0} &= \sqrt{\frac{\hat{C}_T}{\rho}} \left[ 1 + \frac{\hat{\beta}}{4} (1 - \cos(4\alpha) + \dots) \right] \end{aligned}$$

where,

$$(4.18) \quad \begin{aligned} \hat{C}_L &= \frac{c_{11} + c_{22}}{2} - \frac{c_{13}^2 + c_{23}^2}{2c_{33}} \\ \hat{C}_T &= c_{66} \end{aligned}$$

In these equations,  $\hat{\alpha}$  and  $\hat{\beta}$  are the anisotropies of the waves, which have been expressed in terms of the elastic constants of the polycrystal and are given in reference (34).

The combination of expressions for the textured polycrystal's elastic constants (Eqn. 4.11) and the solution to the wave equations (Eqn. 4.17) leads to the link between the anisotropies of the guided mode plate ultrasonic waves and the texture coefficients in Roe's notation (36, 37). For the low frequency  $S_0$  plate waves, the link is the following:

$$(4.19) \quad W_{400} = \frac{35\sqrt{2}\rho}{32\pi^2[3+8(P/L)+8(P/L)^2]c} [V_{S_0}^2(0^\circ) + V_{S_0}^2(90^\circ) + 2V_{S_0}^2(45^\circ) - 4V_{isot}]$$

$$W_{420} = \frac{7\sqrt{5}\rho}{32\pi^2(1+2P/L)c} [V_{S_0}^2(90^\circ) - V_{S_0}^2(0^\circ)]$$

$$W_{440} = \frac{\sqrt{35}\rho}{32\pi^2c} [V_{S_0}^2(0^\circ) + V_{S_0}^2(90^\circ) - 2V_{S_0}^2(45^\circ)]$$

where  $V_{isot}$  is the isotropic longitudinal wave speed in the absence of texture:

$$(4.20) \quad V_{isot} = \sqrt{\frac{L^2 - P^2}{\rho L}}$$

Also, P and L are  $(c_{11}-2c_{44})$  and  $(c_{11}-2c/5)$ , respectively. These are equal to  $\lambda$  and  $\lambda+2\mu$  in the Voigt approximation where  $\lambda$  and  $\mu$  are the Lamé' elastic constants.  $c$  is the single crystal elastic anisotropy parameter as defined in Eqn. 4.12. Similar expressions have been obtained for relations between the speed of  $SH_0$  waves and the texture coefficients. However, they are omitted here, since  $SH_0$  waves were not used in this work.

Equations 4.19 are the key quantitative relations which make the ultrasonic measurement of  $r$ -values of rolled sheets possible. As can be seen from these equations, the texture coefficients calculated ultrasonically, are functions of the anisotropy of the waves and the elastic properties of the single crystal. The latter play an important role in the overall calculations of macroscopic properties and also in the propagation of error considerations. These will be described in Chapter 5. The interesting feature of these relations is the use of the 0, 45 and 90 degree velocities to calculate the texture coefficients. This is consistent with the traditional use of properties ( $E$  or  $r$ -values) in these directions to calculate the weighted means (i.e.  $\bar{r}$ ). One reason is that these directions represent the so-called axes of maximum and minimum ductility in rolled sheets (caused by the texture) where the properties vary the most. Similar to these trends in properties, the magnitude of the speed of the ultrasonic waves shows the largest change in these axis as well (i.e. the speed of  $S_0$  Lamb waves is the highest in 45 degree direction) (37).

Since the speed of the  $S_0$  waves are generally frequency dependent, their speed at the low frequency limit should be used in all the calculations. This requires a correction scheme to be applied to the experimental values of the velocities at the time when they are measured by Ultra-Form. This correction which is part of the overall codes of the instrument will be described in Chapter 5. It should be mentioned that the averaging technique employed in calculation of the isotropic polycrystal properties in Eqn. 4.19 is based on Hill's approach as described in the previous section.

#### 4.1.4 Calculation of Plastic Properties

The models for predicting the plastic deformation of metals fall into two major categories. One involves computations of average properties at the macroscopic level and the other involves computations at the microscopic level based on the behavior of a single crystal. Examples of the first type include obtaining the yield surface of a particular sample experimentally and then deriving the properties analytically according to one of the known yield criteria. The results have been incorporated in various finite element solutions of formability problems available in commercial packages (see Chapter 1 ).

The second type model evaluates the plastic properties of single crystals based on the established crystallographic yield criterion of Schmid (Schmid law). Similar to calculation of elastic properties, an appropriate grain interaction model is then employed to obtain the average polycrystal's properties and its yield surface. However, the mechanisms of grain interaction in the plastic regime is more complicated than in the elastic regime. This is due to complexities associated with the interaction of grain boundaries in the polycrystalline, and the slip process which is now universally believed to be the main mechanism involved in the plastic deformation of metals.

When a macroscopic stress, represented by the stress tensor,  $\sigma_{ij}$ , is applied to a body, it gives rise to internal crystallographic shear stresses,  $\tau_s$ . When the stress reaches a certain critical value,  $\tau_s^c$ , plastic flow occurs in the single crystal. This flow is in the form of slip, which is the movement of lamellae of the crystal sliding over one another, (similar to movement of a number of stacked cards when the deck is distorted). This displacement takes place most easily along a certain crystallographic plane (slip plane) and in a particular crystallographic direction (slip direction) which together constitute a slip system. There may be several slip systems active simultaneously ( $s=1-n$  where  $n$  is the number of active slip systems).

The critical shear stress,  $\tau_s^c$ , is always compared to the applied stress resolved on the slip planes in the direction of slip, and thus is called the critically resolved shear stress, CRSS (Fig. 4.5). According to the Schmid law, of the many slip systems available, the ones whose resolved shear stress has reached the critical level will become active, thus the resolved shear stresses must always satisfy the relationship (75):

$$(4.21) \quad \tau_s \leq \tau_s^c$$

By a simple resolution of forces on the slip plane (Fig. 4.5),  $\tau_s$  is equal to:

$$(4.22) \quad \tau_s = \sigma_{ij} [\cos(\lambda_1)\cos(\lambda_2)]_s = m_s(hkl) \sigma_{ij}$$

where  $m_s(hkl)$  and  $\tau_s$  are the Schmid factor and the shear stress on the  $s^{\text{th}}$  slip system respectively. The Schmid factor is purely dependent on the orientation of the crystal as shown in Fig. 4.5.

The CRSS is always the same for the crystallographically equivalent planes, whereas it may not be the same otherwise. It differs from metal to metal and is a function of degree of purity, temperature and prior strain or deformation (75).

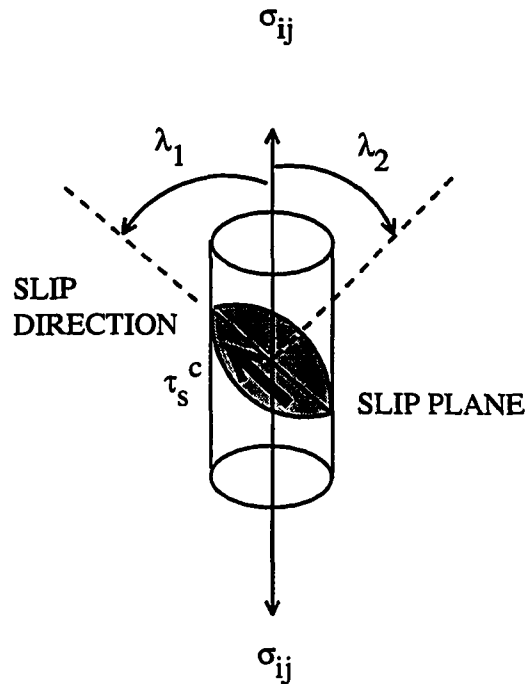


Fig. 4.5 Critically resolved shear stress in a single crystal

**4.1.4.1 Character of slip in bcc Crystals** In bcc crystals (and fcc crystals), the slip planes are always the planes of the most densely packed atoms and the slip direction is always the close-packed direction. In fcc crystals these are the  $\{111\}$  planes with the slip direction in the  $[110]$  direction, which together constitute 12 slip systems. In bcc crystals, the situation is more complicated, since several slip planes ( $\{110\}$ ,  $\{112\}$  and  $\{123\}$ ) may be active simultaneously at room temperature. However, the slip direction is always  $[111]$ . This leads to a maximum possible number of 48 slip systems. Slip can be visually recognized by the presence of slip lines formed by the intersection of slip planes with the surface of the crystal. Slip lines are straight when a single set of slip planes are activated, and it is wavy when mixed slip has occurred. Figure 4.6 shows a micrograph of slip lines on decarburized

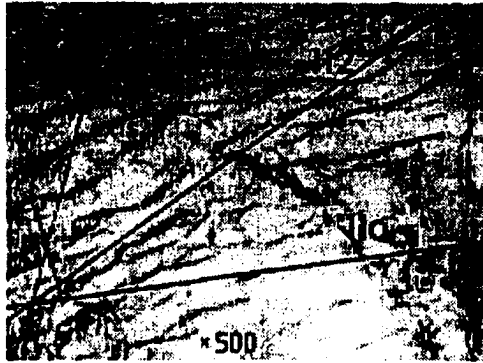


Fig. 4.6 Mixed slip mode in decarburized crystals of iron (76)

single crystals of iron at room temperature where the wavy lines indicate a mixed {110}-{112} glide systems in these crystals (76). The mode of slip in bcc crystals of iron has not been completely elucidated, however.

As stated earlier, mixed slip is generally considered to occur on {110}, {112} and {123} planes. In order to describe the degree of competition in mixed slip between these planes, the ratio of the CRSS for {112} and {123} planes relative to the {110} planes has been experimentally measured and theoretically calculated by several investigators (76, 77 and as reported in 75 and 61). Table 4.1 shows the variously reported values of these ratios:

$$(4.23) \quad \begin{aligned} CR_1 &= \frac{CRSS_{112}}{CRSS_{110}} \\ CR_2 &= \frac{CRSS_{123}}{CRSS_{110}} \end{aligned}$$

Chin (77) used a theoretical model to predict the consequences of various values of  $CR_1$  and  $CR_2$  in a mixed slip mode in bcc crystals of iron. He has shown that if  $CR_1$  is larger than 1.15, then the slip occurs solely on {110} planes whereas if it is less than 0.86, the slip is solely on {112} planes. Franciosi (76) has conducted extensive experimental tests and his results center on the conclusion that a mixed slip only on {112} and {110} planes takes place for pure iron (Fig. 4.6).

Table 4.1 Experimental and theoretical  $CR_1$  and  $CR_2$  values for crystals of iron

Investigator	$CR_1$	$CR_2$
(61)	0.93 <sup>a</sup>	
(75)	1.07 <sup>a</sup>	1.07-1.11 <sup>a</sup> (at 190 <sup>o</sup> c)
(76)	1.0	
(77)	0.86-1.15	.94-1.13

a: Fe-3%wt-Si

**4.1.4.2 Grain Interaction Models and Calculation of  $r$ -values** When a single crystal is deformed plastically, it is free to deform on a single or multiple set of slip planes and it can arbitrarily change its shape. But when imbedded in an aggregate, the variously oriented neighboring grains impose constraints on all of its sides and it can not change its shape in an arbitrary manner. The major task in modeling the behavior of crystals in an aggregate is the description of the effect of these constraints on the plastic flow of the imbedded crystal.

As for the elastic case, there are several models available that describe the interaction of grains in a plastically deformed polycrystal. Among these, the full constraint theory devised by Taylor (41) has received the most attention. However, the shortcomings associated with this theory have led a number of investigators to develop alternatives, which are called re-

laxed constraint models, herein called RC (For a review see works of Honneff, Mecking, Kocks, Canova and Van Houtte as indexed in reference (60)). These relaxed constraint models which are all modifications of the full constraint theory, were originally designed to model deformation textures observed in commercially rolled sheets. They are particularly suited for sheets which are characterized by a flat ('pancake') grain structure. Daniel and Jonas (61) have used these models to simulate the plastic deformation of deep drawing grade steel sheets in a uniaxial tensile test, and have successfully predicted r-values. Since this approach seemed to provide advantages over the full constraint theory, it was decided to use it in this work. However, since RC is derived from the Taylor theory, the full constraint theory will be discussed next.

**4.1.4.3 Full Constraint Theory** According to this theory, each grain of the polycrystal undergoes approximately the same strain as the aggregate does (i.e. it tends to elongate in proportion to the elongation of the bulk material and to contract laterally in proportion to the lateral contraction of the aggregate). Such an assumption (known as the *Taylor assumption*) requires that the local strain tensor,  $\epsilon_{ij}^c$  and the macroscopic strain tensor be equal:

$$(4.24) \quad \epsilon_{ij}^c = \epsilon_{ij}$$

In this equation the local crystallite strain tensor has been transformed into the sample coordinate system by a tensor rotation.

In a mechanical test, the elements of the macroscopic strain tensor may not be known, but the strain state (uniaxial, axisymmetric etc.) can often be assumed and considered to be known *a priori*. For instance, in order to simulate the deformation in a tensile test, one can assume a uniaxial tension with the principal axes of strain (1-2-3 in Fig. 4.2a) coincident

with the axes of symmetry of the rolled plate. Then the macroscopic strain tensor will be the following:

$$(4.25) \quad \epsilon_{ij} = \epsilon_{11} \begin{vmatrix} 1 & 0 & 0 \\ 0 & -q & 0 \\ 0 & 0 & -(1-q) \end{vmatrix}$$

where  $q$  is the contraction ratio, defined in Eqn. 3.4 in Chapter 3. The contraction ratio is a measure of the lateral contraction of the volume element (in this case, the tensile specimen) and is related to the plastic strain ratio,  $r$ , by the following equation:

$$(4.26) \quad q = \frac{\epsilon_{22}}{\epsilon_{11}} = \frac{r}{r+1}$$

By assuming different values for  $q$  (from 0 to 1), the right hand side of Eqn. 4.24 will, in effect, be imposed. Therefore Equation 4.25 sets the boundary conditions.

Since the strain tensor has six independent components (i.e.  $ij=11, 12, 13, 23, 22$  and  $33$ ) and only five are independent in a plastic regime, Taylor (41) reasoned that an arbitrary change of shape of this type (i.e. when the constraints are imposed by the macroscopic strain tensor) requires a minimum of five independent slip systems to operate continually. Consequently, the independent combinations of available slip systems ( $s=n$ ) which give rise to the

local strain tensor,  $\epsilon_{ij}^c$ , will have to be identified:

$$(4.27) \quad \epsilon_{ij}^c = \sum_{s=1}^n m(hkl)_s d\gamma_s$$

where  $d\gamma_s$  refers to the crystallographic shear strains on the slip system and  $m(hkl)_s$  are the Schmid factors for the slip system,  $s$ . Equation 4.27 consists of five independent equations with  $n$  unknowns. To identify all the combinations of five independent slip systems is a formidable task. For example, in bcc crystals, assuming a mixed slip mode on {110} and {112} planes, one can have 42504 combinations of five independent systems (each glide plane has 12 slip directions and a total of 24 slip systems). Using the principle of least work, Taylor (41) then postulated that out of all these combinations, only those systems are active which lead to the minimum amount of internal crystallographic work (*Taylor criterion*), defined by the following:

$$(4.28) \quad W = CRSS_s \sum_{s=1}^n d\gamma_s$$

where CRSS is the same for crystallographically equivalent systems. Also, Taylor defined a factor (known as the *Taylor factor*):

$$(4.29) \quad \frac{W}{CRSS_s} = M = \min \sum_{s=1}^n d\gamma_s$$

The principle of least work reduces the task of identifying the independent combinations of slip systems in Eqn. 4.27 to a minimization problem which can be solved using linear programming techniques, (72). These programs are readily available and straightforward to use. The output of such a program yields the minimum crystallographic shears which are then used in Eqn. 4.29 to calculate M.

It should be mentioned that M is a function of the crystal orientation and the state of macroscopic strain, q. The former has been indicated in Eqn. 4.27 by the presence of the Schmid factor, and the latter has been imposed by the boundary conditions. Therefore, M, as calculated in Eqn. 4.29, is obtained at a given orientation of a crystal. The series expansion formalism can be readily used to average M for all orientations and calculate  $\bar{M}$  for the polycrystal as a function of q and the angle with respect to the rolling direction,  $\alpha$ . Applying Eqns. 4.2 and 4.3:

$$(4.30) \quad \bar{M}(q, \alpha) = \sum_{\lambda=0}^L \sum_{\mu=1}^{M(\lambda)N(\lambda)} \sum_{\nu=1}^{m_{\lambda}^{\mu\nu} C_{\lambda}^{\mu\nu}} \frac{1}{1+2\lambda} \cos(2\nu - 1)\alpha$$

In this equation texture coefficients are obtained through ultrasonics ( $\lambda=4$ ) or X-ray diffraction. The coefficients of expansion,  $m_{\lambda}^{\mu\nu}$ , are numerically calculated from the calculated Taylor factors (Eqn. 4.29).

The functional form of the relation between  $\bar{M}$  and q for a textured polycrystal is not known analytically. Using the Von Mises associated flow rule, Hosford and Beckofen (12) have determined this relationship analytically for an isotropic sheet. Their results are shown in Fig. 4.7a. In an isotropic sheet, when  $\bar{M}$  is plotted versus q, the curve is symmetric and it

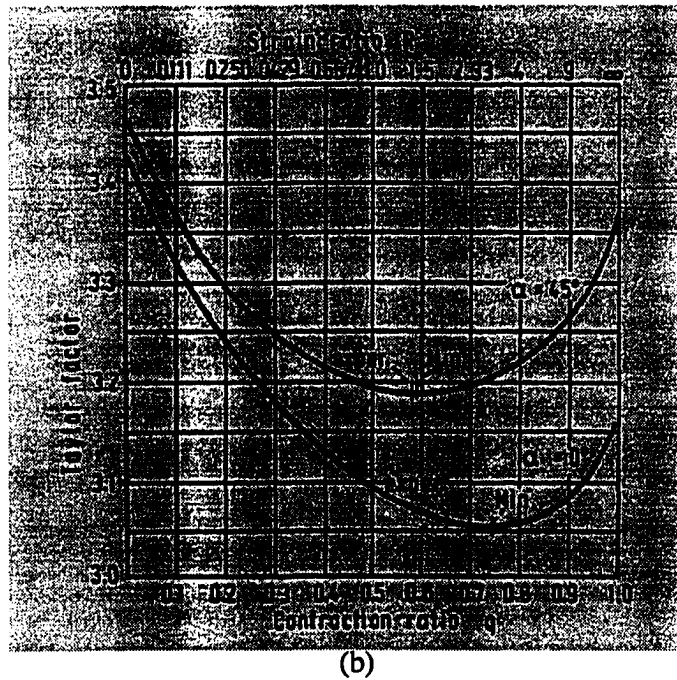
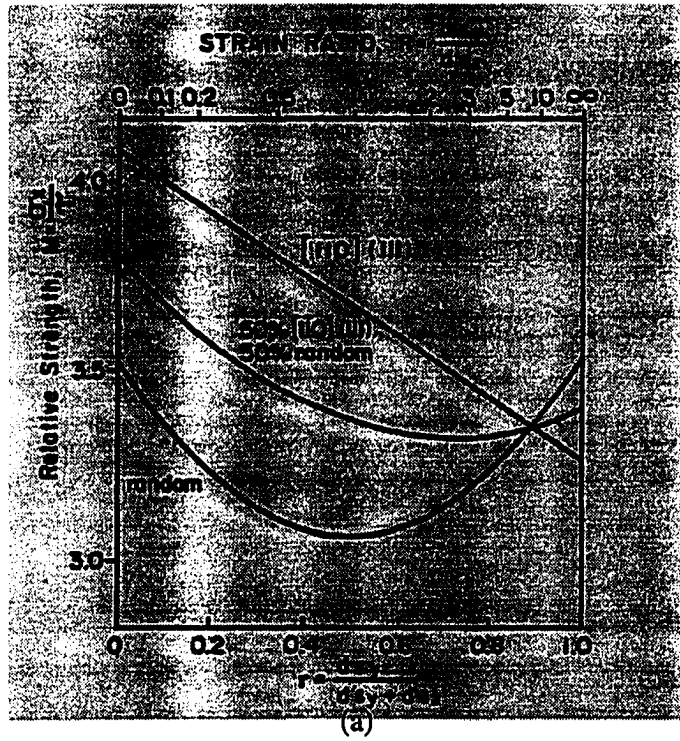


Fig 4.7 Angular dependence of Taylor Factor:  
 (a) Isotropic (12)  
 (b) For an AKDQ steel (32)

shows a minimum at a certain strain state,  $q$ . For a textured sample, the curve is skewed to the left or right depending on the texture components.  $q_{\min}$  is the strain state that gives rise to the minimum shear causing the slip to occur. This is the generalization of the principle of least plastic work in a polycrystal (12). The plastic strain ratio is then calculated using Eqn. 4.26.

Bunge (32) has used the Taylor theory (Eqn. 4.29) and the series expansion method (Eqn. 4.30), to predict  $r$ -values of an AKDQ steel using texture data obtained from X-ray diffraction. His results are also shown in Fig. 4.7 (Fig. 4.7b).

**4.1.4.4 The Relaxed Constraint Model, RC** As indicated by Hosford et al. (12), one of the major objections to the Taylor model is the fact that the deformation of a single crystal embedded in a polycrystal may not be homogenous. This is consistent with the slip line observations in aggregates which indicate that slip is not uniform within each grain and that the number of active slip systems is less than five, contrary to the Taylor assumption. Also the grain shape argument seems to be a factor that is missing from this analysis (60).

As stated earlier, a variety of RC models have been proposed. These models vary only in the number of shear strains in the local strain tensor that may be 'relaxed' to allow the grain to deform freely (at least partially). The number of these 'relaxed' shear strains depends on the shape of the grain. The particular model which was used in this study (61), is called the RC3 model, since two shear strains of  $\epsilon_{13}$  and  $\epsilon_{23}$  are relaxed, Fig. 4.8b and c. This model is suitable for flat-shaped grains common in rolled sheets. Examples include IF steels which are processed with heavy hot and cold reductions and AKDQ steels (see the processing discussions in Chapter 2 and Fig. 2.2). The main argument here is that for the flat-shaped grains, the continuity of strain across the smaller grain boundaries is fulfilled only within a limited volume fraction contiguous with these boundaries. The two 'relaxed' shear strains lead to very small displacements which can be easily accommodated in the grain boundary re-

gions, Fig. 4.8 (60).

This modification is relatively minor in terms of changes that it brings about in the computations involved in the full constraint theory. By 'relaxing' the two shear strains,  $\epsilon_{13}$  and  $\epsilon_{23}$ , Eqn. 4.26 is thus reduced to three equations and n unknowns. Based on the work of Franciosi (76), Daniel and Jonas (61) adopted a mixed slip mode on only  $\{110\}$  and  $\{112\}$  planes to calculate M per unit  $CRSS_{110}$ :

$$(4.31) \quad \frac{W}{CRSS_{110}} = M = \sum_{s=1}^{12} dy_s^{110} + CR_1 \sum_{s=1}^{12} dy_s^{112}$$

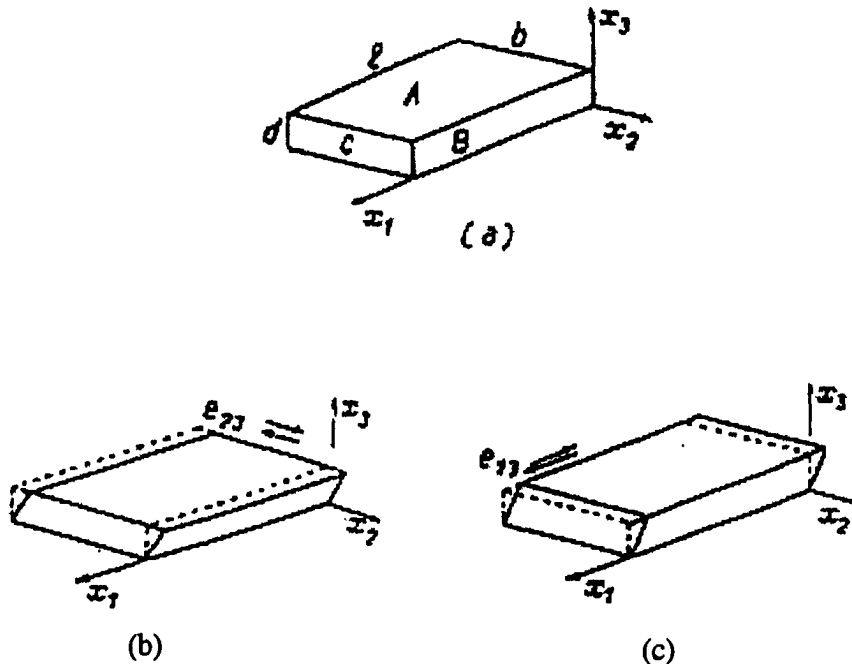


Fig. 4.8 'Relaxation' of shear strains in 'pancake' grains (60)

where  $CR_1$  is defined in Eqn. 4.23. Also, based on considerations regarding the reported range of  $CR_1$  (Table 4.1), these authors selected three values for this quantity, 0.9, 0.95 and 1 which were used throughout the calculations. Using the series expansion technique, this method led to three sets of  $m_\lambda^{\mu\nu}$  coefficients (up to order  $\lambda=22$ ) for each  $CR_1$ .

It should be mentioned here that the  $r$ -value calculated in the framework of the Taylor theory corresponds to  $r_{\text{regression}}$  discussed in Chapter 2. This assumes that the texture of the sheet has not changed significantly during the tensile test. In view of the reported observations regarding this change (not significant after the first 5%), this assumption is reasonable. Chapter 5 will demonstrate some of the results obtained using this model on the material used in this study.

## CHAPTER 5

### EXPERIMENTAL TECHNIQUES AND RESULTS

#### 5.1 Approach

The overall approach in designing experiments to achieve the objectives of this study (enumerated in Chapter 5, section 1.5) was to use Ultra-Form to perform ultrasonic measurements on a statistically appropriate number of deep drawing grade steel samples and to compare predictions with tensile data. Four major areas were considered to be necessary to be explored: a) The reproducibility of ultrasonic measurements, b) Their sensitivity to the microstructure of the steel sheets (texture), c) The factors affecting the relative value of the predictions, and d) The evaluation of the performance of a deformation model in contrast to the empirical correlations of Mould and Johnson (Eqns. 1.8 and 1.9), which had previously been programmed in Ultra-Form to predict  $r$ -values (2). The ultrasonic measurements were to be performed in the Ames Laboratory while the tension tests were to be performed by the industrial research partners according to their own tensile testing procedures. This procedure seemed reasonable, since, for this technology to gain acceptability in an industrial environment, its predictions would have to be compared with the results obtained by industry according to their own procedures rather than by a controlled laboratory tensile test. Neutron diffraction measurements were also to be performed on a selected group of samples as an independent check on the ultrasonic measurements of ODC's.

As is evident from the discussions in Chapters 2-4, the formability of steel is a strong function of thermomechanical processing, chemical composition and microcleanliness (The latter is particularly true with regard to the effects of impurities on CRSS as stated in Chapter 4). Therefore, the strategy throughout the design phase was to gain as much information as possible regarding the chemistry, properties and microstructure (texture) of the common

---

deep drawing grade steels, including a detailed understanding of the tests commonly employed to determine those quantities (i.e. tensile testing and X-ray or neutron diffraction). A considerable amount of effort was therefore expended, including a fact-finding trip to Detroit by the author to consult with the industrial partners regarding these matters. Some of these findings were described in Chapters 1-3 regarding general formability issues and the associated industrial problems, mill processing stages, their impact on the microstructure of low carbon steels, and the tension test and its limitations.

This chapter describes the experimental techniques used in this study, which include ultrasonic velocity, tensile and neutron diffraction measurements. All the associated experimental results, as well as the results obtained by using the RC model (described in Chapter 4) will be presented. These include data on the reproducibility of ultrasonic measurements, and on experimental correlations between ultrasonic parameters, texture coefficients and the tensile data ( $\bar{r}$  and  $\Delta r$ ). Data obtained by using neutron diffraction was used to examine the effects of truncation of higher order ODC's in ultrasonic prediction of plastic properties as well as to independently check the accuracy of ultrasonic measurements of texture coefficients. Where appropriate, the ideal texture orientations of low carbon steels were also simulated. These simulations, when compared with the experimentally predicted angular variation of r-values or Young's modulus, were found to give a good qualitative indication of the major orientations present in these steels. These results will also be presented here. Chapter 6 will address the conclusions drawn from these results.

## 5.2 Steel Samples

The steel samples selected were among the most commonly used grades in stamping operations. Following the guidelines discussed in Chapter 2, these were chosen to be IF, AKDQ, BH, HSLA steels and a special phosphorized high strength grade (denoted by HS,

manufactured by National Steel Corporation which is used in outer body panels in automobiles). Tables 5.1 and 5.2 provide complete information regarding their chemical composition, gages, pertinent properties ( $\bar{r}$ ,  $\Delta r$ ) and  $\delta r$ . The latter is defined as the anisotropy in the rolling plane (i.e. the difference between  $r$  at 0 and 90 degrees with respect to the rolling direction).

In selecting the number of steels, a significant effort was expended to make a statistically appropriate decision in sampling the steels. The emphasis here was to determine the number of samples necessary that would produce a statistically significant confidence level in determining the experimental correlations between ultrasonic velocities and the tensile data. To sample properly, the previous results reported by Hirao et al. (78) were used. These authors reported a linear relationship between their measured ultrasonic velocities and  $r$ -values for a number of similar drawing grade steels. Therefore, a statistical regression analysis was performed (on their data) to determine the minimum number of samples necessary to achieve an acceptable error (standard deviation) for the mean of the velocities to be measured. This analysis indicated a need for a minimum of 10 grades with 95% confidence.

Moreover, to raise the confidence level further, this minimum number was increased to include as wide a range of  $r$ -values as possible. Eventually 26 lifts of steel were obtained. A lift is usually a piece cut out of the steel coil with a length of 96 in. (2.4 m) which has the same width as that of the coil. Having the steels in this form served the purpose of testing the reproducibility of the ultrasonic measurements throughout the lifts as well. Each lift was cut to 10-12 pieces of 20 in. by 20 in. (0.5 by 0.5 m) for ultrasonic measurement. This particular size was chosen to minimize the edge effects (due to the echo of the pulses). Moreover, by making consecutive measurements on lifts, useful information was obtained regarding the sensitivity of the ultrasonics to the variability of texture in the lift, which is of importance for quality control operations. The total number of samples tested was therefore about 260

Table 5.1 Properties of the steels studied

Company	Grade	Gage (mils)	Coating (mils)	$\bar{r}$	$\Delta r$	$\delta r$
National	IF1	31.50	0.75 (EG)	1.89	0.50	0.44
"	IF2	24.00	0.74 (HDA)	2.28	0.48	0.80
"	IF3	28.00	0.59 (HDA)	2.00	0.56	0.50
"	IF4	30.00	0.68 (HDA)	1.77	0.32	0.06
LTV	IF5	28.00	0.74 (EG)	2.00	0.06	0.79
"	IF6	31.00	0.93 (EG)	1.98	0.30	0.70
"	IF7	29.00	0.00	1.81	*	*
"	IF8	30.00	0.95 (HD)	1.85	*	*
"	IF9	26.00	0.10 (Ni)	2.31	0.26	0.82
"	IF10	28.00	1.06 (HD)	1.88	0.11	0.39
"	IF11		*	1.78	0.26	0.53
National	AKDQ1	28.00	0.77 (EG)	1.63	0.56	0.41
"	AKDQ2	33.50	0.00	1.42	0.55	0.03
"	AKDQ3	25.00	0.00	1.50	0.46	0.19
LTV	AKDQ4	33.00	0.78 (EG)	1.45	0.65	0.02
"	AKDQ5	29.00	1.10 (EG)	1.54	0.53	0.29
National	BH1	31.00	0.76 (EG)	1.57	0.46	0.30
"	BH2	31.00	0.76 (EG)	1.59	0.38	0.43
"	BH3	29.50	0.79 (EG)	1.77	0.41	0.42
LTV	BH4	30.00	0.00	1.21	*	*
"	BH5	31.00	0.76 (EG)	1.49	0.74	0.32
National	HS1	27.60	0.62 (EG)	1.64	0.53	*
"	HS2	30.00	0.66 (HDA)	1.97	0.68	-0.25
"	HS3	27.00	0.72 (HDA)	1.51	0.39	0.38
"	HSLA1	33.00	0.88 (EG)	1.15	-0.04	0.18
"	HSLA2	39.00	0.75 (EG)	*	*	*

\* The tensile data were not available on these samples

Table 5.2 The chemical composition of the steels studied

Grade	$\bar{r}$	%W							
		C	Mn	P	S	Si	Al	Ti	Cb
IF1	1.89	0.0078	0.21	0.007	0.008	0.010	0.043	0.056	----
IF2	2.28	0.0037	0.23	0.010	0.009	0.010	0.058	0.069	----
IF3	2.00	0.0034	0.24	0.011	0.005	0.010	0.046	0.052	----
IF4	1.77	0.0074	0.58	0.028	0.009	0.011	0.059	0.041	0.019
IF5	2.00	0.0050	0.12	0.010	0.003	----	0.032	0.049	0.032
IF6	1.98	0.0050	0.19	0.008	0.006	0.008	0.040	0.031	0.030
IF7	1.81	0.0040	0.09	0.004	0.003	----	----	0.063	----
IF8	1.85	0.0050	0.12	0.008	0.01	----	----	0.069	----
IF9	2.31	0.0040	0.14	0.007	0.009	----	----	0.049	----
IF10	1.88	0.0055	0.12	0.005	0.005	----	----	0.055	0.029
IF11	1.78	*	*	*	*	*	*	*	*
AKDQ1	1.63	0.0280	0.23	0.007	0.015	0.010	0.068	----	----
AKDQ2	1.42	0.0450	0.25	0.009	0.019	0.005	0.050	----	----
AKDQ3	1.50	0.0330	0.23	0.008	0.013	0.010	0.063	----	----
AKDQ4	1.45	0.0520	0.24	0.005	0.012	----	0.060	0.003	----
AKDQ5	1.54	0.0380	0.24	0.007	0.007	0.004	0.060	0.006	----
BH1	1.57	0.0100	0.22	0.040	0.010	0.010	0.063	----	----
BH2	1.59	0.0074	0.20	0.036	0.011	0.010	0.042	----	----
BH3	1.77	0.0230	0.20	0.038	0.014	0.050	0.076	----	----
BH4	1.21	0.0400	0.25	0.01	0.009	0.015	----	----	----
BH5	1.49	0.0200	0.22	0.01	----	0.010	0.044	----	----
HS1, 4	1.64	0.0370	0.37	0.055	0.012	0.010	0.049	----	----
HS2	1.97	0.0070	0.60	0.034	0.008	0.015	0.065	0.041	0.026
HS3	1.51	0.0370	0.39	0.053	0.013	0.010	0.053	----	----
HSLA1	1.15	0.0500	0.32	0.041	0.020	0.010	0.034	----	0.015
HSLA2	*	0.0800	0.40	0.007	0.011	0.005	0.074	----	0.074

samples. The reproducibility results for these samples will be presented later in this chapter.

As Table 5.1 shows, the  $\bar{r}$  for these steels varied from a minimum of 1.15 (HSLA1) to 2.31 (IF9) while  $\Delta r$  varied from -0.04 (HSLA1) to 0.74 (BH5). The thicknesses of these steels were all within the range used in automotive applications varying from 24 mils (0.6 mm) (IF2) to 39 mils (1 mm) (HSLA2). The steels were all cold rolled, batch annealed (except for IF7-IF11 which was continuously annealed) and galvanized, except for 4 lifts which were uncoated (IF7, AKDQ2, AKDQ3 and BH4).

The coating thickness on the samples varied from 0.1 mils (0.002 mm) (IF9) to 1.1 mils (0.02 mm) (AKDQ5). Most of these coatings were G-type electrogalvanized or hot dipped (denoted by EG or HD in Table 5.2), and A-type hot dipped galvanized (denoted by HDA in Table 5.2). One lift was coated on one side only with the coating being nickel oxide (IF9). These coatings tend to reduce the ultrasonic velocities, (In a similar manner the frequency of oscillations of the coupons in the Modul-r instrument are also reduced by the presence of coatings). Since use of galvanized sheets is routine in industry, it was decided to include a study of coated steels in this research. For this reason, at this point, it may be appropriate to briefly describe the process of galvanizing steels.

The main purpose in galvanizing steel sheets is to minimize corrosion. There are two major types of galvanizing that are used in the auto industry (43). The first type is called hot dipping where the substrate (the cold rolled steel) is passed through a bath of molten zinc. Here, the substrate is usually heated to high temperatures to ensure that the steel is at the same temperature as the zinc bath. Therefore, hot dipping involves a chemical reaction between zinc and the steel which may also change the properties of the substrate. Moreover, the zinc bath can not be completely pure. In order to restrict the thickness of the resulting intermetallic alloy layer, to optimize coating adherence and to prevent flaking in forming operations, aluminum (0.1-0.25%) is usually added which results in the formation of  $\text{FeAl}_3$  or

$\text{Fe}_2\text{Al}_3$  compounds. These compounds tend to retard the growth of the zinc-iron layer. Other additions include small amounts of antimony, cadmium and larger amounts of lead to alter the size of the coating spangles. This kind of galvanizing is designated by the G-type coating label. There is another type of hot dipped coating called galvanized, where the coating material consists entirely of zinc and iron (90% zinc and 10% iron). This type of coating (which is designated by the symbol A) has a gray matt finish and exhibits better paint adherence, weldability and tolerance for moderate forming operations.

The second major type of galvanizing is electroplating where the zinc is bonded to the strip by an electrochemical process. Unlike the hot dipping process, the electrogalvanizing (EG) is carried out 'cold' (at room temperature), and thus no diffusion takes place. Instead, a tight bond is formed between the steel and the electrolytically deposited zinc by a sharing of electrons at the interface. Usually the strip passes through a series of electrolytic cells. In each of the plating cells electrical current flows through a zinc or zinc-sulfate solution from anode to cathode (strip), bonding the zinc to the steel strip. Figure 5.1 shows a high magnification photomicrograph produced at Bethlehem Steel (79) with an oblique view showing the cross-section and coating surface of a typical sample of electrogalvanized sheet (with 50G50G coating mass which corresponds to a minimum of  $50 \text{ g/m}^2$  of coating mass on each side). EG coated plates have a natural matt finish. In the electrogalvanizing process, the properties of the substrate remain unchanged.

The effects of coating on r-values are generally believed to be negligible (43). It may be that if there are any changes relative to the r-values of the cold rolled substrate, then the tension test is not sensitive enough to detect them. However, coatings do have a significant effect on the performance of cupping tests, since as mentioned in Chapter 1, cupping tests (e.g. Swift test) are sensitive to friction. The coatings contribute to the frictional effects and alter the cupping results. However, with a proper choice of lubricants, this effect may be

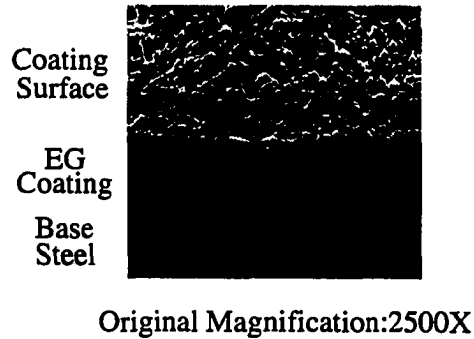


Fig. 5.1 Photomicrograph of an EG coating (79)

minimized (79). The effects of coating on the velocity of ultrasonic pulses will be discussed later in this chapter.

### 5.3 Tensile Tests

As stated previously, the tensile tests in the present research were performed by the industrial partners, and carried out according to their own procedures. National Steel Company uses a manual testing procedure in which ASTM-type tensile coupons (type A) are prepared. The final strain levels, depending on the yield strength of the steel vary from 12%-18% (twelve percent for yield strengths greater than 50 ksi, 15% for yield strengths between 30 and 50 ksi and 18% for yield strengths less than 30 ksi). In the procedure used by the LTV Steel Company extensometers are used where the gage lengths of ASTM tensile coupons are slightly modified to allow the extensometers to fit on the gage section. Here, only one strain is used in calculating r-values (which is equivalent to the manual technique). At Ford Motor

Company an automatic tensile machine is used which also utilizes extensometers. Here, all the data acquisition is automatic with a software that fits a regression line to strains between approximately 5% and 14% levels.

Figure 5.2a shows the comparison between the automatic data and the manual data obtained from some of the steels studied. It is apparent that a large difference exists between the two measurements. This is consistent with the differences seen between manual and automatic measurements of  $r$ -values in previously reported work (69). For comparison purposes, Fig. 5.2b shows the data reported in reference (69). These authors also used an automatic tensile machine with extensometers as sensors. As stated previously (See Chapter 3 Section 3.1.3), the causes for these differences are not clear and this matter will be explored in a later study.

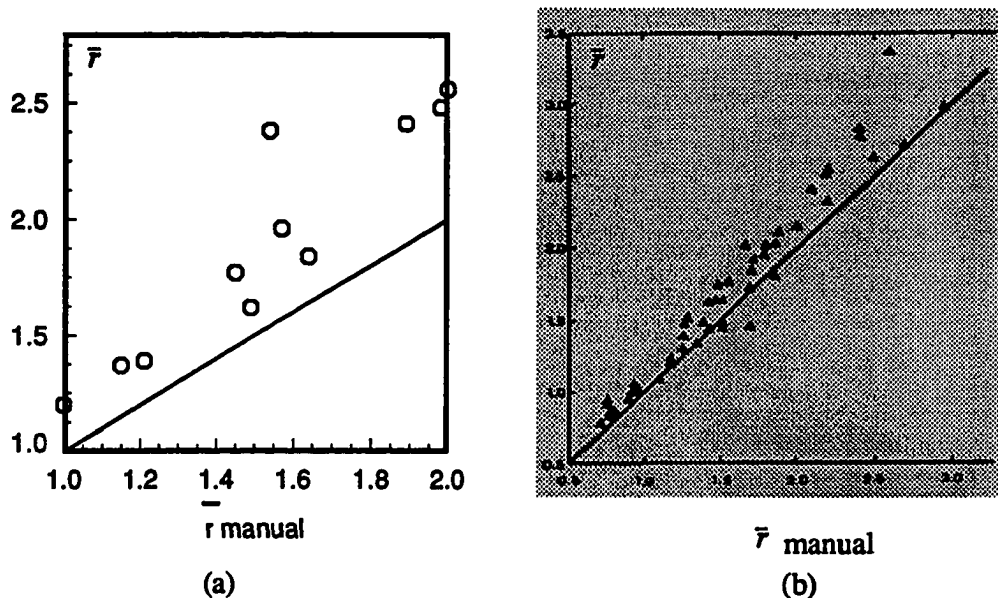


Fig. 5.2 Comparison of automatic data with manual data:

- (a) Data from the present study
- (b) Data from reference (69)

#### **5.4 Neutron Diffraction Measurements**

In order to obtain an independent check of the ultrasonic measurements of texture coefficients, a number of steel samples were examined by neutron diffraction using standard techniques. With the exception of IF steels (where 6 samples were selected) one sample from each category was chosen (one from AKDQ, BH, HS and HSLA steels). This selection procedure led to a total of 10 samples on which neutron diffraction measurements were performed. The reason for selecting a larger number of IF steels was to examine the effects of truncation of higher order ODC's which may have been more important for these steels as indicated in the discussions in Chapter 2. The diffraction tests were performed in Chalk River reactor in Canada.

#### **5.5 Ultrasonic Velocity Measurements**

The two important features of velocity measurements by Ultra-Form are the selection of a proper frequency for operation of the EMAT probes (which also determines the frequency of the generated ultrasonic pulses) and the signal processing technique to measure the speed of the pulses.

##### **5.5.1 Selection of the Operating Frequency for the EMAT Transducers**

The efficiency of the EMAT transducers is a maximum when the wavelength of the guided mode ultrasonic pulses is approximately equal to the period of the meander coils in the EMAT probes (~0.4 in. or 1.02 cm). Therefore, the main controller in the Ultra-Form sets this frequency by using the information supplied by the user given through the touch screen unit (i.e. the density and thickness of the plate and the single crystal elastic constants). As stated in Chapter 4,  $S_0$  Lamb waves are dispersive. In order to calculate their frequency in a textured sheet, it is necessary to solve the Rayleigh-Lamb dispersion relation

which involves solving a transcendental equation. However, considering the fact that the commercially produced sheets are mostly weakly textured, it is possible to treat the plate as an isotropic plate and approximate the solution to Rayleigh-Lamb waves by a 5th degree polynomial (80):

$$(5.1) \quad W = \sqrt{2K} \left[ \sqrt{\frac{1}{1-\nu}} (1 - 4K^3 + 3K^4) + 0.5K^3(1 + K) + 4K^3(1 - K) \right]$$

where

$$(5.2) \quad \begin{aligned} W &= \frac{b\omega}{\pi V_t} \\ K &= \frac{bk}{\pi} \end{aligned}$$

Here, W and K are the nondimensionalized frequency and wavevector (the original variables are  $\omega$  and  $k=2\pi/D$  where D is the period of the meander coils in the EMATs) and b and  $\nu$  are the plate thickness and Poisson's ratio of the plate material.  $V_t$  is the transverse plane wave velocity which is equal to:

$$(5.3) \quad V_t = \sqrt{\frac{\mu}{\rho}}$$

where  $\mu$  is the shear modulus and  $\rho$  is the density. Using Eqn. 5.1 and the information supplied by the user, the main controller in the Ultra-Form calculates the frequency of operation for the EMATs and rounds them off to the nearest 10 kHz integer which can range from 450-550 kHz.

Figure 5.3 shows a flow chart of the sequence of events that takes place leading to the operation of these probes and the eventual velocity calculations employed by the signal processing technique. During the ultrasonic measurements, however, it was observed that on some samples (IF5 and IF9) the measured velocity in the 90 degree direction fell outside of the usual range of values associated with these steels ( $\sim 5.77$  mm/ $\mu$ s) to a much smaller value ( $\sim 5.26$  mm/ $\mu$ s). It was also observed that this problem could be corrected by changing the settings for the elastic constants (mostly  $c_{44}$  which changes  $\mu$  for the polycrystal).

In order to investigate the reason for this observation, a Fortran code was written on a DEC station which calculated the frequency of EMATs exactly in the same way that is done in Ultra-Form as shown in Fig. 5.3. Different sets of elastic constants were used as inputs to this code. The results indicated that the reason for the decrease in velocity is probably due to the fact that Eqn. 5.1 assumes weakly textured plates which assumption is not appropriate for samples IF5 and 9. As will be shown later, these particular steels which have high  $r$ -values (around 2) show strong anisotropy in the rolling plane (i.e. high  $\delta r$ ) due to the particular secondary texture components that are present in their overall texture. Therefore, for these samples, Eqn. 5.1 approached its limits in predicting the correct frequency for operation of EMATs and the rounding-off procedure moved the effective frequencies into the wrong region. The fact that the difference between these velocities corresponds to a difference of approximately 10 kHz in the frequency of operation, confirms this explanation. By changing  $c_{44}$ , the shear velocity in Eqn. 5.3 was changed which, in effect, made the material corresponding to the right hand side of Eqn. 5.1 more anisotropic and therefore led to the

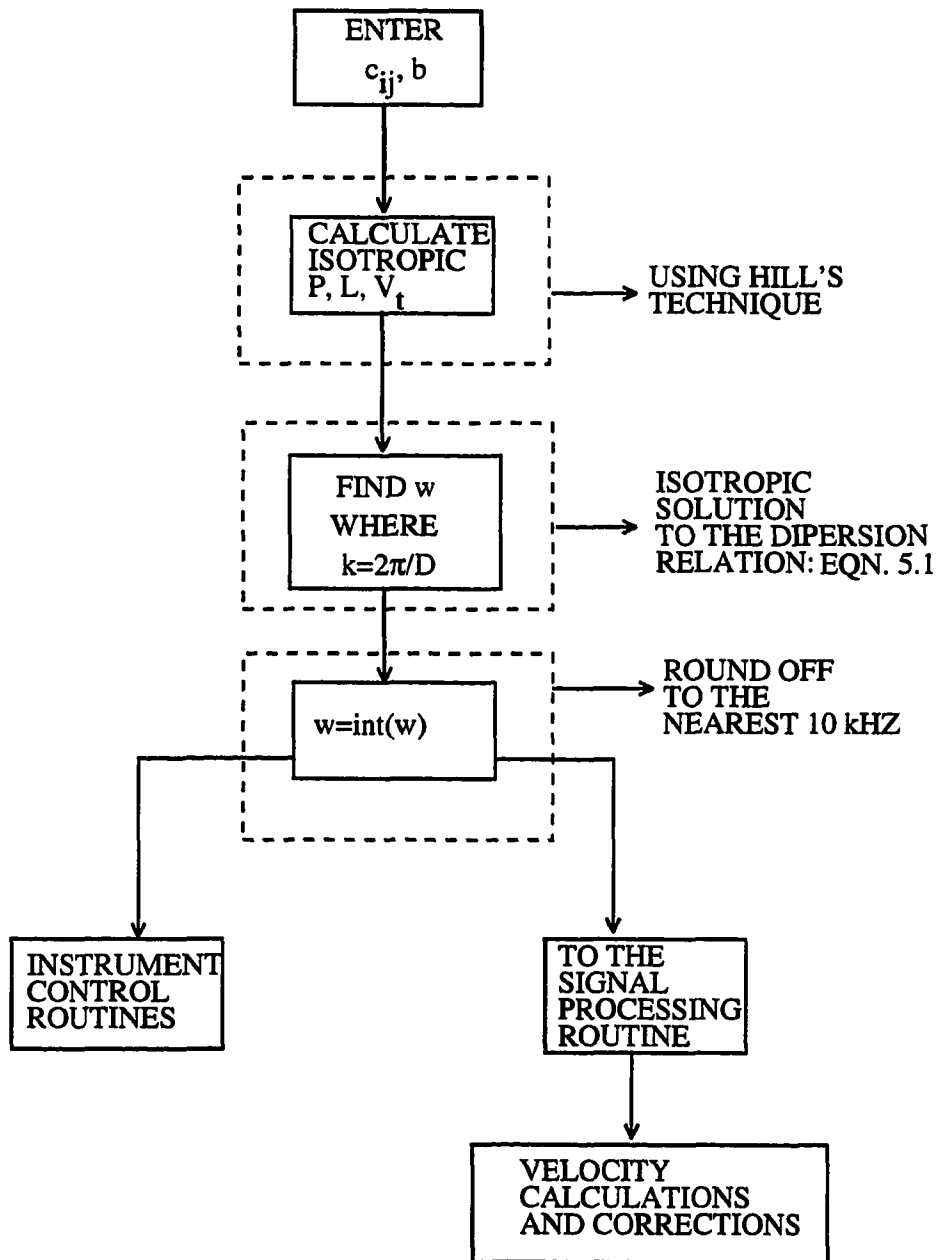


Fig. 5.3 Frequency selection of EMATs in Ultra-Form

correct 90 degree velocities in these samples. Although Eqn. 5.1 yields satisfactory results for almost all of the steels, this observation suggests that it should probably be modified for the effects of stronger textures in IF samples.

### 5.5.2 The Signal Processing Technique and The Dispersion Correction

In order to calculate the ultrasonic velocity in each direction, the primary parameter to be measured is the time of travel of the waveforms between the first and second transmitter coils which value is used. The time delay measurements involve a digital phase-slope signal processing technique which has been described previously (81). In this technique (which is programmed in Ultra-form) the two waveforms are first digitized and then transferred to the frequency domain by applying the Fast Fourier Transform (FFT). The time delay is given by the slope of the phase-frequency curve as shown in Fig. 5.4. This curve for nondispersive propagations is a straight line. If dispersion is present, this relationship becomes nonlinear and the stronger the dispersion, the stronger is the degree of the nonlinearity present in the phase-frequency plot. The principle feature of a dispersive pulse is that it does not retain its shape as it propagates through the medium. Thus, a short-duration pulse may be dispersed into extended wave trains in time. Here, the crests and troughs are propagated with the phase velocity,  $V_p = \omega/k$ . The wave packet, however, travels with the group velocity,  $V_g = d\omega/dk$ . This is the velocity at which the energy associated with waves of a given length is propagated. For a nondispersive propagation, the two velocities are equal.

The value of the speed of Lamb waves used in the theoretical discussions of Chapter 4 (Section 4.1.3) is the long wavelength (low frequency) limit of the velocity. Due to dispersion, the group velocity is a function of frequency (i.e. due to nonlinearity in the phase-frequency plot, Fig. 5.4, the slope depends on frequency). Therefore, in measuring speeds of Lamb waves in steels, a second order polynomial is fitted to the phase frequency data. To

minimize the effects of random noise, only the data within the bandwidth of the signals is considered since these points have superior signal-to-noise ratios. The slope of the phase-frequency curve is then calculated at the peak frequency leading to the calculation of  $V_p$  at the peak (Fig. 5.4). The so-obtained velocity is then corrected for the effects of dispersion.

Since dispersion is usually small at wavelengths large with respect to the typical plate thicknesses encountered in this study, the dispersion correction programmed in Ultra-Form is based on the theory of Lamb waves in isotropic plates. Strictly speaking, this correction should be based on the theory of Lamb waves in orthotropic plates taking into account the texture of the sheet (i.e. texture coefficients) (37). However, since texture induced velocity anisotropy of commercially produced rolled sheets are in general weak, the isotropic approximation is reasonable.

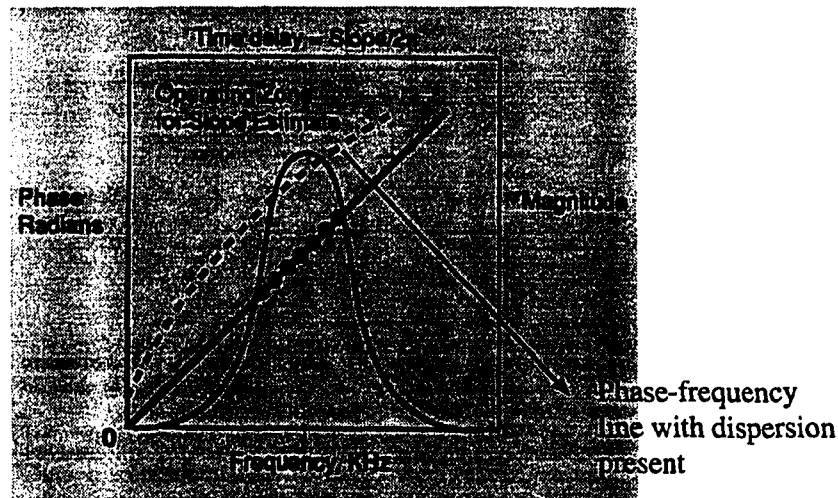


Fig. 5.4 The phase-frequency plot

### 5.5.3. Coating Effects

The effect of coatings on ultrasonic velocity has been experimentally investigated by Hirao et al. (38). Their findings show that the presence of coatings on sheets tend to lower the speed of the pulses since zinc is an 'elastically soft' material. This effect is similar to the effect of coatings on the resonant frequencies of coupons measured by the Modul-r instrument as reported in reference (30) (See Chapter 3, Section 3.2.2). An approximate formula has been suggested by Hirao et al. (38) which compensates for the coating effects on ultrasonic speed. In deriving this formula, these authors have made three assumptions: 1) The zinc coating is isotropic in itself, 2) The coating is much thinner than the substrate, and 3) The sheet is thin enough to assume a uniform strain through the entire thickness (38). These authors have pointed out that zinc generally shows a strong elastic anisotropy and sharp texture, however, for very thin coatings this effect may be less important.

Based on a plane stress assumption for an elastically stretched isotropic substrate, the velocity of pulses in the coated sheet was expressed as a function of the thickness of the coating and the elastic constants of iron and zinc:

$$(5.4) \quad V_{coated} = V_{uncoated} \left[ 1 + 0.5 \left( \frac{\Delta d}{d} \right) \left( \frac{M^{Zn}}{M^{Fe}} - \frac{\rho^{Zn}}{\rho^{Fe}} \right) \right]$$

Here,  $\Delta d$  is the thickness of the coating and  $d$  is the half-thickness of the plate as shown in Fig. 5.5.  $M$  is  $c_{11}$  calculated for an isotropic polycrystal. Using a typical set of elastic constants for iron and zinc, Eqn. 5.4 will change to the following:

$$(5.5) \quad \frac{V_{coated}}{V_{uncoated}} = 1 - 0.222\left(\frac{\Delta d}{d}\right)$$

As Hirao et al. (38) point out, this correction will affect the ultrasonic predictions of normal anisotropy as indicated by  $W_{400}$  and  $\bar{V}$ , but it will not affect the predictions of planar anisotropy.

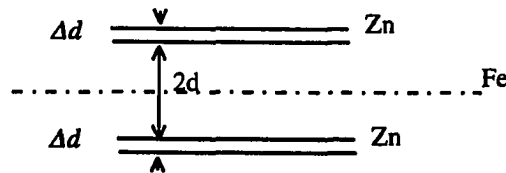


Fig. 5.5 The relative position of the coating

In order to investigate the effects of coatings on ultrasonic predictions of properties, both the corrected velocities (corrected by using Eqn. 5.5) and the actual measured velocities on the coated samples were used in the analysis. Table 5.3 shows the speeds of ultrasonic pulses in two samples of AKDQ4 and AKDQ5. The ultrasonic velocities in two uncoated samples are also included (AKDQ2 and AKDQ3). While these samples are not exactly identical to AKDQ4 and AKDQ5, they have very similar chemistries and properties (i.e. comparable  $r$ -values, as shown in Table 5.2 and 5.3) and may provide a reasonable reference point for comparison purposes.

It appears that the coating indeed has reduced the speed in the AKDQ4 material which is consistent with findings reported in reference (38). However, for the AKDQ5 material, the actual measured velocity (i.e. the uncorrected one) seems to be almost identical to the speed in the uncoated sample, AKDQ3. The reason for this observation is not clear, but it may be due to nonuniformities in coating thickness throughout the coil.

Table 5.3 The actual coated velocities

Steel Sample	Tensile $\bar{r}$	Coated velocity $\bar{V} \text{ m / s}$	$\frac{\Delta d}{d}$
AKDQ2 (uncoated)	1.42	5600.8	0.000
AKDQ4	1.45	5584.5	0.023
AKDQ3 (uncoated)	1.50	5599.5	0.000
AKDQ5	1.54	5598.1	0.037

Moreover,  $r$ -values predicted by various empirical models (Mould-Johnson, and RC models) to be described later in this chapter, indicate that use of the coating correction actually overestimates the predicted  $r$ -values by 0.1 to 0.2. The reason for this, is that Eqn. 5.5 affects the ultrasonic predictions of normal anisotropy indicated by the texture coefficient,  $W_{400}$ . Figure 5.6 shows a comparison between  $W_{400}$  values measured using neutron diffraction and those obtained from the ultrasonic technique for some of the samples studied. Here it can be seen that there is an excellent agreement between the uncorrected  $W_{400}$  values and the diffraction measurements. It is evident that the correction scheme indeed overes-

estimates significantly the actual effects of coatings on the velocities of the pulses. These results indicate that the coating thicknesses of the steels were not large enough to warrant the use of Eqn. 5.5. The values of the ratio,  $\frac{Ad}{d}$  for the steels studied here are shown in Fig. 5.7. On the average, this ratio is approximately equal 0.026.

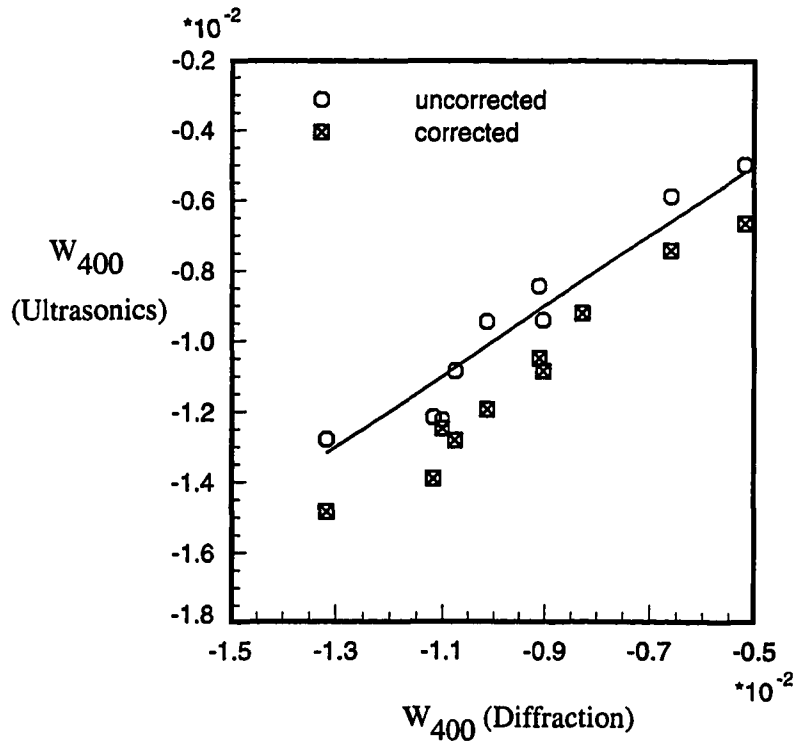


Fig. 5.6 The comparison of the corrected and uncorrected  $W_{400}$  with diffraction

Figure 5.8 shows the results obtained by Hirao et al. (38). These authors used several samples of the same cold rolled substrate which were electroplated with successively increasing coating thicknesses. The coating thicknesses used in the present study (ratio of  $\sim 0.026$ ) are at the low end of the scale on Fig. 5.8 where the differences between the times

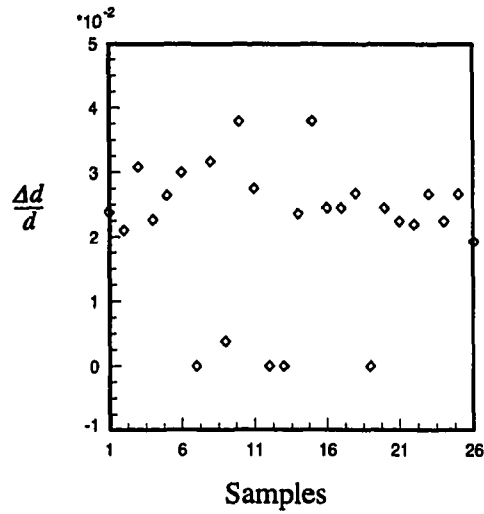


Fig. 5.7 The coating thickness ratio for the steels studied

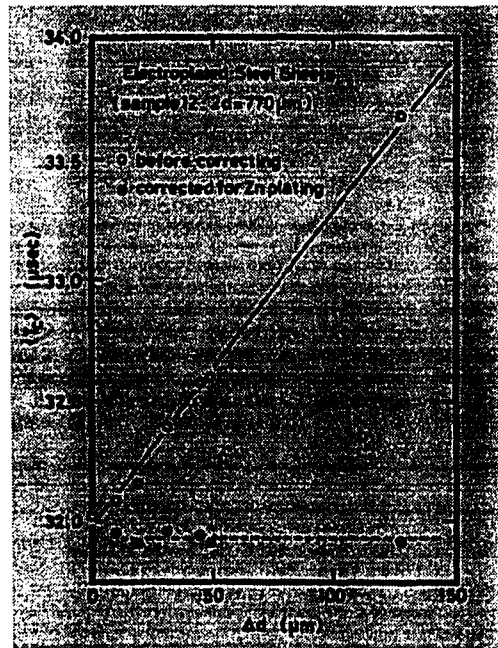


Fig. 5.8 The coating correction data from reference (38)

of flight,  $T_c$ , in coated and uncoated sample can be seen to be very small. Moreover, the correction formula seems to systematically overestimate the times of flight of the coated samples (shown with a dashed line) relative to the original uncoated one. The authors have attributed this observation to the texture of the zinc, but it is probably due to the inaccuracies of the choice of elastic constants for zinc and iron. It will be shown later, that a proper choice of elastic constants (which should be representative of the chemical composition of the material) plays an important role in ultrasonic predictions of normal anisotropy. This statement may be further qualified by the fact that, as stated in previous sections, the G-type coatings are not entirely pure zinc and have other constituents in them as well (i.e. zinc-sulfate or aluminum). This changes the accuracy of the correction formula, since this formula uses the elastic constants of pure zinc.

The data here indicate that within the range of the coating thicknesses encountered in this study (a typical range for the automotive applications), the coatings do not have any significant effect on the ultrasonic predictions of r-values and their presence can be ignored.

### **5.6 Repeatability Data**

Table 5.4 presents the variabilities of r-values and ultrasonic velocities through each lift of steel measured by observing changes in ultrasonic predictions of r-values (Mould and Johnson correlation) from sample to sample. The percent variations shown in Table 5.4 are the coefficients of variation which are expressed as the ratio of the standard deviation to mean calculated with 95% confidence. This uncertainty is a measure of the consistency of ultrasonic predictions as well as the uniformity of texture from measurement-to-measurement on nominally identical samples that came from the same lift. In order to compare this with the inherent electronic and probe positioning errors, two classes of tests were performed. First, the probe was left stationary on one sample. The measurement was re-

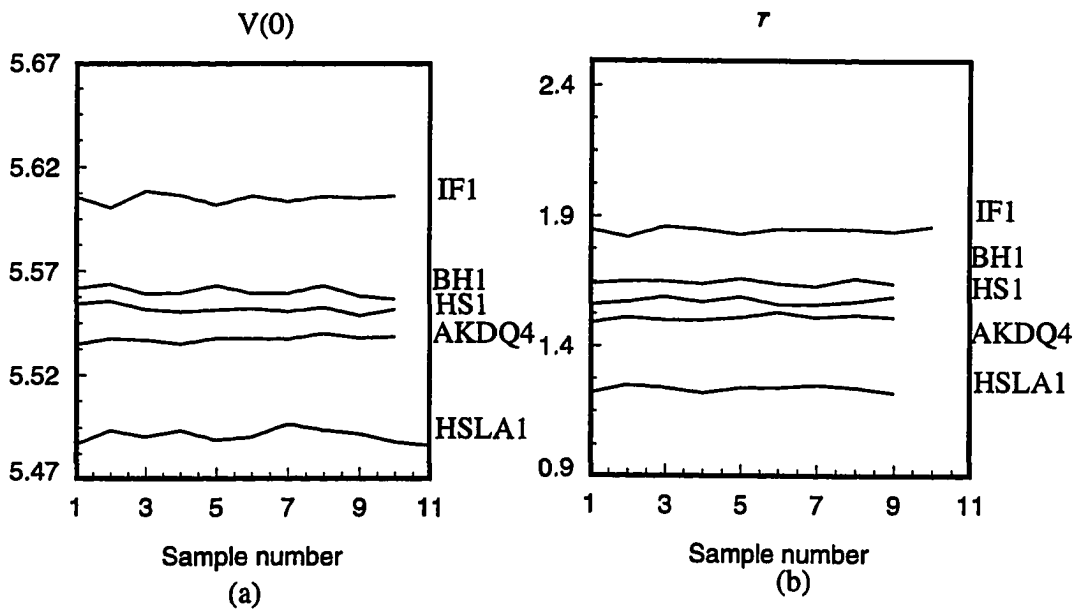
peated 10 times after which the standard deviation of repeatability was calculated. Second, the probe was repositioned on the same sample 10 times to examine the error caused by repositioning the probe. Table 5.5 shows the results. In all cases, with 95% confidence, these errors were smaller than the variation of r-values and velocities throughout the lifts caused by mill processing as shown in Table 5.4. This is significant since sensitivity to subtle changes in crystallographic texture caused by mill processing is important should this technology be used on-line in the future. Also the low repeatability error of the velocities indicates a good electromagnetic coupling existing between the probes and the sheets which again is important from the perspective of on-line use of this technology. Figures 5.9a and b show the variations of velocity and  $\bar{r}$  throughout the lifts of some of the steels studied.

Table 5.4 %Variations seen throughout the lifts

<b>Steel Type</b>	<b>± % Variation in <math>\bar{r}</math></b>	<b>± % Variation in v(0)</b>	<b>± % Variation in v(45)</b>	<b>± % Variation in v(90)</b>
IF1	0.4	0.03	0.01	0.14
IF6	0.4	0.19	0.04	0.63
AKDQ3	0.4	0.10	0.03	0.05
AKDQ4	0.37	0.02	0.01	0.02
BH1	0.42	0.03	0.02	0.02
BH4	0.70	0.22	0.03	0.30
BH5	0.86	0.46	0.03	0.60
HSLA1	0.65	0.13	0.03	0.14
HSLA2	0.64	0.01	0.03	0.01
HS1	0.57	0.02	0.02	0.05

Table 5.5 The repeatability error in ultrasonic readings

Probe Position	%Error in Reading $\bar{r}$	%Error in $v(0)$	%Error in $v(45)$	%Error in $v(90)$
Probe being lifted and put down on one sample	0.2	0.01	0.009	0.01
Probe remains stationary on one sample	0.2	0.01	0.01	0.005

Fig. 5.9 The variation of  $V(0)$  and  $\bar{r}$  in some of the lifts studied

### 5.7 Experimental Correlations

Figures 5.10a-c and 5.11a-d show the experimental correlations obtained between the measured ultrasonic data and the tensile data. These include the data pertaining to the normal anisotropy (i.e.  $\bar{V}$ ,  $\bar{E}$  and  $W_{400}$  vs  $\bar{r}$ ), planar anisotropy (i.e.  $\Delta V$ ,  $\Delta E$  and  $W_{440}$  vs  $\Delta r$ ) and anisotropy in the rolling plane (i.e.  $W_{420}$  vs  $\delta r$ ). Each data point in these figures represents an average of 10-12 measurements per lift. Therefore, they are indicative of the correlations existing between the ultrasonic data and plastic properties of each lift of the steels studied. The regression polynomial lines (first and second order) along with their respective correlation coefficients are also shown. Table 5.6 also compares the obtained correlation coefficients with the standard ones at 1% significance level (99% confidence).

Table 5.6 Comparison of the correlation coefficients with the standard ones at 1% significant level

Correlations	Correlation coefficients	1%Significance Level
$\bar{r} - \bar{V}$	87.0	52.6
$\bar{r} - \bar{E}$	87.0	52.6
$\bar{r} - W_{400}$	87.0	52.6
$\Delta r - \Delta V$	91.0	56.1
$\Delta r - \Delta E$	89.0	56.1
$\Delta r - W_{440}$	91.0	56.1
$W_{420} - \delta r$	76.0	56.1

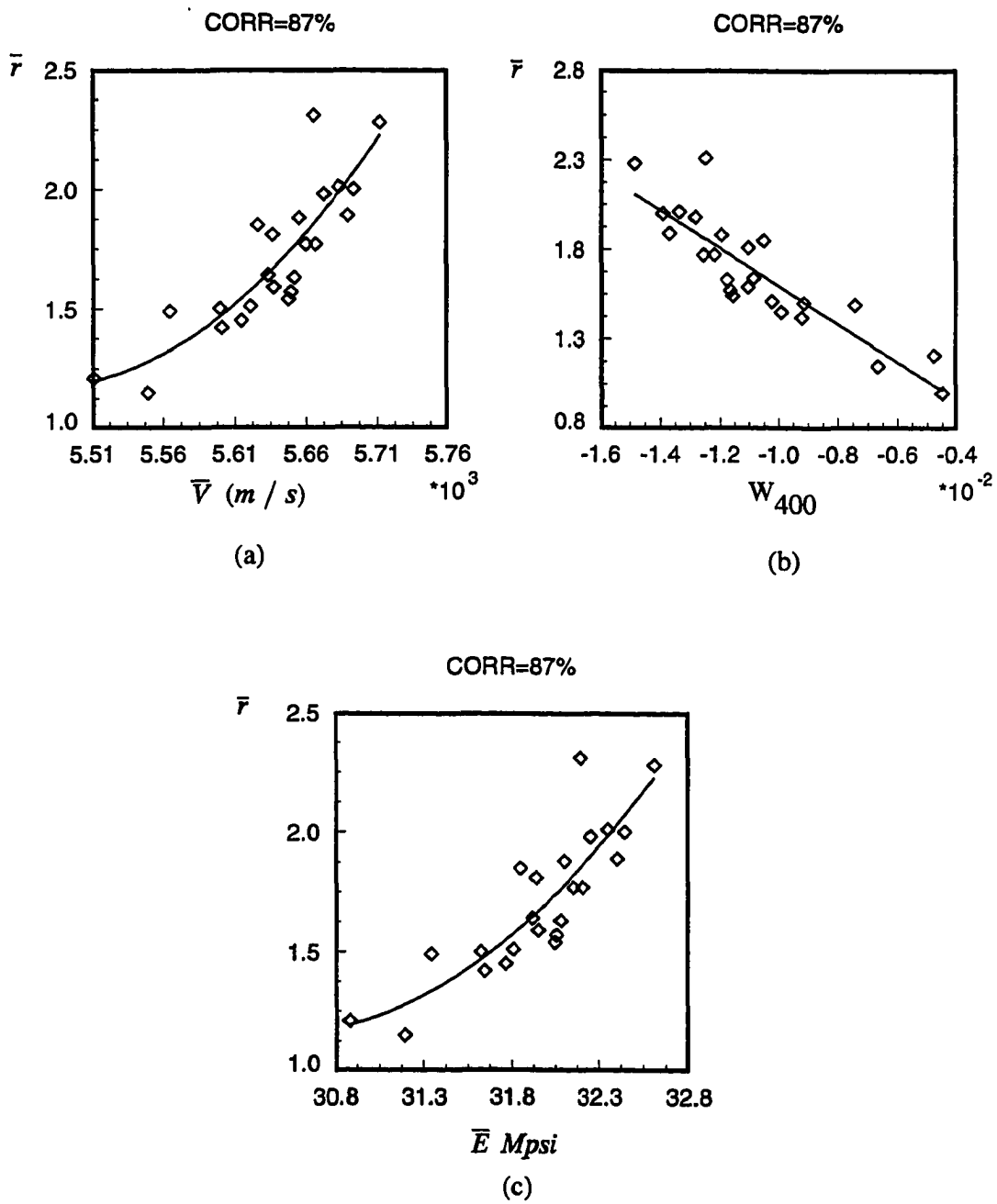


Fig. 5.10 The experimental correlations (normal anisotropy)  
(solid lines are lines of best fit)

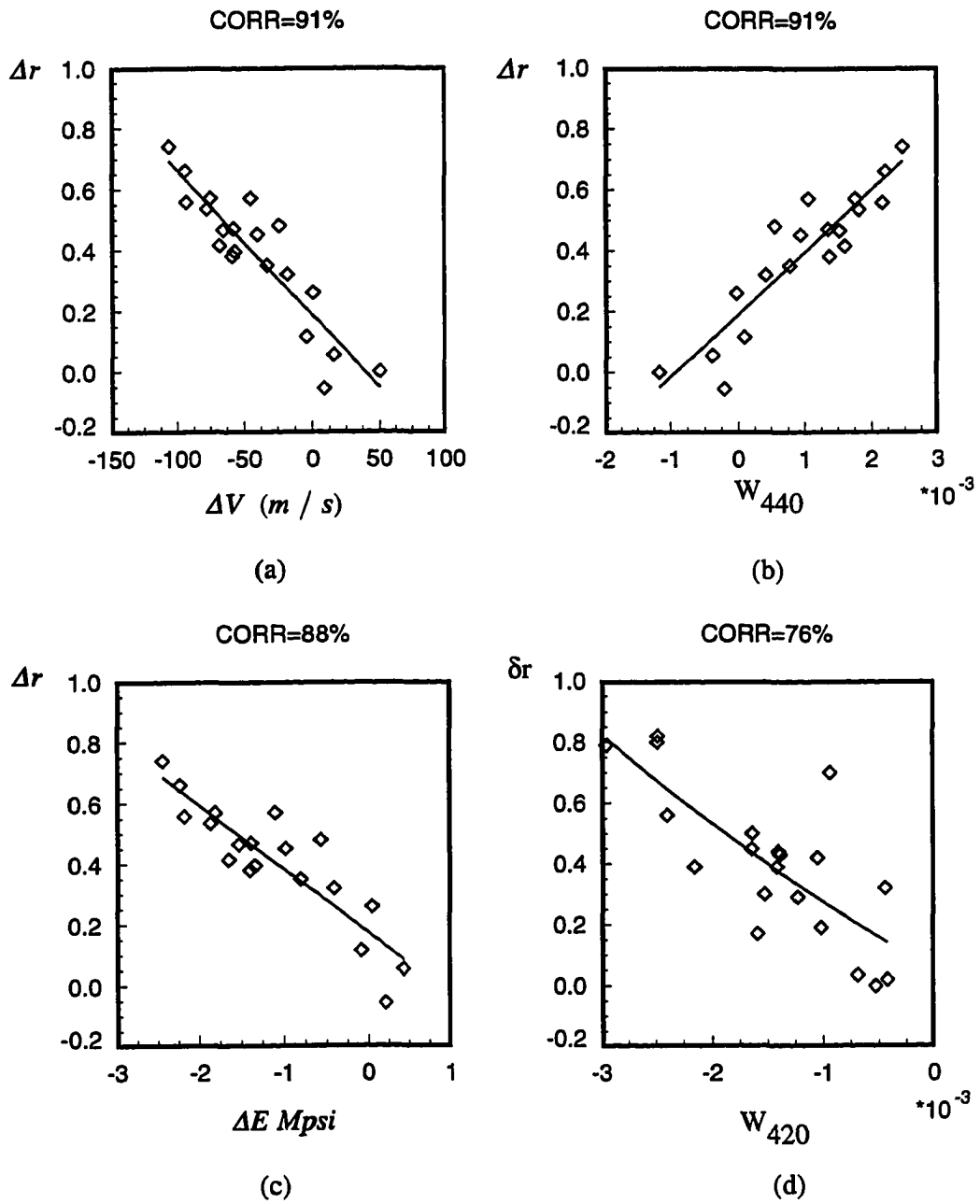


Fig. 5.11 The experimental correlations ( planar anisotropy)  
(solid lines are lines of best fit)

It is evident that a significant correlation between the ultrasonic parameters and the tensile data exists. An important conclusion here is the reasonably good correlation obtained between  $W_{420}$  and  $\delta r$  shown in Fig. 5.11d. This texture coefficient, which represents the anisotropy in the rolling plane, is more difficult to measure accurately for steels with textures that lead to small  $\delta r$  values (e.g. AKDQ2 and AKDQ4, Table 5.1). The difficulty in measuring  $W_{420}$  is due to the small differences that exist between the velocities in the rolling and transverse directions, relative to the small absolute value of this parameter itself (order of  $\sim 10^{-4}$ ). During the repeatability experiments, it was observed that the repeatability error for  $W_{420}$  approached the absolute value of the magnitude of  $W_{420}$  itself, for steels that showed a small degree of anisotropy in the rolling plane. For this reason the level of scatter is higher for this particular texture coefficient. However, the high level of the correlation coefficient demonstrates the sensitivity of the ultrasonic velocity as an indicator of texture of the steels and the good accuracy of the EMAT technology used in Ultra-Form.

A useful observation regarding IF samples can be made by study of the data presented in Figs. 5.12a-c. Here, the  $\bar{r} - \bar{V}$  data corresponding to the IF steels (Fig. 5.12a) and all the non-IF steels (Fig. 5.12b) have been compared. It appears that the level of scatter for IF steels is higher than for the non-IF steels with the correlation coefficient reduced drastically to 56% (this scatter was not limited to velocities alone, it included other parameters such as Young's modulus, texture coefficients, etc. with an identical reduction in their correlation coefficients when compared to non-IF data). Also, previous observations that were made regarding the data that was obtained by Ultra-Form in 1990 (2), pointed to the same level of scatter (Chapter 1, Fig. 1.8).

However, if one excludes the data point observed on IF9 (shown by a circle in Fig. 5.12a), the correlation coefficient improves significantly (shown in Fig. 5.12c) which suggests that this particular data point is an outlier. One may also separate the IF data into two

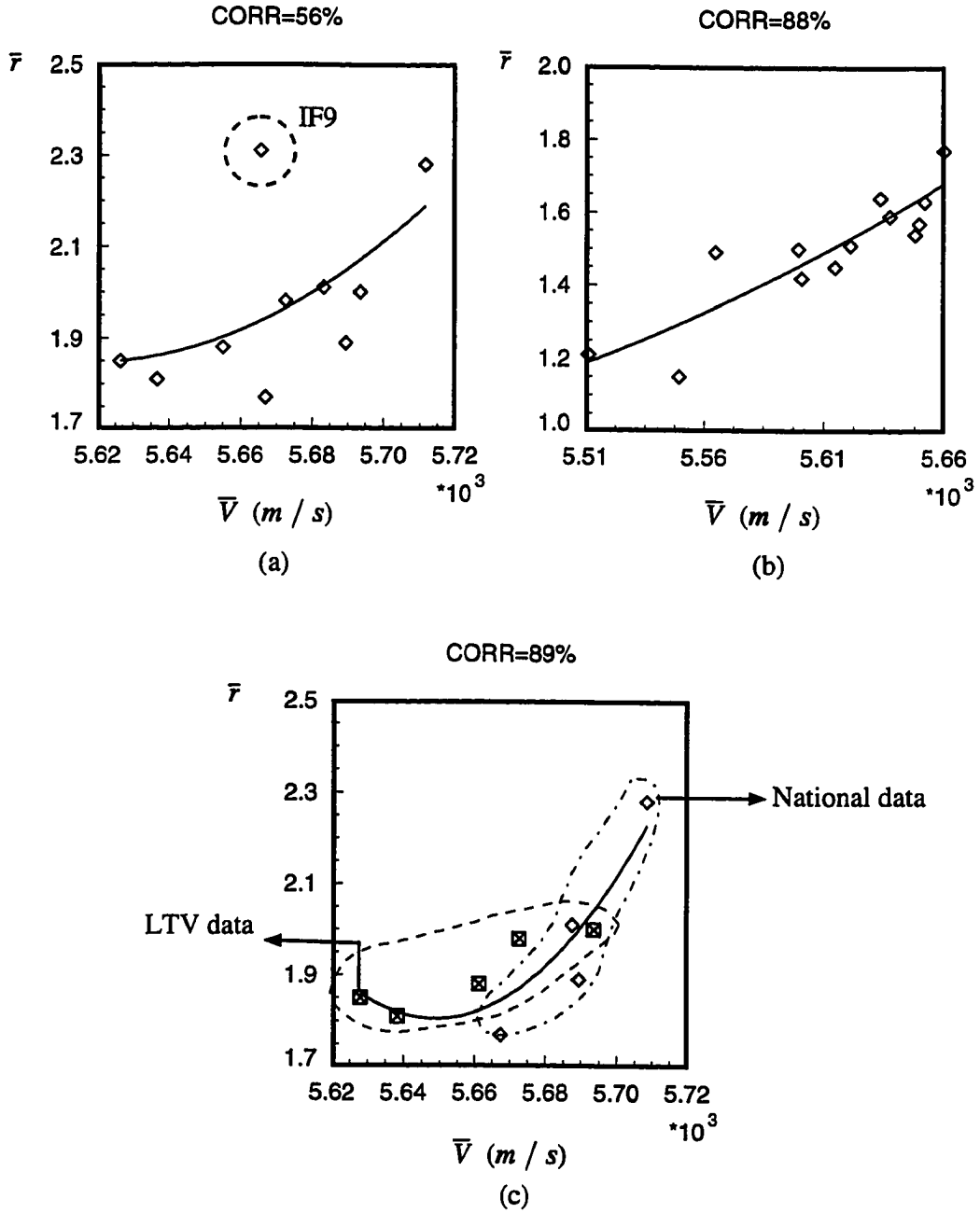


Fig. 5.12 Comparison of data on IF samples and non-IF samples (solid lines are lines of best fit)

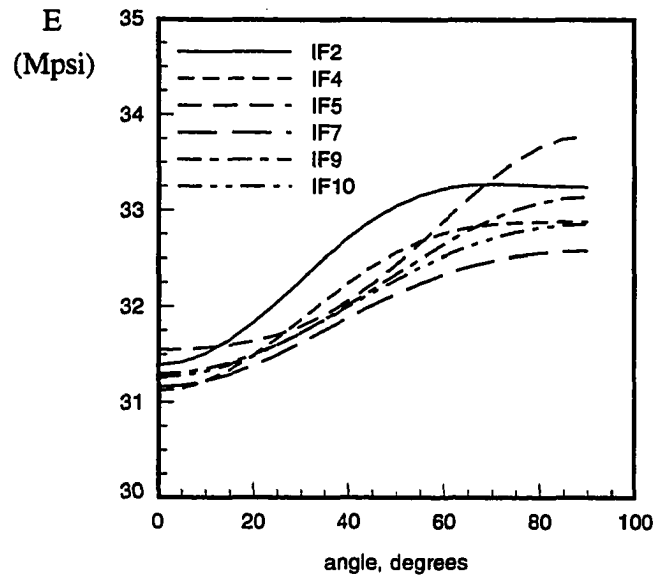
groups shown by the ellipses in Fig. 5.12c. which clearly correspond to the data obtained by the two different companies, LTV and National. Since these two groups fall on the same curve fairly well, it seems that the differences between the manufacturing techniques (employed by these two companies) and which may be thought to contribute to the scatter are minor. In view of the discussions regarding the limitations of tensile tests (Chapter 3, Section 3.1.3), the scatter seen in the IF data is quite possibly due to differences in the tensile test procedures between companies and their corresponding experimental errors. As stated in Chapter 3, at high levels of  $r$ -values (close to and above 2), the tensile measurement of  $r$  approaches its limitations and the magnitude of the error increases significantly. For the IF steels the  $r$ -values are at the higher end of the distribution which increases the probability of having outliers in the data. This may be the reason for the earlier observations reported in 1990 (2).

## **5.8 Data on Elastic Anisotropy**

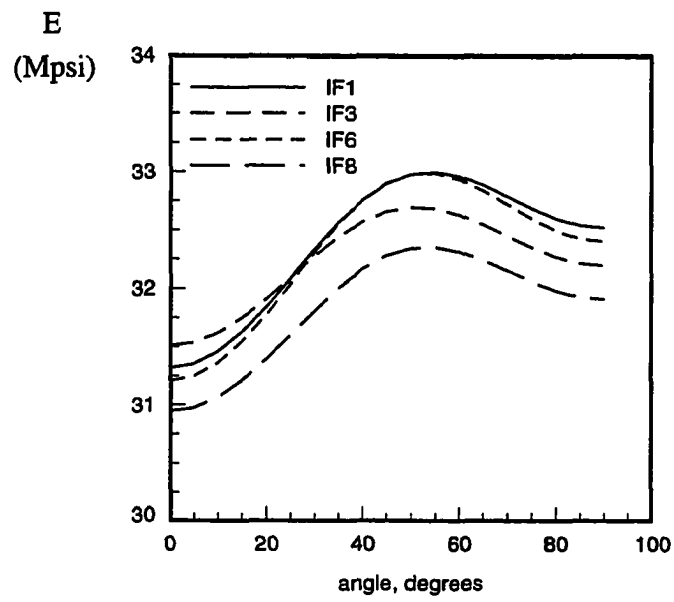
In this section, data on the elastic properties will be presented. This includes the ultrasonic predictions of Young's modulus on the steels studied and the importance of selection of a proper set of single crystal data in these predictions (i.e. single crystal elastic constants). Also, by simulating the angular variation of Young's modulus corresponding to major ideal orientations and comparing them to the experimental data (ultrasonic predictions), useful qualitative information can be obtained regarding the texture of the steel sheets which information will also be presented in this section.

### **5.8.1 Young's Modulus Predictions**

Figures 5.13, 5.14 and 5.15 show the ultrasonic predictions of the angular variation of Young's moduli of the steels studied. These were predicted using Hill's technique following

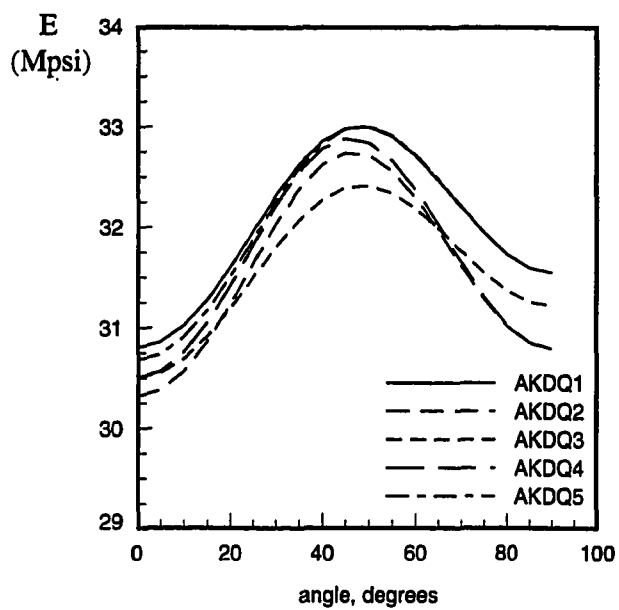


(a)

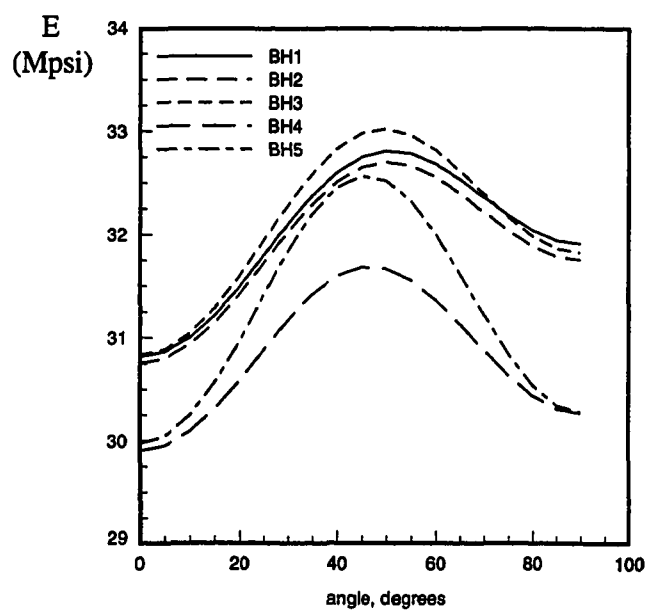


(b)

Fig. 5.13 Ultrasonic predictions of angular variation of Young's modulus for IF steels

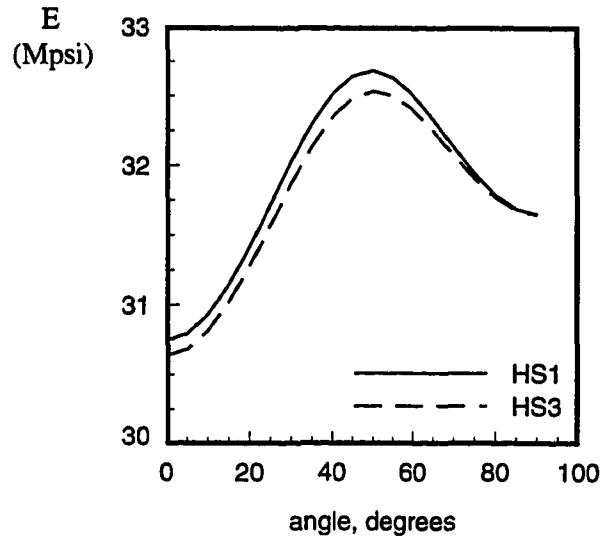


(a)

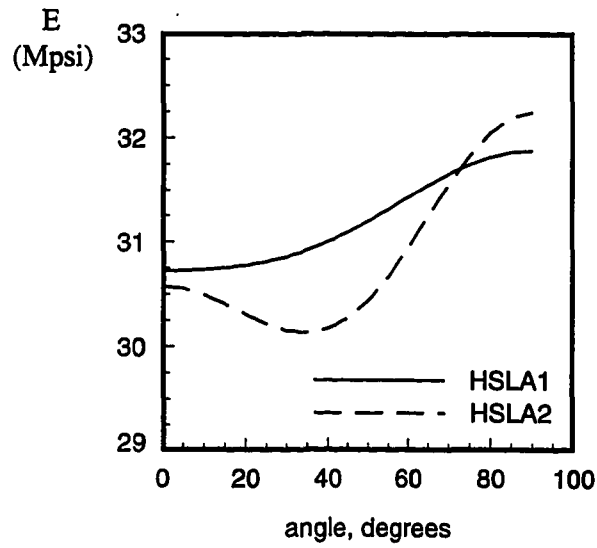


(b)

Fig. 5.14 Ultrasonic predictions of angular variation of Young's modulus for AKDQ and BH steels



(a)



(b)

Fig. 5.15 Ultrasonic predictions of angular variation of Young's modulus for HS and HSLA steels

the discussions presented in Chapter 4 (Section 4.1.2), using Eqn. 4.13. As stated previously, a separate code was written on DEC stations to carry out these calculations which are very similar to the one programmed in Ultra-Form.

Based on the shapes of these plots, two different textures in the IF samples were observed which are loosely grouped and shown in Fig. 5.13a and b. In order to provide a qualitative picture of the main texture components present in these steels, the angular variation of Young's moduli of some of the ideal orientations in low carbon steels were also simulated. These are presented in Fig. 5.16 and Fig. 5.17 for the major orientations of  $\{111\}\langle 110\rangle$ ,  $\{111\}\langle 112\rangle$ ,  $\{100\}\langle 001\rangle$  and  $\{110\}\langle 001\rangle$ , and secondary components of  $\{554\}\langle 225\rangle$ ,  $\{223\}\langle 110\rangle$ ,  $\{332\}\langle 110\rangle$  and  $\{223\}\langle 472\rangle$ . These orientations were selected according to the discussions in Chapter 2 (Section 2.2.3), since these are the ones most commonly observed in drawing grade steels using X-ray and ODF studies. The ideal texture coefficients were simulated using the following relation by Bunge and Esling (56):

$$(5.6) \quad C_{\lambda}^{\mu\nu} = \frac{\exp(-\lambda^2\omega^2/4) - \exp[-(\lambda+1)^2\omega^2/4]}{1 - \exp(-\omega^2/4)} T_{\lambda}^{\mu\nu}$$

where,  $T_{\lambda}^{\mu\nu}$  are the cubic/orthorhombic generalized spherical harmonics and they are tabulated by Bunge in reference (32). In order to give a realistic description of the texture, a Gaussian spread,  $\omega$ , is incorporated into this relation which accounts for the normally occurring misorientation of grains which can take a value between 5 and 20 degrees (56). The smaller this value, the sharper is the texture. Sakata et al. (82) have carried out extensive X-ray studies on deep-drawing grade steels. They determined that a Gaussian spread of 10 degrees is realistic for the common textures of these steels. Therefore, a Gaussian spread of 10

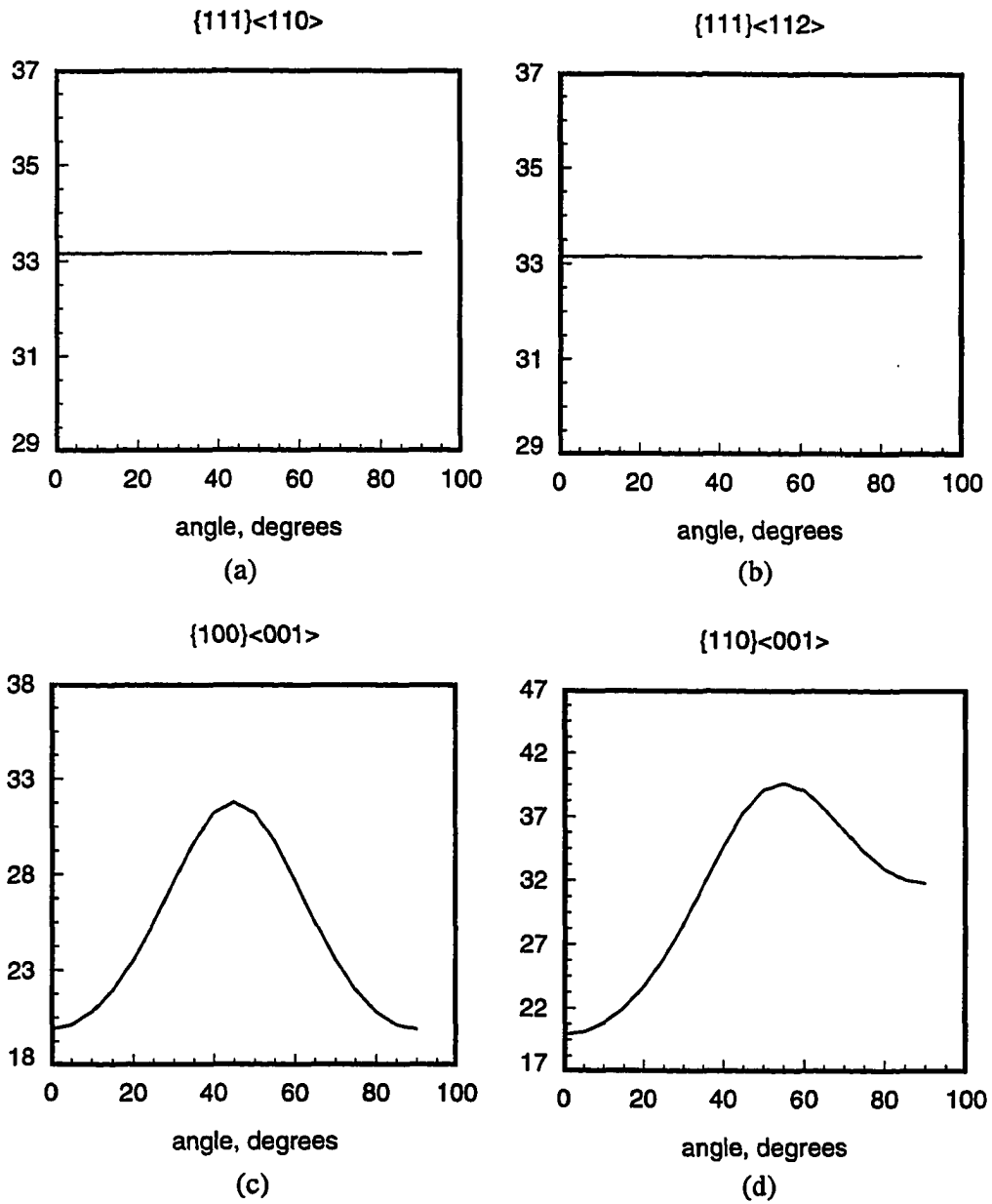


Fig. 5.16 Simulated angular variation of  $E$  (Mpsi) for major ideal orientations

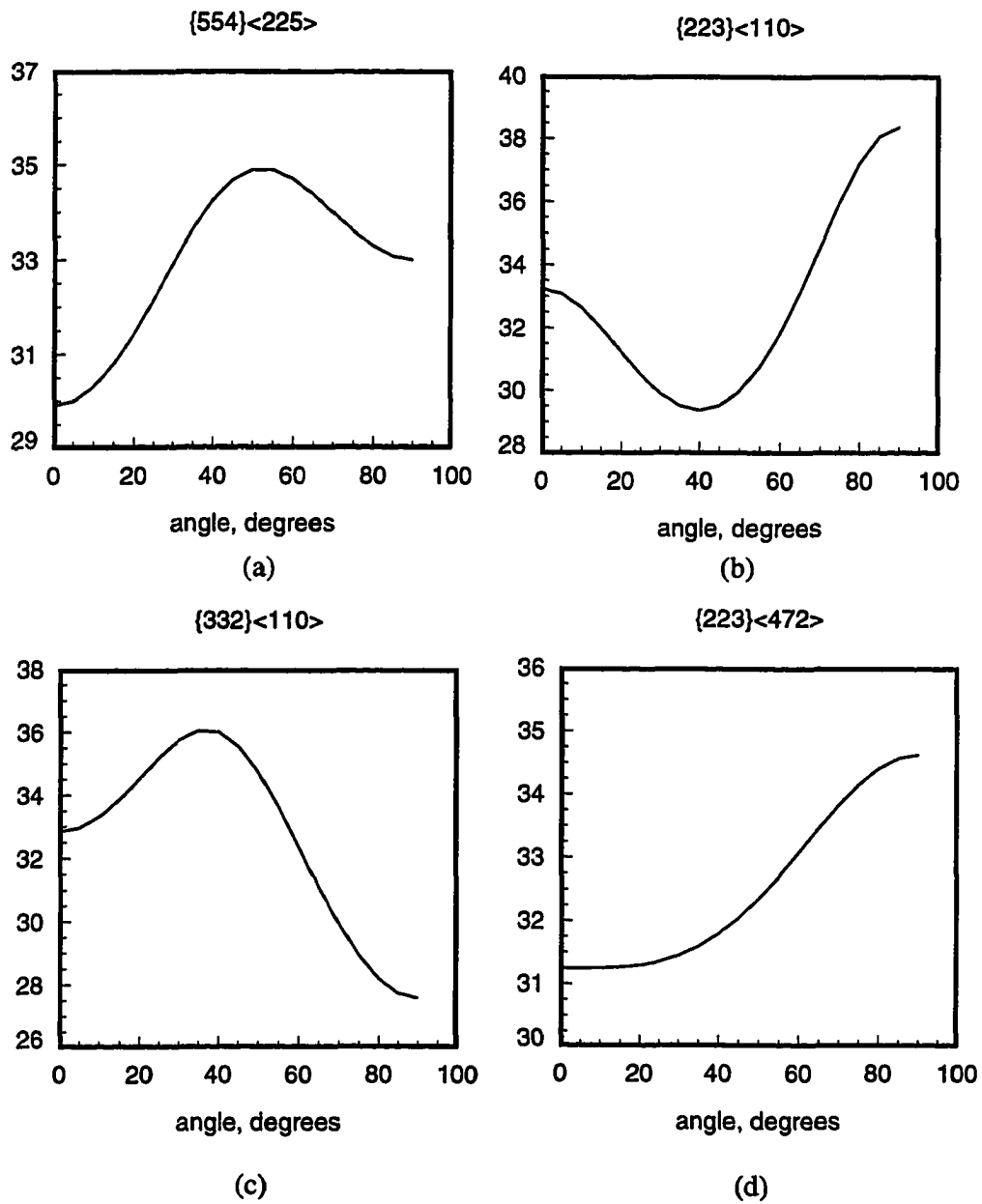


Fig. 5.17 Angular variation of E (Mpsi) of the simulated secondary ideal orientations

degrees was adopted throughout the simulations presented here. Tables 5.7 and 5.8 show the texture coefficients (including order 8th) obtained using Eqn. 5.6 for the ideal orientations selected.

An approximate description of the texture of the steels can be obtained by comparing Figs. 5.16 and 5.17 with Figs. 5.13-15, and an examination of ideal ODC's in Tables. 5.7 and 8. It should be emphasized here that such a qualitative discussion is meaningful only if one keeps in mind that the real textures always consist of a mixture of these ideal orientations. It is only in that light that one can qualitatively approximate the relative contribution of each one of these ideal components to the final texture of the steel. For instance, based on previous data published by various investigators, it is known that a large fraction of grains in AKDQ steels possesses  $\{111\}\langle uvw \rangle$  and  $\{554\}\langle 225 \rangle$  components, and to some extent the  $\{332\}\langle 110 \rangle$  components. Therefore, by combining the planar anisotropies of these components (shown in Figs. 5.16a and b, and 5.17a and c) and comparing them with the ultrasonic predictions, one can reasonably explain these results.

Keeping the above discussion in mind, investigation of the ideal textures shown in figures 5.16 and 5.17 and ODC's in Tables. 5.7 and 8, reveals that the level of the normal elastic anisotropy (i.e.  $\bar{E}$ ) is mostly set by  $C_4^{11}$  terms, where the planar elastic anisotropy is influenced by the non-zero  $C_4^{12}$  and  $C_4^{13}$  terms of the secondary components shown in Table 5.8 and Fig. 5.17 (This is particularly true for steels which show a strong intensity of  $\{111\}\langle uvw \rangle$  components in their textures). It appears that the texture in the IF steels shown in Fig. 5.13a (IF2, 4,5,7,9 and 10) are influenced heavily by the secondary components of  $\{223\}\langle 472 \rangle$ , while the ones shown in Fig. 5.13b (IF1, 3, 6 and 8) may have been influenced more by  $\{554\}\langle 224 \rangle$  components. This observation is consistent with the discussions presented in Chapter 2 (Section 2.2.3) and data reported by Daniel and Jonas (61) which they obtained by detailed ODF analysis. Of interest here is the angular variation of Young's

Table 5.7 ODC's for major ideal texture components

$C_{\lambda}^{\mu\nu}$	{111}<110>	{111}<112>	{100}<001>	{110}<001>
$C_4^{11}$	-3.94	-3.94	5.90	-1.48
$C_4^{12}$	0.00	0.00	0.00	-6.60
$C_4^{13}$	0.00	0.00	4.99	3.74
$C_6^{11}$	-5.94	-5.94	-3.34	5.43
$C_6^{12}$	0.00	0.00	0.00	-3.02
$C_6^{13}$	0.00	0.00	8.83	-5.52
$C_6^{14}$	5.32	-5.32	0.00	-4.48
$C_8^{11}$	2.10	2.10	7.06	3.97
$C_8^{12}$	0.00	0.00	0.00	2.46
$C_8^{13}$	0.00	0.00	3.75	5.86
$C_8^{14}$	-7.43	7.43	0.00	-5.48
$C_8^{15}$	0.00	0.00	5.72	3.21

Table 5.8 ODC's for secondary ideal texture components

$C_{\lambda}^{\mu\nu}$	{554}<225>	{223}<110>	{332}<110>	{223}<472>
$C_4^{11}$	-3.75	-3.08	-3.42	-3.08
$C_4^{12}$	-1.36	-1.82	2.45	-1.37
$C_4^{13}$	0.94	-1.81	1.59	-0.25
$C_6^{11}$	-5.28	-3.96	-3.99	-3.97
$C_6^{12}$	1.04	4.03	-1.12	3.04
$C_6^{13}$	-1.45	1.93	-2.50	0.26
$C_6^{14}$	-5.24	4.93	5.12	-2.71
$C_8^{11}$	1.82	0.15	1.57	0.15
$C_8^{12}$	2.54	2.61	-4.06	1.97
$C_8^{13}$	-1.77	4.97	-2.05	0.68
$C_8^{14}$	6.71	-5.32	-5.30	2.92
$C_8^{15}$	0.20	0.75	0.59	-0.73

modulus in IF5 (Fig. 5.13a) which is almost entirely identical to the Young's modulus of the ideal orientation  $\{223\}\langle 472\rangle$  (Fig. 5.17b). These orientations are responsible for the larger anisotropy that is seen in the rolling plane of the IF samples (e.g. see  $\delta r$  in Table 5.1).

Examination of Fig. 5.14a and b reveals that the AKDQ and BH steels have essentially similar textures which are influenced by  $\{554\}\langle 225\rangle$  and  $\{332\}\langle 110\rangle$ , responsible for the smaller anisotropy (almost isotropic) which is seen in their rolling plane. Similar deductions can be made with regard to the HS and HSLA steels (Fig. 5.15a and b). The level of the normal elastic anisotropy in the latter, however, seems to have been degraded by the presence of the  $\{100\}$  components which are commonly seen in HSLA steels.

### 5.8.2 Effects of Single Crystal Data

As is evident from the discussions in Chapter 4, use of the series expansion technique in the calculation of Young's moduli of polycrystals is a function of the properties of the single crystal's elastic constants (Eqn. 4.13). The relations between the velocity of the ultrasonic pulses and the texture coefficients of the polycrystal are also function of these properties (Eqn. 4.19). Therefore, an accurate prediction of macroscopic properties using the anisotropy of ultrasonic Lamb waves is dependent on accurate estimates of the single crystal data.

The elastic constants of iron have been obtained experimentally by several investigators whose findings have been collected and reported by Ledbetter (70). The standard deviation on the mean of these constants is however large (i.e.  $c_{11}=229\pm 9$ ,  $c_{12}=134\pm 9$  and  $c_{44}=115\pm 3$  GPa). These uncertainties are due to differences in the experimental procedures and the chemical compositions of the single crystals of iron that were used by these various investigators. Table 5.9 shows a subset of these constants (7 groups) where the chemical compositions of the corresponding single crystals were similar to the ones in commercially

produced low carbon steels as listed in reference (70). The standard deviations associated with the mean of the subset data are the following:  $c_{11}=230\pm 5$ ,  $c_{12}=136\pm 5$  and  $c_{44}=116.5\pm 2.5$  GPa. Table 5.10 shows the results of a propagation of error analysis predicting the uncertainties associated with ultrasonic prediction of texture coefficients (Eqn. 4.19) using the errors of the subset presented in Table 5.9.

Table 5.9 Various sets of elastic constants reported in reference (70)

Investigator	$c_{11}$	$c_{12}$	$c_{44}$
1. Moller, Brasse	228	140	112
2. Leese, Lord	226	140	116
3. Lord, Bershers	228	132	116.5
4. Guinan, Beshers	230.1	134.6	116.7
5. Goens, Schmid	237	141	116
6. Rayne	233.1	135.4	117.8
7. Yamamoto	234	135	117.6

Table 5.10 Error in texture coefficients due to uncertainties in Table 5.9

Texture Coefficient	$\pm$ Error
$W_{400}$	$1.79 \times 10^{-3}$
$W_{440}$	$1.63 \times 10^{-4}$
$W_{420}$	$5.48 \times 10^{-5}$

These results indicate that of the three texture coefficients,  $W_{400}$  is the one most susceptible to uncertainties in the elastic constants and  $W_{440}$  is next with less sensitivity, and  $W_{420}$  is the least susceptible texture parameter. Since  $W_{400}$  represents the normal anisotropy in rolled sheets, large uncertainties in this texture coefficient can affect ultrasonic predictions of  $\bar{E}$  and  $\bar{\nu}$  significantly. This is consistent with the observations by Thompson et al. (37), in which larger errors were observed in their ultrasonically predicted  $W_{400}$  values than the other two coefficients in copper samples.

In order to investigate the effects of variations of elastic constants on Young's modulus, use of the ideal texture coefficients may provide insight. The reason for this supposition is that calculation of Young's modulus by the ultrasonic technique (Eqn. 4.19) is dependent on the texture coefficients which in turn are function of the elastic constants. Therefore, by fixing the texture coefficients using ideal ODC's, an independent check on the effects of elastic constants on Young's modulus can be obtained. Figure 5.18a shows the results of these effects on Young's modulus of the ideal orientation,  $\{554\}\langle 225 \rangle$ . It is evident that varying the constants from set 1 to 7, increases the level of normal anisotropy by approximately 5% ( $\sim \pm 2.5\%$  from the mean which is shown by the dotted line in the figure). The shapes of the plots do not change which indicates that the planar anisotropy is insensitive to these errors. This is consistent with the propagation of error results shown in Table 5.10 where  $W_{440}$  shows less sensitivity. It is difficult to establish the relative weight of the individual elastic moduli in forming the trend shown in the figure, although,  $c_{11}$  may weigh more heavily than the other two in contributing to these trends. Figure 5.18b shows the variation of the Young's modulus (obtained ultrasonically) on AKDQ1 for the two sets 1 and 7. Although the actual data show the same trend as that seen in Fig. 5.18a, the increase is less,  $\sim 2.5\%$ . This is due to the interdependence of Young's modulus and texture coefficients in Eqn. 4.19, where the increase in Young's modulus is offset by a larger increase in  $W_{400}$ .

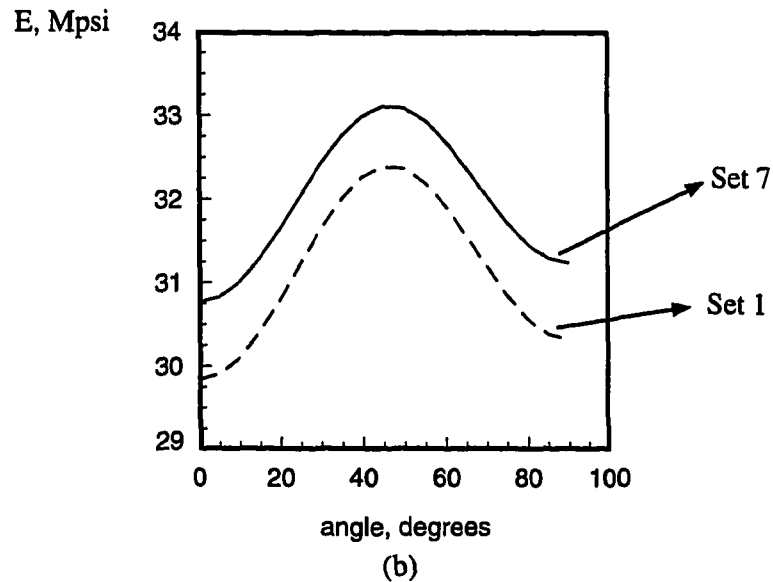
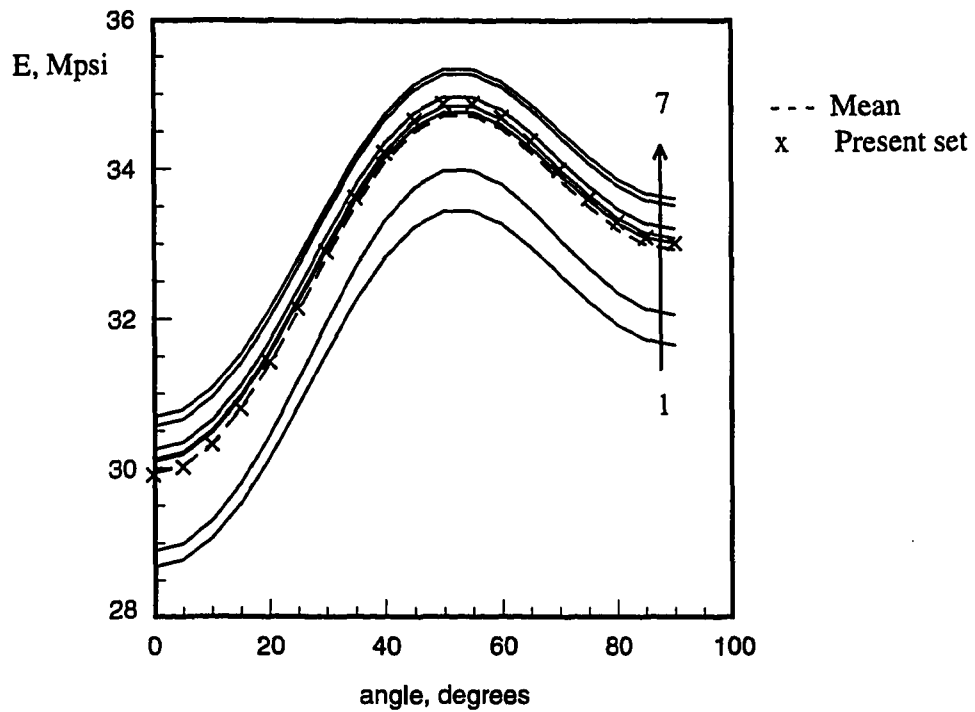


Fig. 5.18 Effects of variations in elastic constants on Young's modulus predictions:  
 (a) On Young's modulus of  $\{554\}\langle 225\rangle$  orientation  
 (b) On Young's modulus of AKDQ1

Figure 5.19 shows the variation seen in the ultrasonically predicted values of  $W_{400}$  and  $\bar{r}$  on AKDQ1-5 samples (Eqn. 4.19 and Mould and Johnson correlation, respectively). It is clear that the change in  $\bar{r}$  closely parallels that of  $W_{400}$  and is quite significant from set 1 to 7. This change, shown in Table 5.11, can be as much as 0.54.

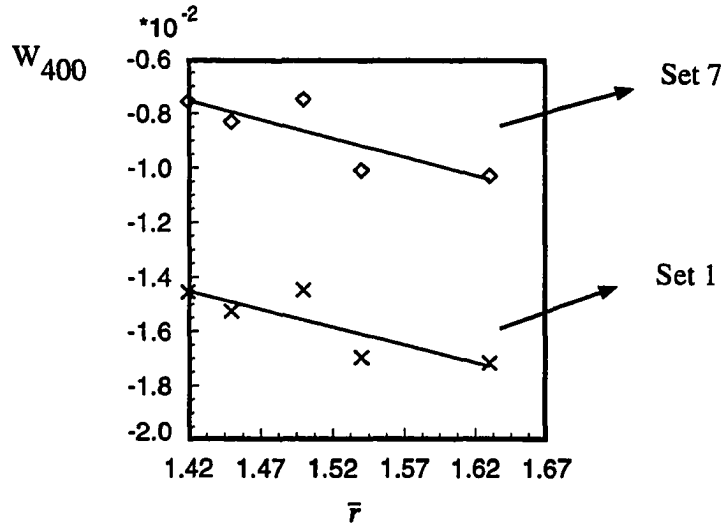


Fig. 5.19 Effects of variations in elastic constants on  $\bar{r} - W_{400}$  plots for AKDQ 1-5

Table 5.11 Variations in  $\bar{r}$  due to variations in elastic constants

Tensile $\bar{r}$	Ultrasonic $\bar{r}$ (Mould-Johnson) Set 7	Ultrasonic $\bar{r}$ (Mould-Johnson) Set 1
1.63	1.95	1.41
1.42	1.64	1.19
1.50	1.63	1.18
1.45	1.72	1.25
1.54	1.93	1.39

Figure 5.20a and b show that the change in  $\Delta r$  and  $\delta r$  closely parallel those of  $W_{440}$  and  $W_{420}$  but that they are not as significant as the variation in  $W_{400}$  (which is expected).

From the above discussion, it is evident that a proper choice of elastic constants is vital to accurate ultrasonic predictions of sheet properties which reflect the degree of normal anisotropy. The difficulty in selecting the proper value lies in the fact that the chemical composition and microcleanliness of the steels change significantly from grade to grade, and ideally, each grade of steel requires a separate set of elastic constants representative of its own particular chemical composition. However, it is possible to, in effect, 'calibrate' the steels so that one set of elastic constants can be used on all grades with reasonable accuracy. This was done by Daniel and Jonas (61) who used the Modul-r instrument as an independent way of measuring Young's modulus. These authors used the X-ray technique to obtain texture coefficients which they used to calculate the Young's moduli of their steel samples by means of Bunge's elastic energy technique (61). Through an iterative procedure, within the reported range of uncertainties reported in reference (70), they changed the elastic constants until their calculated moduli became the same as their magnetostrictively measured ones (by Modul-r instrument). Since the grades and chemical compositions of the steels that they studied closely resembled the steels used in this study, their set, which is  $c_{11}=233$ ,  $c_{12}=141$  and  $c_{44}=117.5$  GPa (shown by crosses in Fig. 5.18a), was adopted throughout all the calculations in this work. Figure 5.21a shows the comparison of the ultrasonically measured  $W_{400}$  values on some of the steels used in the present work with the ones obtained by neutron diffraction. It is evident that an excellent agreement exists between the  $W_{400}$  values obtained with the present set of elastic constants and the diffraction data which pertains to the fact that this set is representative of the chemical compositions of the steels studied here. Similar agreements are seen for the other two coefficients shown in Fig. 5.21b and c.

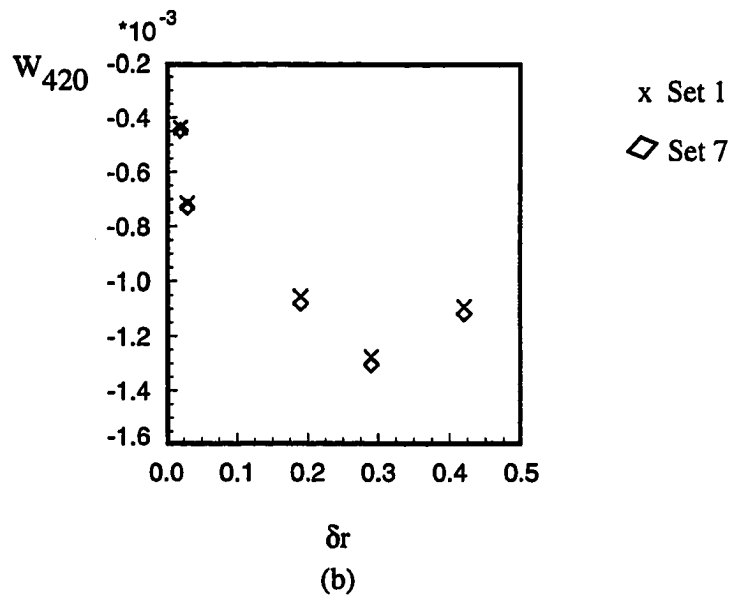
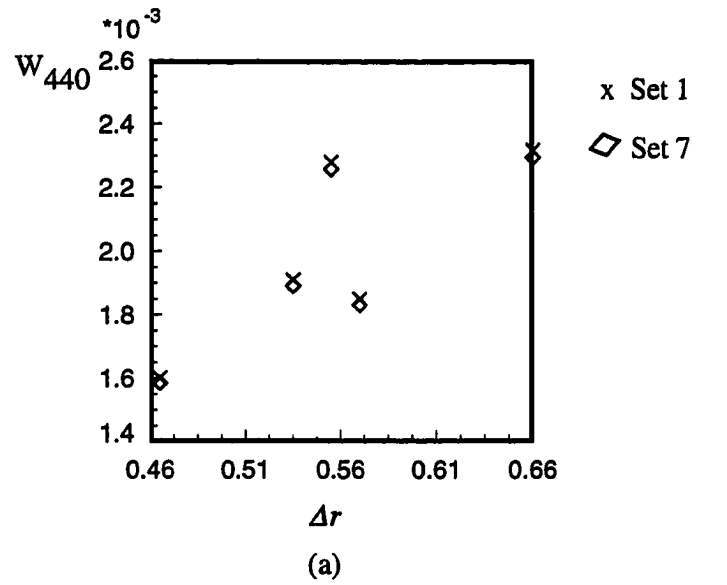
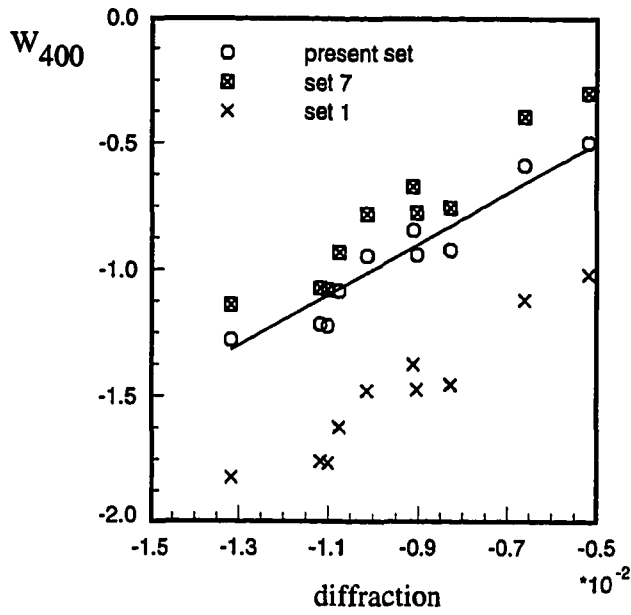


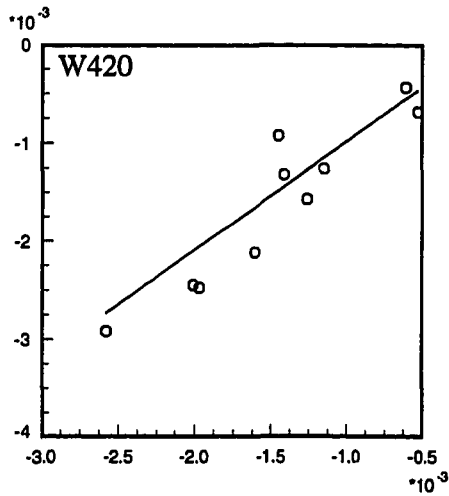
Fig. 5.20 Effects of variations in elastic constants on:

(a)  $\Delta r - W_{440}$

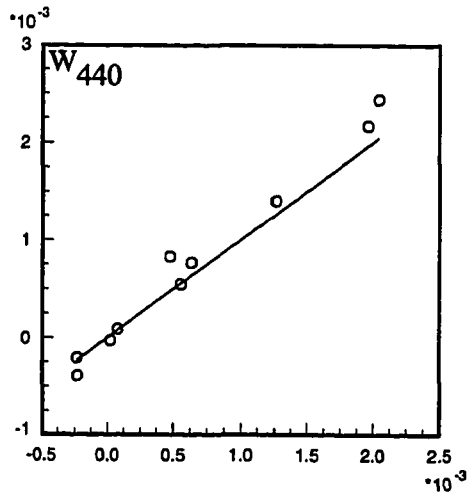
(b)  $\delta r - W_{420}$



(a)



(b)



(c)

Fig. 5.21 Agreement between diffraction and ultrasonics on texture coefficients:

(a)  $W_{400}$     (b)  $W_{440}$     (c)  $W_{420}$

## 5.9 Data On Plastic Anisotropy

In this section data regarding predictions of plastic properties will be presented. These include predictions of r-values by ultrasonic and diffraction techniques. They will also be compared with tensile measurement results. Also, as with the discussions of the elastic anisotropy in the previous sections, the angular variations of r-values corresponding to the ideal orientations are also presented which when compared to the experimental data, provide a reasonable description of the texture of the steels used here. Moreover, using ideal ODC's, the effects of early truncation of 6th order texture coefficients on convergence of the series expansion technique are simulated. The results of these simulations will then be compared to the actual experimental evidence which is obtained from the neutron diffraction technique using 4th order alone, and 4th order and 6th order terms included. The RC model was used throughout all the r-value calculations using data from ultrasonic and diffraction techniques. Finally, certain data and matters regarding the relative weights of the  $W_{6mn}$  coefficients in prediction of r-values will be discussed. Before proceeding to present the data, however, it may be useful to discuss some aspects of the relaxed constraint model (RC model) which are important with regard to its accuracy and capabilities.

### 5.9.1 The RC Model

**5.9.1.1 Location of Minimum in M-q Plot** Calculation of r-values by the RC model is carried out by finding the appropriate strain state (i.e., contraction ratio, q) where the average Taylor factor,  $\bar{M}$  is a minimum. This is the generalization of the Taylor's principle of minimum plastic work in a polycrystal. The calculation involves two stages, one of identifying the functional relationship between this factor and the contraction ratio, q, and the other of locating the minimum. Figure 5.22 shows three plots of  $\bar{M}$  vs q for the three directions of 0, 45 and 90 degrees in a BH1 sample. The relationship between  $\bar{M}$  and q is obtained by a

polynomial regression. Location of the minimum is a critical step, since as Bunge (32) points out, this part of the curve is relatively flat and, therefore, the accuracy in calculation of  $r$  becomes a function of the accuracy of finding the minimum in the plot. Particular care was taken in this work to increase the accuracy of the regression fitting and to locate the minimum contraction ratio. Using NAG routines E02ADF, E02AEF and E04ABF, Chebyshev-series polynomials of power 10 were used to fit the experimental data and to locate the minimum.

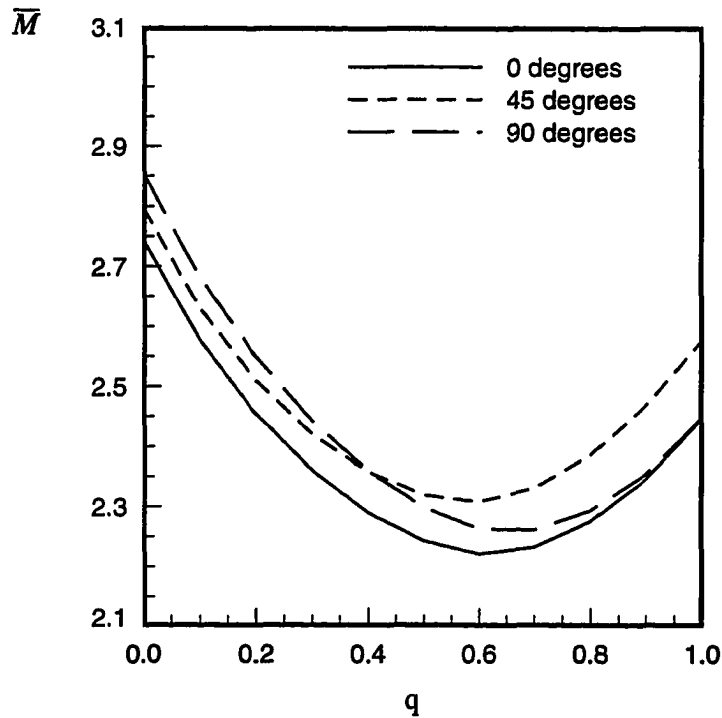


Fig. 5.22 Plots of average Taylor factor vs the contraction ratio for sample BH1

In addition to  $r$ -values, another plastic property of interest may be obtained easily by this model. This is the angular variation of flow stress, or yield stress in the plane of the sheet, normalized with respect to the critically resolved shear stress:  $\sigma(\alpha)/\tau$ . This parameter (Eqn. 4.29), is essentially equal to the average Taylor factor of the polycrystal,  $\bar{M}$  (weighted by the texture coefficients). Figure 5.23 shows the angular variations of normalized yield strengths of the two samples, BH5 and IF5. The trend in data is quite consistent with the variation of measured values of yield strengths obtained in these samples by using tensile tests (e.g. yield strength of BH5 varies from 32.1 ksi at 0 and 90 degrees to 33.7 ksi at 45 degrees).

**5.9.1.2 Choice of CR Factor in RC Model** As discussed in Chapter 4, the glide in bcc crystals can occur on  $\{110\}$  and/or  $\{112\}$  planes. For pure iron crystals, the two glide planes exhibit an equal share of slip, with the critically resolved shear stress ratio,  $CR_1$  (herein called CR) being experimentally determined to be approximately 1 (76). Examination of Table 4.1 shows that the presence of impurities or interstitials lowers this ratio to less than 1. This means that interstitials make glide more difficult on  $\{110\}$  planes. The RC model takes this fact into account and has three CR ratios of 0.9, 0.95 and 1. Daniel and Jonas (61), experimentally determined that CR factors of 0.95 and 1 obtain better fits between their predicted  $r$ -values and the tensile measurements for high  $r$ -value steels such as IF steels, and 0.9 for AKDQ and other non-IF steels which show lower  $r$ -values. They reasoned that this is also consistent with the fact that IF steels have lower interstitials than the others and hence a higher CR is necessary for these steels. Experimental evidence obtained in this study seems to confirm their findings.

Figure 5.24 shows the variation of  $\bar{r}$  as measured by the tensile test, and the percent weight of the carbon of the steels studied here. It can be seen that, despite the scatter, there is a strong relationship between  $\bar{r}$  and the carbon contents of the steels. The correlation coefficient is 83% (1% significance level is 52.6%). The steels with less than 0.01% carbon

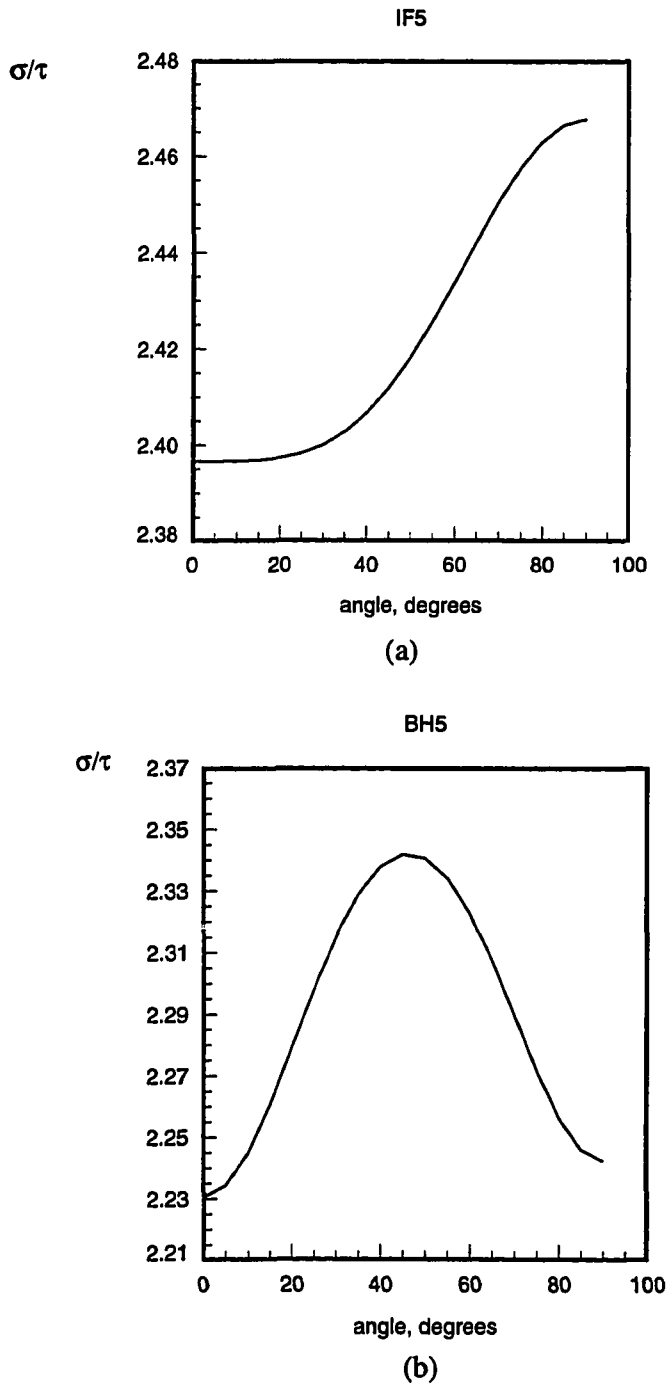


Fig. 5.23 Angular variation of normalized yield strength for (a) IF5 and (b) BH5

content show high values of  $\bar{r}$  (see Table 5.1) and steels with more carbon show smaller  $\bar{r}$ . Therefore, in a manner similar to the effects of single crystal elastic constants on Young's modulus, the normal anisotropy as indicated by  $\bar{r}$  is strongly influenced by the presence of interstitials such as carbon.

Figure 5.25 shows the effects of the three CR factors on the ultrasonic predictions of  $r$ -values for sample AKDQ3. It is evident that the planar anisotropy is unaffected by change in CR (the shape of the curve is unaffected), while normal anisotropy is changed systematically which is consistent with the observation in Fig. 5.24 (average  $r$  decreases with decreasing carbon content). The impact of changing CR from 0.9-1 is an increase of approximately 0.2 in  $\bar{r}$ , while change from 0.9-0.95 results in an increase of 0.1 in  $\bar{r}$ .

Based on these observations and the ones reported in reference (61), the following CR factors were used in this work: Values of CR of 1 and 0.95 were used for steels with carbon contents of less than 0.01% (IF steels), and CR values of 0.9 for all other non-IF steels. The Taylor factors corresponding to these CR factors are tabulated in Reference (60) which were used in this work.

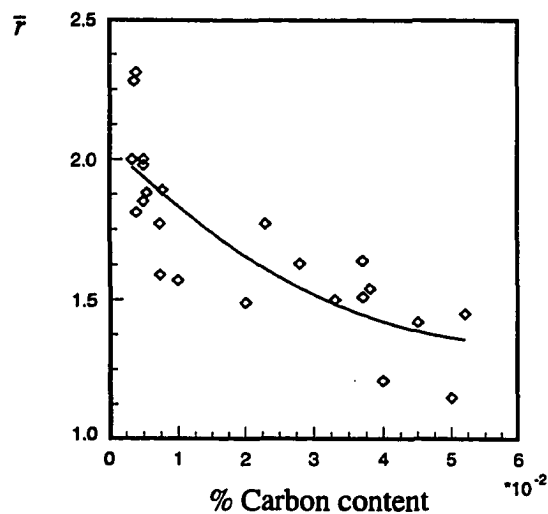


Fig. 5.24 Variation of  $\bar{r}$  with %carbon content in steels studied

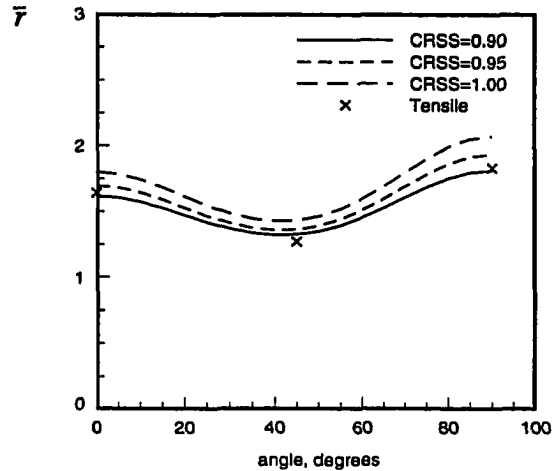
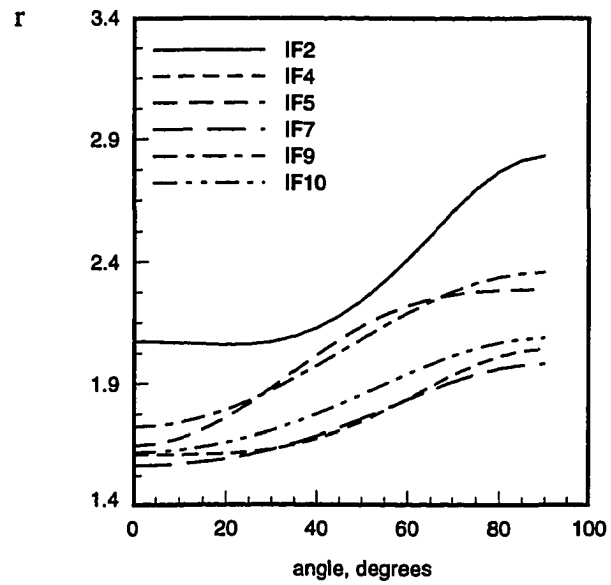


Fig. 5.25 Effects of CR factor on predictions of normal anisotropy

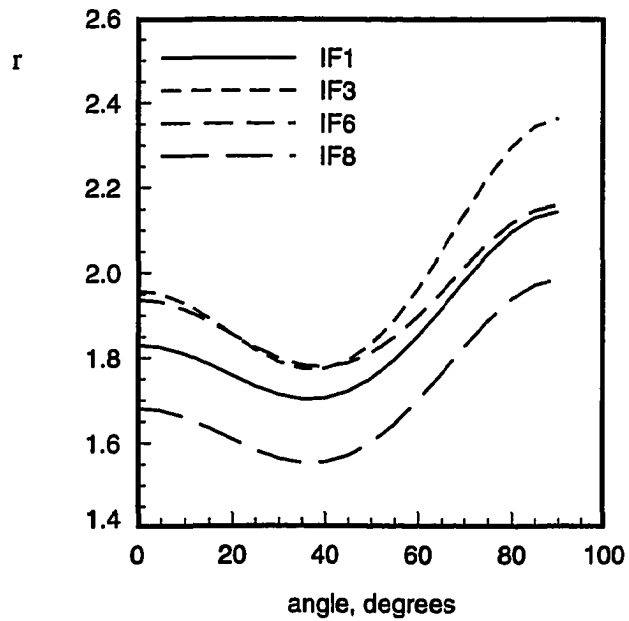
### 5.9.2 r-value Predictions and Ideal Orientations

Figures 5.26-28 show the ultrasonic predictions of the angular variations of the r-values in the steels studied. It can be seen that the shape of these variations is exactly opposite to the ones predicted for the angular variations of the Young's moduli of the identical samples which are shown in Figs. 5.13-15 (e.g. The shape of planar anisotropy is 'U' for AKDQ, BH and HS steels, where the elastic anisotropy for the same steels was bell shaped). Nevertheless, the two types of IF samples which were loosely grouped in Fig. 5.13, (based on the ultrasonic prediction of their elastic anisotropy) can be grouped here as well, this time based on the shape of their plastic anisotropy. This is due to the fact the same texture components have contributed to the elastic and plastic properties of these steels.

Table 5.12 shows the predicted plastic properties of ideal orientations using the RC



(a)



(b)

Fig 5.26 Angular variation of r-values in IF steels, predicted ultrasonically

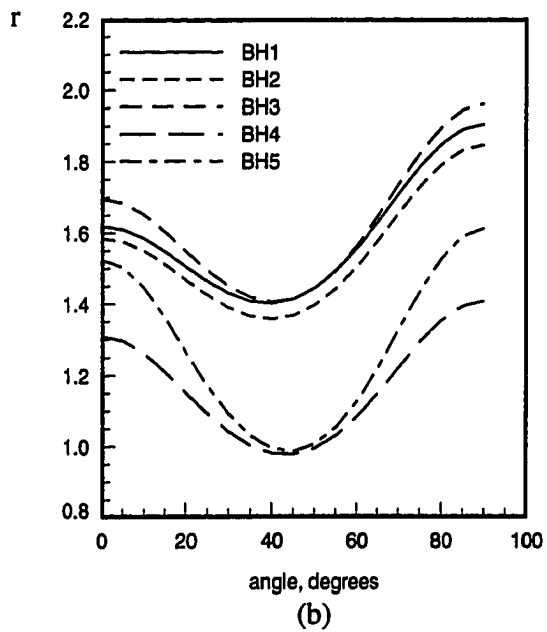
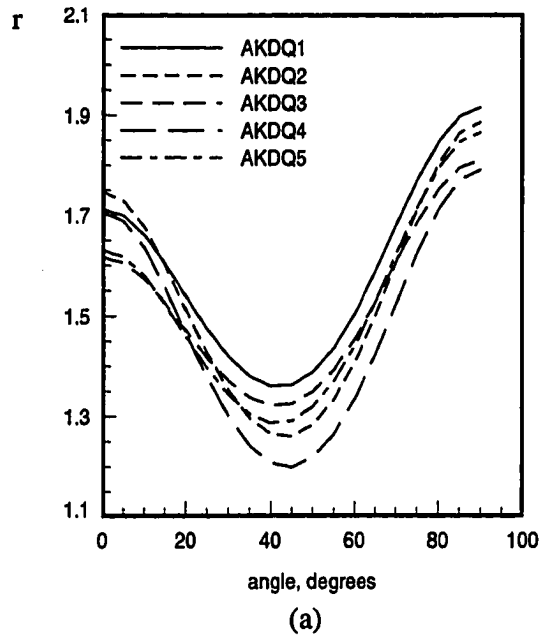
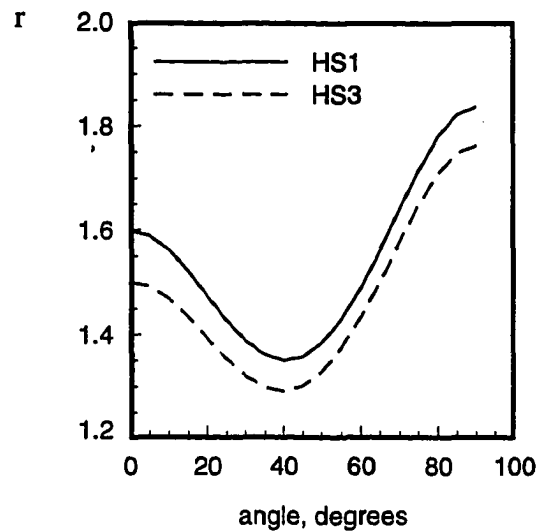
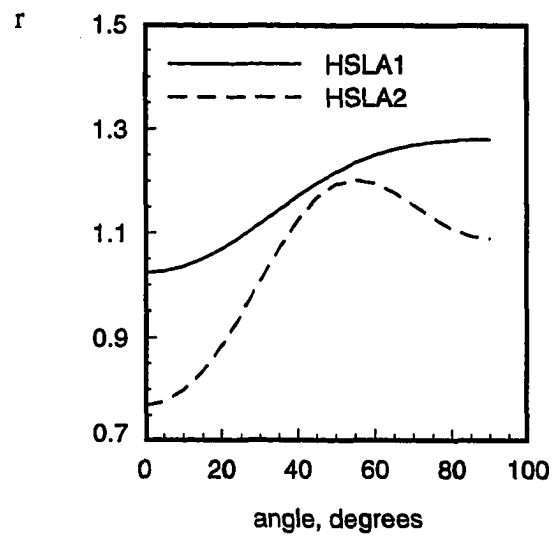


Fig 5.27 Angular variation of r-values, predicted ultrasonically in  
(a) AKDQ steels  
(b) BH steels



(a)



(b)

Fig 5.28 Angular variation of r-values, predicted ultrasonically in

(a) HS steels

(b) HSLA steels

model. Examination of Table 5.12 reveals that the  $\{111\}$  components ( $110$  and  $112$  directions) show high  $\bar{r}$  with negligible  $\Delta r$  which suggests that these components mostly set the level of normal anisotropy in low carbon steels. The planar anisotropy must, therefore, be influenced mostly by the secondary components ( $\{554\}$ ,  $\{223\}$ ,  $\{332\}$ , etc.) external to the  $\gamma$  fiber, discussed in Chapter 2. This is consistent with the results reported in the literature where  $\{111\}\langle uvw \rangle$  components show high X-ray intensities which correlate well with  $\bar{r}$ . The  $\{100\}\langle uvw \rangle$  components show a deleterious effects on drawability which again is quite consistent with the reported results in previous studies. The Goss component ( $\{110\}\langle uvw \rangle$ ) shows a very high  $\delta r$  which is due to its high  $r$ -values at 90 degrees. Because of the high planar anisotropy due to this texture component, its presence is not desirable in low carbon steels of deep drawing quality.

Table 5.12 Properties of simulated ideal orientations, using RC model

Texture component	$\bar{r}$	$\Delta r$	$\delta r$
$\{111\}\langle 110 \rangle$	2.76	0.007	0.70
$\{111\}\langle 112 \rangle$	2.76	0.007	-0.70
$\{100\}\langle 001 \rangle$	0.40	0.74	-1.29
$\{110\}\langle 001 \rangle$	3.27	5.31	11.66
$\{554\}\langle 225 \rangle$	2.86	1.72	0.99
$\{223\}\langle 110 \rangle$	3.18	-3.08	1.37
$\{332\}\langle 110 \rangle$	3.12	3.07	-3.01
$\{223\}\langle 472 \rangle$	2.36	-0.20	1.28

Further examination of Table 5.12 shows that the components  $\{223\}$  ( $\langle 472 \rangle$  and  $\langle 110 \rangle$ ) and  $\{554\}\langle 225 \rangle$  which are found in IF steels are responsible for large positive  $\delta r$ 's (as seen in all the IF steels particularly IF2, 5, 6, and 9) and small  $\Delta r$  in the IF steels studied here (particularly IF5, 9 and 10). Figures 5.29 and 5.30 show the shape of the angular variation of  $r$ -values corresponding to the ideal orientations. On examining the shape of the planar anisotropy in Fig. 5.30a, c and d, and comparing them to the ultrasonically predicted ones (Fig. 5.26a and b) strong similarities are obvious and this confirms the conclusions drawn by similar examinations of the elastic anisotropies in these steels which were discussed in Section 5.8.1.

The texture components  $\{554\}\langle 225 \rangle$  and  $\{332\}\langle 110 \rangle$  which are exhibited in AKDQ steels are responsible for the planar anisotropy that is observed in these steels ( $\Delta r \sim 0.5$ , see Table 5.2) and the small  $\delta r$ 's ( $\{332\}$  components have negative  $\delta r$ , and thus contribute to the small anisotropy in the rolling planes of these steels, particularly AKDQ2-5). The 'U' shape that is observed in their planar anisotropy which is confirmed by the tensile measurements (see Fig. 5.25), is due to the presence of these components and probably a mixture of  $\{111\}\langle 110 \rangle$  and  $\{111\}\langle 112 \rangle$  components. BH and HS steels show similar trends (with higher  $\delta r$ 's). This is true since these steels are essentially the same as the AKDQ steels (particularly BH steels). HSLA steels show almost isotropic trends with small planar anisotropy and  $\delta r$ 's which are due to the strength of the  $\{100\}$  components in their textures.

### 5.9.3 The effects of Higher ODC's in the Prediction of $r$ -values

As stated in Chapter 2, Section 2.2.3, some of the deep drawing grade steels may show 6-fold symmetry in their plastic properties. These include IF steels which, due to their particular processing practices (heavy hot and cold reductions), have sharper textures than the rest of the steels (i.e. they show higher X-ray intensities). This means a higher intensity in

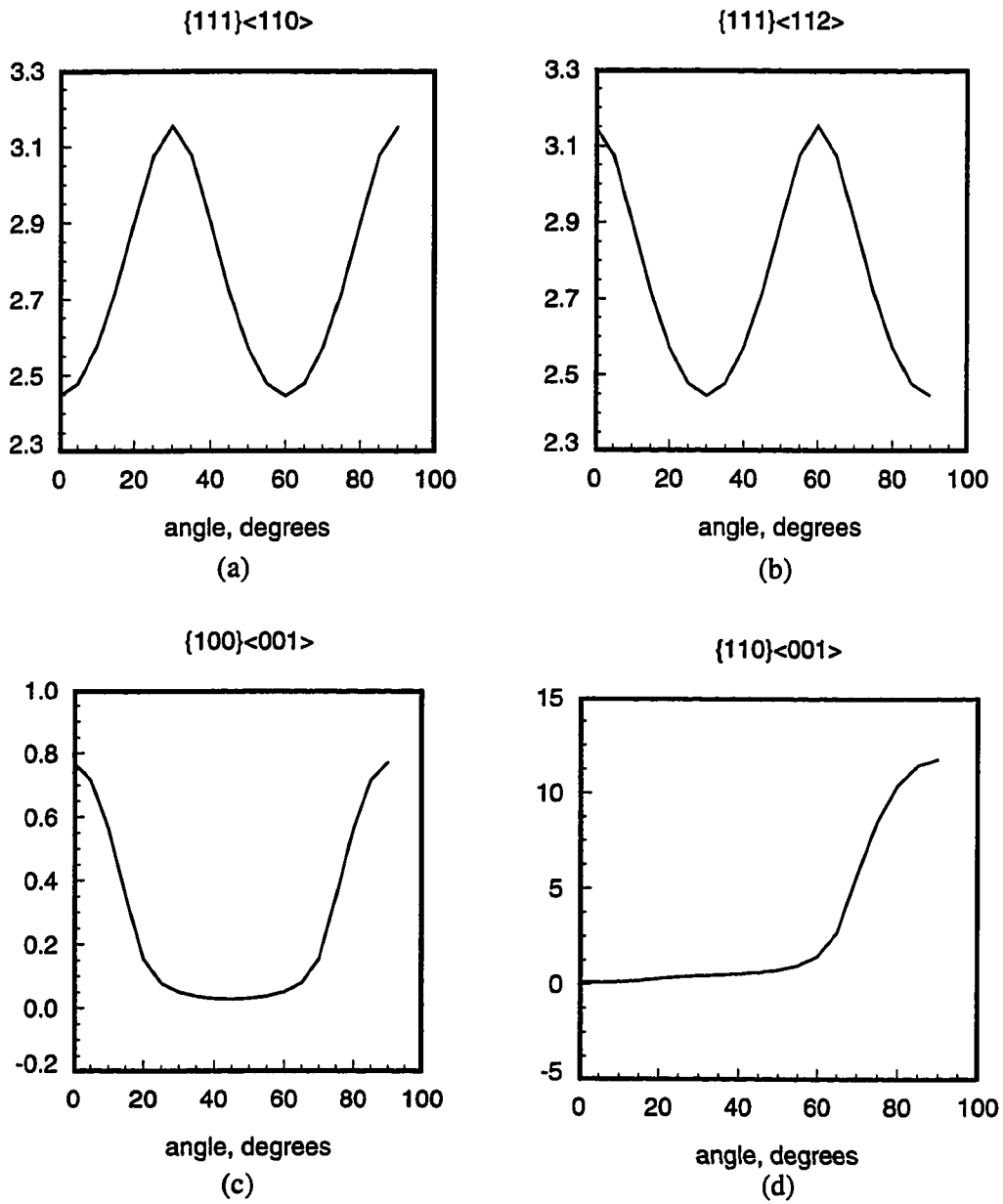


Fig. 5.29 Angular variation of  $r$ -values for simulated ideal major orientations

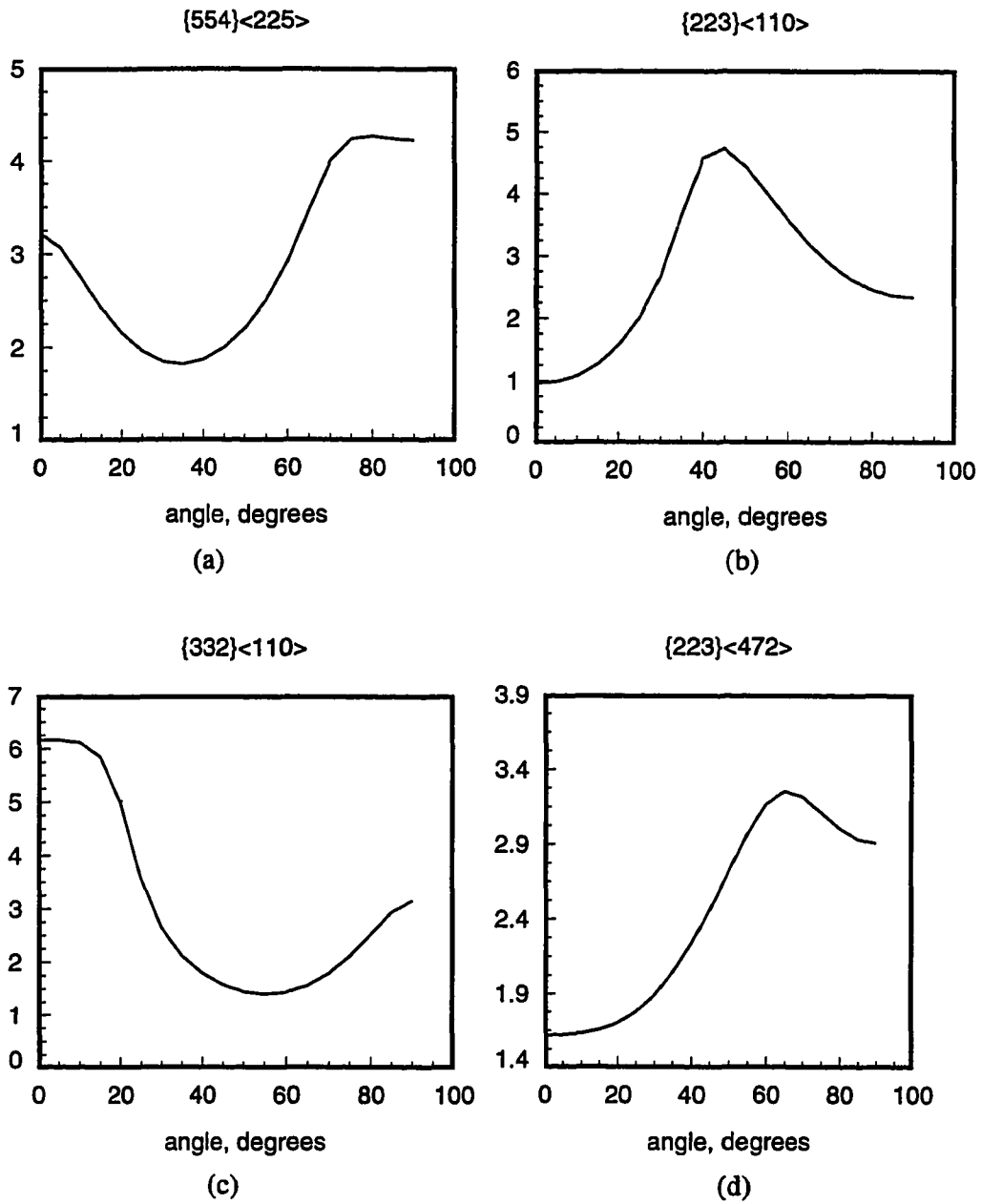
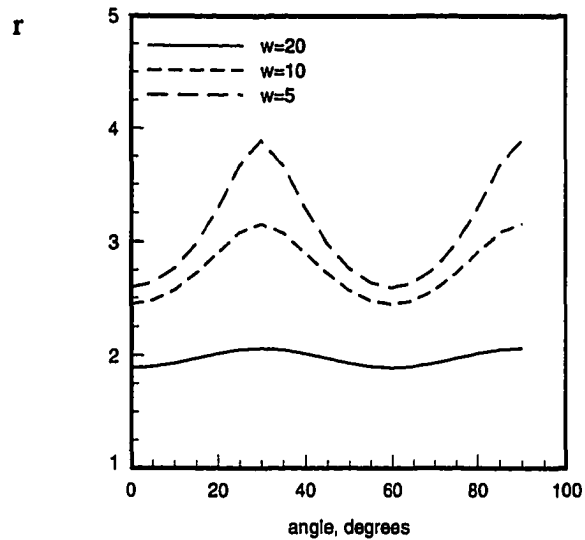


Fig. 5.30 Angular variation of r-values for simulated ideal secondary orientations

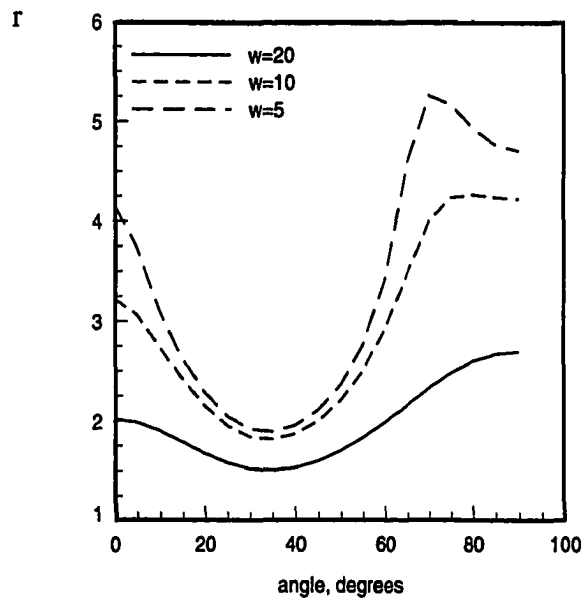
their  $\{111\}$  components and as Fig. 5.29a and b show, the  $\{111\}$  components show a 6-fold symmetry in their  $r$ -values every 60 degrees in the rolling plane.

Since the ultrasonic technique can only compute ODC's up to order 4, (i.e. it truncates the series expansion at  $W_{6mn}$  coefficients), it may lose important information regarding the plastic properties of these steels. In order to investigate this possibility, use of the Gaussian spread,  $\omega$ , in simulations of the plastic properties of ideal orientations may be useful. As mentioned earlier, the Gaussian spread is used to take into account the normally occurring misorientation of grains in simulation of ideal texture components in Eqn. 5.6. The smaller this value, the sharper the texture of the single ideal components. Figures 5.31a and b show the planar anisotropies of  $r$ -values of two texture components,  $\{111\}\langle 110\rangle$  and  $\{554\}\langle 225\rangle$  at three different Gaussian spread values of 5, 10 and 20 degrees. It can be seen that as the texture becomes sharper, the planar anisotropy of the  $r$ -value also becomes sharper with sharper peaks and corners. Therefore, it is conceivable, that as the real textures of the steels become sharper (e.g. textures in IF steels relative to, say, HSLA steels which have weaker textures), the series expansion may indeed need higher order terms (i.e.  $W_{6mn}$  or  $W_{8mn}$ ) to obtain a better convergence in its approximation of the properties.

In order to quantitatively test the effects of early truncation of higher order texture coefficients on the series expansion technique, the  $r$ -values of four ideal components  $\{111\}\langle 110\rangle$ ,  $\{100\}\langle 001\rangle$ ,  $\{554\}\langle 225\rangle$  and  $\{223\}\langle 472\rangle$  (which are all found in IF and other deep drawing steels) were calculated using the corresponding ideal ODC's up to and including the 8th order terms (Table. 5.7 and 5.8). Then the higher order terms were successively truncated: 8th order first, then 6th and finally the calculations included only the 4th order terms. Table 5.13 shows the numerical results for all the four ideal components. Here, it can be seen that truncation of the 8th order terms is not important at all, probably due to their smaller absolute values relative to the 4th and 6th order coefficients. While the effects



(a)



(b)

Fig. 5.31 Simulation of effects of sharpening the texture on r-value predictions

(a)  $\{111\}\langle 110\rangle$

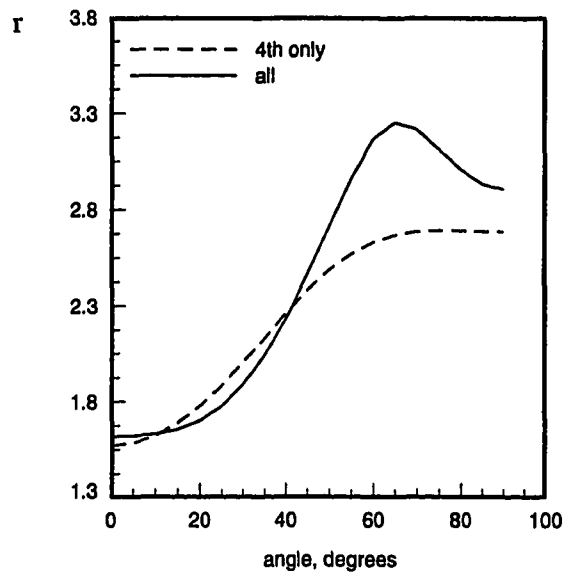
(b)  $\{554\}\langle 225\rangle$

of losing 6th order terms on  $\bar{r}$  is not very large ( from 0.03 in {554}<225> components to 0.2 in {100}<001> components), the effects on  $\delta r$  are larger (0.17 in {223}<472> components to  $\sim 1.1$  in {554} components). The change in  $\Delta r$  is even smaller except for the {100}<001> component ( $\sim 0.45$ ). Figures 5.32a and b show the effects of truncations of the 6th order terms on the shape of the planar anisotropy of r-values in the two components {554}<225> and {223}<472>. It is evident that while the level of normal anisotropy may not have changed significantly, the predictions based on only the 4th order terms 'miss' the sharp peaks or corners of the variations of r-values (particularly with respect to the {223}<472> components).

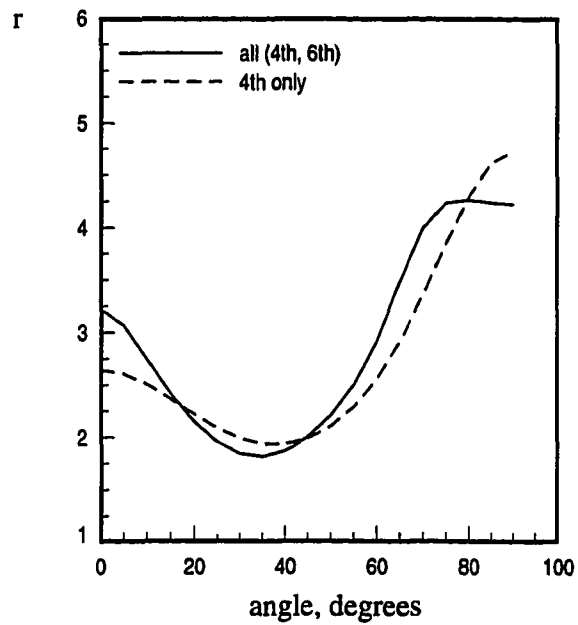
These results, therefore, indicate that while the 8th order terms are not important, the 6th order terms may be needed in order for the series expansion technique to make better predictions of the planar anisotropy (including  $\delta r$ ), and to a lesser extent, their normal anisotropy as indicated by  $\bar{r}$ .

Table 5.13 The effects of truncation of 6th order coefficients on predictions

Texture Component	$\bar{r}$	$\Delta r$	$\delta r$
{111}<110	2.76 (4th,6th, 8th)	0.007	0.707
	2.76 (4th, 6th)	0.007	0.707
	2.69 (4th only)	0.000	0.000
{554}<225>	2.86	1.720	0.990
	2.86	1.720	0.990
	2.83	1.690	2.080
{223}<472>	2.36	-0.200	1.286
	2.36	-0.200	1.286
	2.25	-0.254	1.115
{100}<001>	0.40	0.743	0.000
	0.40	0.743	0.000
	0.21	0.295	0.000



(a)



(b)

Fig. 5.32 Simulation of effects of early truncation on r-value predictions

(a)  $\{223\}\langle 472\rangle$

(b)  $\{554\}\langle 225\rangle$

#### 5.9.4 Comparison of the Experimental $r$ -value Predictions with Tensile Results

Figures 5.33a-c show the comparison of the predicted  $\bar{r}$  with those obtained by the tensile tests. The solid lines represent a perfect fit between the predicted results and the tensile data. The dashed lines are the lines of error that have traditionally been observed to be associated with tensile tests. As stated in Chapter 3, the best experimental error of  $\pm 0.2$  for  $r$ -values equal to 2 is realistic. However, the actual observed errors (i.e. variations seen from the data reported by various laboratories) can be larger. Based on these considerations, it was decided to adopt the usual reported error (listed in a NAADRG study reported in reference (60)) of  $\pm 0.1-0.2$  in this study.

Figure 5.33a shows the  $\bar{r}$  results obtained by the RC model and the Mould-Johnson correlation. It is evident that the data obtained by using the RC model is in good agreement with the tensile results. Although all the data (except for 4 samples BH5, IF8, 9 and 10) are within the error bands of the tension tests, most of the disparity with the tensile data was observed in the IF samples. Table 5.14 also lists the numerical data. The Mould-Johnson correlation seems to systematically underestimate by a margin that is not acceptable, particularly for the IF samples. Figure 5.33b shows the results obtained when the ODC's are inferred from the diffraction technique (using the RC model with 4th order coefficients only). These results were obtained on 10 samples (IF2, 5, 6, 8, 9 and 10, AKDQ2, BH5, HS1 and HSLA1). Here it can be seen that the agreement between the diffraction and ultrasonics results is quite good which is expected since their measured 4th order coefficients were very close. Figure 5.33c shows the diffraction-measured  $\bar{r}$ 's with the 6th order coefficients included. It appears that the inclusion of the 6th order terms has improved the predicted  $\bar{r}$ 's (on all of the 4 mentioned samples except for IF9) to the extent that they are in better agreement with the tensile data. This increase in  $\bar{r}$  relative to the  $\bar{r}$  predicted on the basis of the 4th order ODC's measured by the diffraction technique, is  $\sim 0.1-0.15$  in all steels (see Table

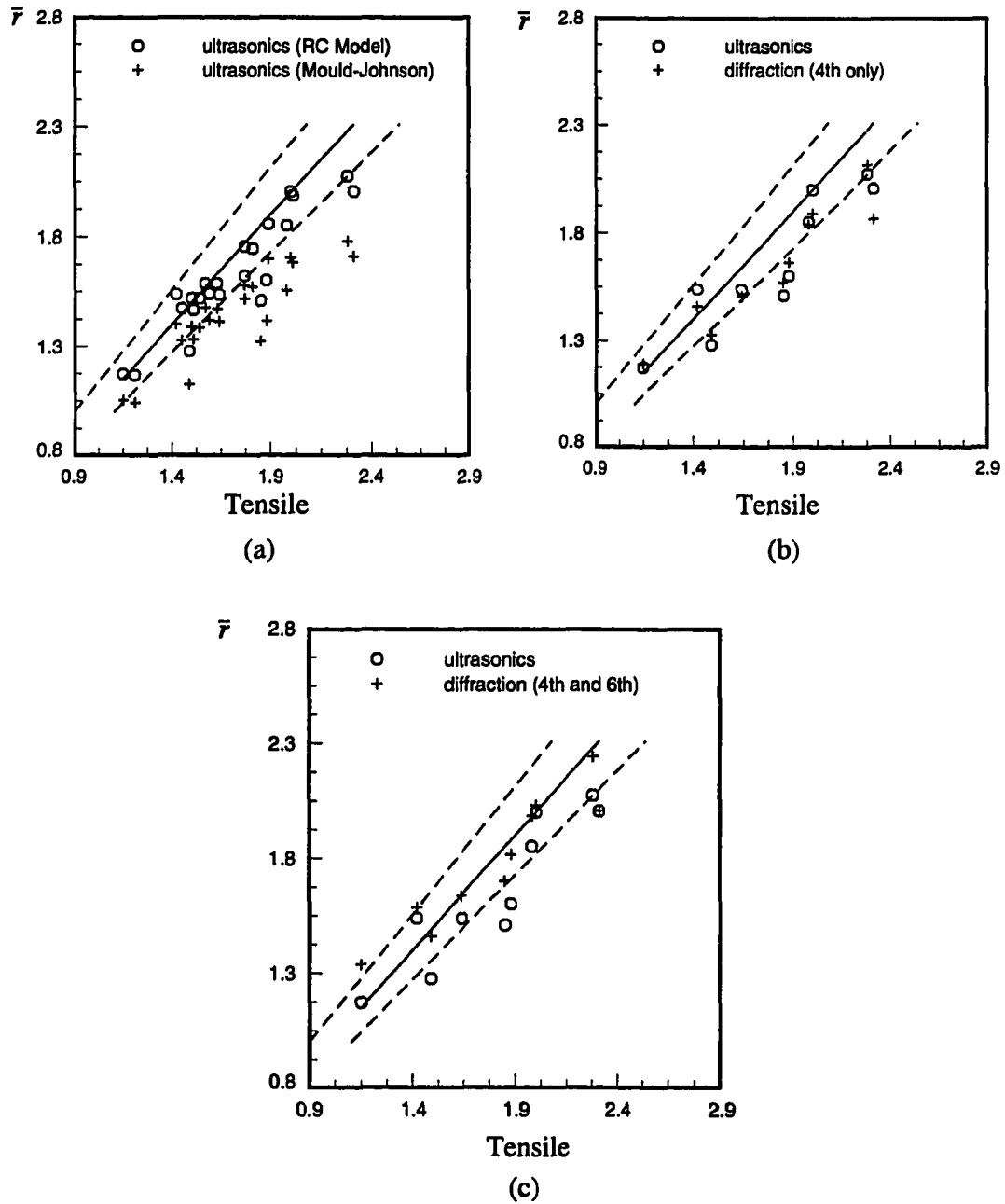


Fig. 5.33 Experimental predictions of  $\bar{r}$  by ultrasonics, diffraction and tensile  
 (a) Ultrasonics and tensile on all the samples  
 (b) Ultrasonics, 4th order diffraction and tensile  
 (c) Ultrasonics, 4th and 6th order diffraction and tensile

Table 5.14 Experimental predictions of  $\bar{r}$ 

		Predictions			
Grade	Tensile	Ultrasonics (RC Model)	Ultrasonics (Mould-Johnson)	Diffraction (4th only)	Diffraction (4th and 6th)
IF1	1.89	1.85	1.70	*	*
IF2	2.28	2.07	1.78	2.11	2.24
IF3	2.00	1.98	1.68	*	*
IF4	1.77	1.75	1.58	*	*
IF5	2.00	2.00	1.70	1.89	2.03
IF6	1.98	1.85	1.55	1.84	1.98
IF7	1.81	1.75	1.57	*	*
IF8	1.85	1.51	1.32	1.57	1.70
IF9	2.31	2.00	1.71	1.87	2.00
IF10	1.88	1.60	1.42	1.66	1.82
AKDQ1	1.63	1.59	1.47	*	*
AKDQ2	1.42	1.54	1.40	1.46	1.59
AKDQ3	1.50	1.52	1.39	*	*
AKDQ4	1.45	1.47	1.33	*	*
AKDQ5	1.54	1.52	1.39	*	*
BH1	1.57	1.59	1.48	*	*
BH2	1.59	1.54	1.42	*	*
BH3	1.77	1.62	1.52	*	*
BH4	1.21	1.17	1.04	*	*
BH5	1.49	1.28	1.13	1.33	1.46
HS1	1.64	1.54	1.41	1.51	1.63
HS3	1.51	1.47	1.33	*	*
HSLA1	1.15	1.17	1.05	1.19	1.34
HSLA2	*	1.04	0.95	*	*

5.14) which is of the same order of magnitude as the results of those simulations (an increase of  $-0.07$  to  $0.11$  from  $\{111\}\langle uvw \rangle$  to  $\{223\}\langle 472 \rangle$  components) shown in Table 5.13 of the previous section. The data on sample IF9, however, did not improve which confirms the fact that the tensile data on this sample may be an outlier (See Section 5.7 on the experimental correlation data).

Figures 5.34a-c show  $\Delta r$  data obtained by ultrasonics and diffraction methods (with 4th only and 4th and 6th order coefficients) and their comparisons with the tensile measurements. As with the previous plots, the solid lines pertain to a perfect fit between the tensile data and predictions, while the dashed lines point to the observed errors in tensile measurements of  $\Delta r$ . A simple propagation of error shows that this error is actually twice as large as the error in  $\bar{r}$ . This is due to the particular functional form of this parameter. Therefore, for an error of  $\pm 0.1-0.2$  in  $\bar{r}$ , the error in  $\Delta r$  is about  $\pm 0.2-0.4$ . Here, again, the observed error of  $\pm 0.3$  which is reported in reference (60) was used.

Examination of Fig. 5.34a shows that generally a good agreement exists between the RC model predictions of  $\Delta r$  and tensile data. Again, despite small differences between the tensile measurements, most of the disparity is seen in the IF data (see Fig. 5.34a in the 0-0.5 range). Also of interest here is the good agreement between the Mould-Johnson correlation predictions and the RC model and the tensile data. Table 5.15 shows that this correlation's predictions are also in very good agreement with the 4th order diffraction data. This is in sharp contrast with data shown in Fig. 5.33a where the correlation showed a consistent underestimation of  $\bar{r}$ . This is probably due to the differences between the chemical compositions of the original set of steels on which the Mould-Johnson correlation was obtained (late sixties) and the present set of steels used in this study. The differences in chemical composition affect the elastic constants which in turn affect the ultrasonic predictions of normal anisotropy much more than the ultrasonic predictions of the planar anisotropy (i.e.  $W_{400}$  as

---

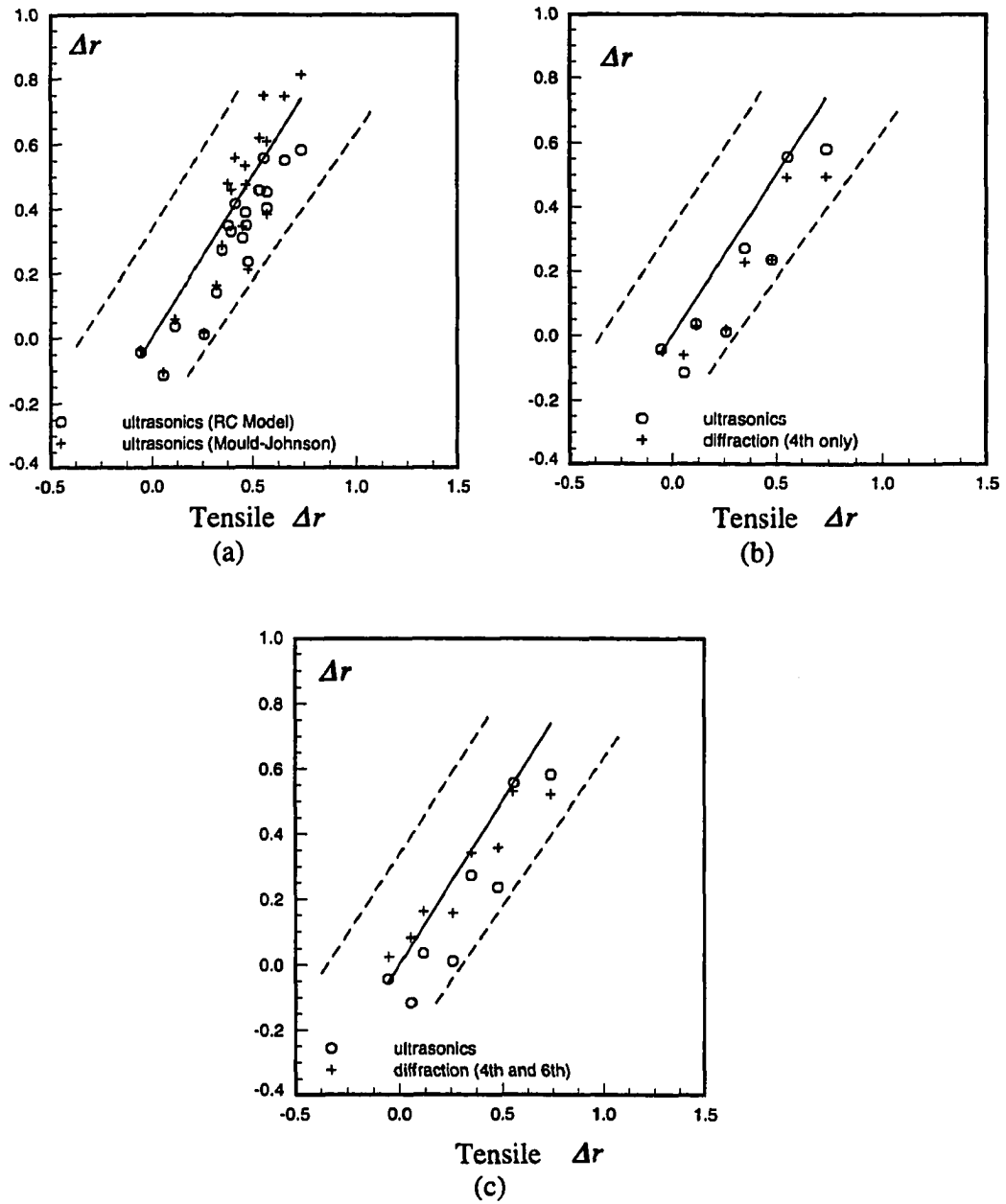


Fig. 5.34 Experimental predictions of  $\Delta r$  by ultrasonics, diffraction and tensile  
 (a) Ultrasonics and tensile on all the samples  
 (b) Ultrasonics, 4th order diffraction and tensile  
 (c) Ultrasonics, 4th and 6th order diffraction and tensile

Table 5.15 Experimental predictions of  $\Delta r$ 

		Predictions			
Grade	Tensile	Ultrasonics (RC Model)	Ultrasonics (Mould-Johnson)	Diffraction (4th only)	Diffraction (4th and 6th)
IF1	0.50	0.31	0.34		
IF2	0.48	0.24	0.21	0.24	0.36
IF3	0.56	0.40	0.38		
IF4	0.32	0.14	0.16		
IF5	0.06	-0.11	-0.10	-0.06	0.08
IF6	0.30	0.27	0.28	0.23	0.34
IF7	*	0.05	0.07		
IF8	*	0.24	0.30	0.14	0.20
IF9	0.26	0.01	0.01	0.01	0.15
IF10	0.11	0.03	0.05	0.03	0.16
AKDQ1	0.56	0.45	0.60		
AKDQ2	0.55	0.56	0.75	0.49	0.53
AKDQ3	0.46	0.39	0.53		
AKDQ4	0.65	0.55	0.75		
AKDQ5	0.53	0.46	0.62		
BH1	0.46	0.35	0.47		
BH2	0.38	0.35	0.48		
BH3	0.41	0.42	0.56		
BH4	*	0.38	0.56		
BH5	0.74	0.58	0.81	0.50	0.52
HS1	0.53	0.36	0.49	0.32	0.38
HS3	0.39	0.33	0.45		
HSLA1	-0.04	-0.04	-0.03	-0.05	0.02
HSLA2	*	-0.23	-0.33		

opposed to  $W_{420}$  and  $W_{440}$ ). As the data in Section 5.8.2 showed (see Fig. 5.19a), the effects of these variations in elastic constants on ultrasonic predictions of  $W_{400}$  is systematic and moves the  $\bar{r}-W_{400}$  curves up or down. Similarly, the  $\bar{r}-\bar{E}$  plots will move up or down depending on the differences in elastic constants caused by differences in chemical compositions. This is the reason why the data in Fig. 5.33a shows a consistent underestimation, while the data on the planar anisotropy predicted by the correlation is almost unaffected. This suggests that use of the original correlation by Mould and Johnson as a way of ultrasonically measuring  $\bar{r}$  should be avoided. The use of correlation in the Modul-r instrument as it is, however, is appropriate since the mentioned compositional variations are reflected in the values of Young's modulus which is measured experimentally by this instrument.

Inclusion of the 6th order terms whose results are shown in Fig. 5.34c, yields an improvement in the values of  $\Delta r$  which is similar to the improvement that was observed in  $\bar{r}$  - when these coefficients were included in the RC model. This change, which is approximately  $\sim 0.06$  to  $0.1$  (slightly higher than the results of simulations for all ideal components except for  $\{100\}\langle 001\rangle$  in Table 5.13) is more significant for IF samples than for the AKDQ2, BH5, HS1 and HSLA1 samples, where the latter actually exhibits a worsening effect. Similar trends can be seen in the  $\delta r$  data which are shown in Table 5.16 and Figs. 5.35a-c. Both the ultrasonic and the 4th order diffraction results show good agreement with the tensile data, while inclusion of the 6th order coefficients improves the results for almost all of the IF samples (particularly IF6). However, it seems to worsen the results on AKDQ2 and HSLA1 steels.

These results all indicate that although the differences between the 4th order ultrasonic data and tensile measurements are within the error range of the tensile tests, the conclusion may be inescapable that the addition of the 6th order coefficients has a general improving effect on almost all of the samples, particularly for the IF steels. While these improvements

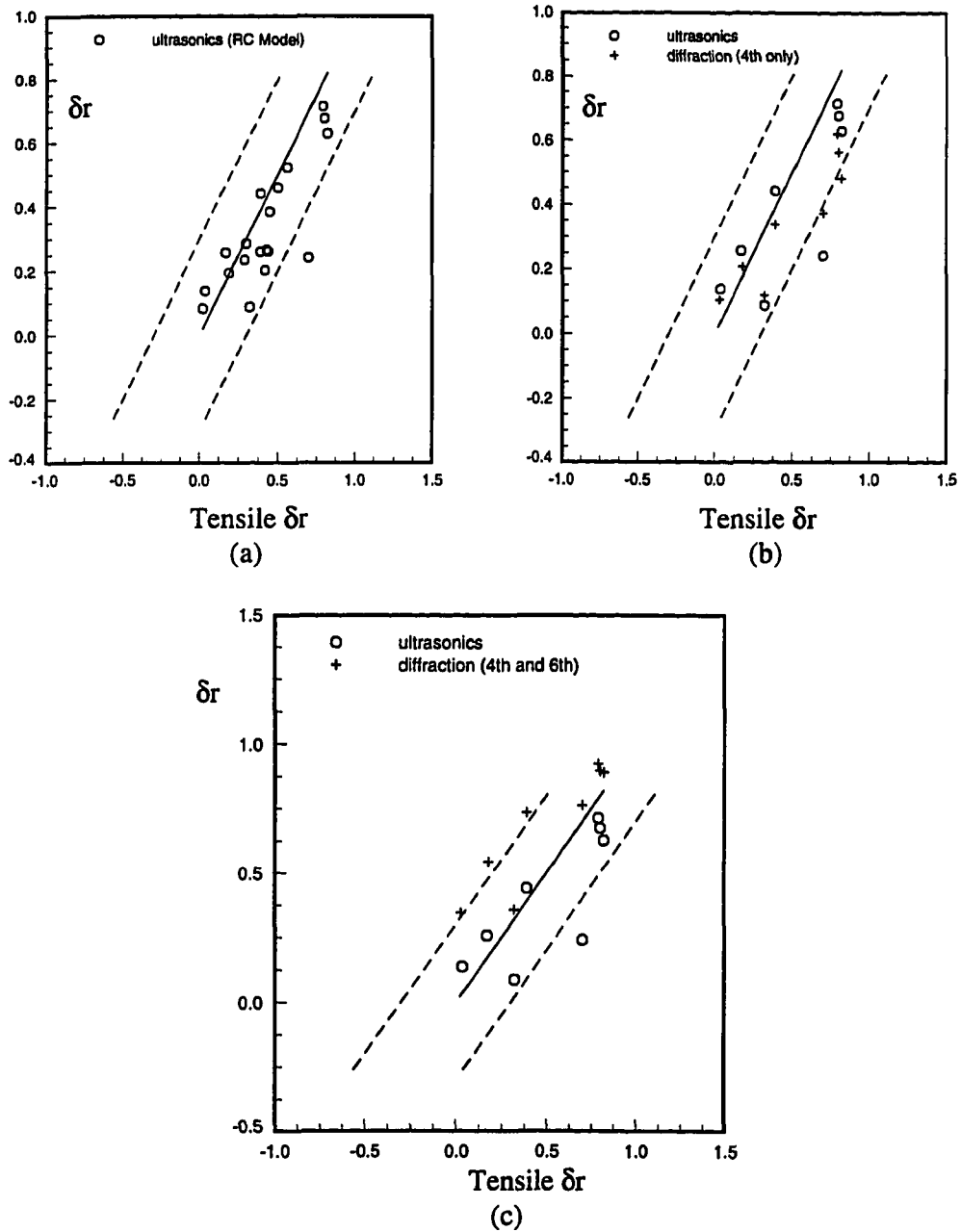


Fig. 5.35 Experimental predictions of  $\delta r$  by ultrasonics, diffraction and tensile  
 (a) Ultrasonics and tensile on all the samples  
 (b) Ultrasonics, 4th order diffraction and tensile  
 (c) Ultrasonics, 4th and 6th order diffraction and tensile

Table 5.16 Experimental predictions of  $\delta r$ 

		Predictions		
Grade	Tensile	Ultrasonics (RC Model)	Diffraction (4th only)	Diffraction (4th and 6th)
IF1	0.44	0.38		
IF2	0.80	0.68	0.56	0.90
IF3	0.50	0.46		
IF4	0.56	0.52		
IF5	0.79	0.71	0.62	0.92
IF6	0.70	0.24	0.37	0.76
IF7	*	0.41		
IF8	*	0.29	0.30	0.56
IF9	0.82	0.63	0.48	0.89
IF10	0.39	0.44	0.34	0.73
AKDQ1	0.41	0.20		
AKDQ2	0.03	0.14	0.10	0.35
AKDQ3	0.19	0.19		
AKDQ4	0.02	0.08		
AKDQ5	0.29	0.24		
BH1	0.30	0.29		
BH2	0.43	0.26		
BH3	0.42	0.27		
BH4	*	0.09		
BH5	0.32	0.08	0.12	0.36
HS1	*	0.24	0.21	0.47
HS3	0.38	0.26		
HSLA1	0.18	0.26	0.20	0.54
HSLA2		0.32		

are small (i.e.  $\sim 0.1-0.15$ ) and they are comparable to the errors associated with the tensile test, nevertheless, they do improve the agreements. The nature of these improvements can be seen in Figs. 5.36a-d where inclusion of  $W_{6mn}$  terms has led to a better fit between the predicted results and the tensile results on IF2, 5, 6 and BH5 samples. This is consistent with the results of simulations in the previous section (shown in Figs. 5.32a and b).

The reason for the opposite effect seen on HSLA1 and AKDQ2 steels is not clear. As Figs. 5.37a and b show, the inclusion of higher order coefficients has indeed worsened the fit for these steels. The increase in  $\bar{r}$  and  $\Delta r$  in the HSLA1 sample ( $\sim 0.15$  and  $0.07$ , respectively), although smaller, is consistent with the increase seen in the values for these properties when  $W_{6mn}$  are included for the ideal orientation  $\{100\}\langle 001\rangle$  which is dominant in these steels. The change in  $\delta r$  for both the HSLA1 ( $\sim 0.36$ ) and AKDQ2 ( $\sim 0.25$ ) samples is not consistent with the results shown in Table 5.13 for  $\{100\}\langle 001\rangle$  and  $\{554\}\langle 225\rangle$  components. Since diffraction data is only available on one sample from HSLA and AKDQ grades, it is difficult to generalize this worsening effect to these grades as a whole, especially since an improvement was seen for BH5 steel which has a texture comparable to that of AKDQ steels. The case with regard to data on IF9 may be more clear. As stated previously, the tensile data on this sample seems to be an outlier, and may be the result of systematic error in the tension test.

In order to investigate the effects of the  $W_{6mn}$  further, at this point, it may be useful to examine the relative weights of the individual 6th order coefficients based on their correlations with the plastic properties measured by the tensile test.

### 5.9.5 Correlations between $C_6^{\mu\nu}$ ( $W_{6mn}$ ) and Tensile Data

In order to investigate the relative importance of the individual 6th order coefficients (i.e.  $C_6^{11}$ ,  $C_6^{12}$ ,  $C_6^{13}$  and  $C_6^{14}$ ) the use of the ideal ODC's shown in Tables. 5.7 and 5.8 may

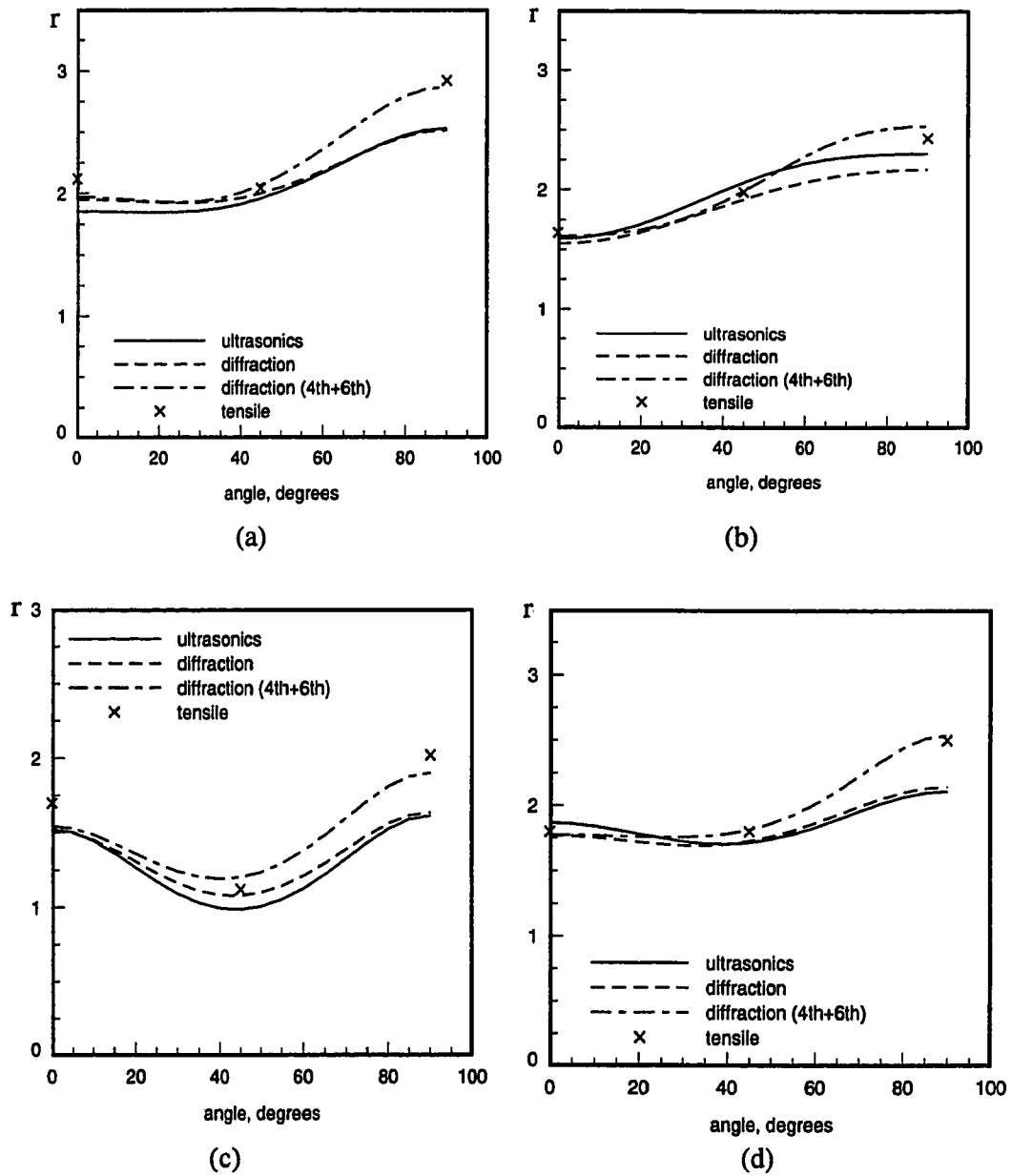
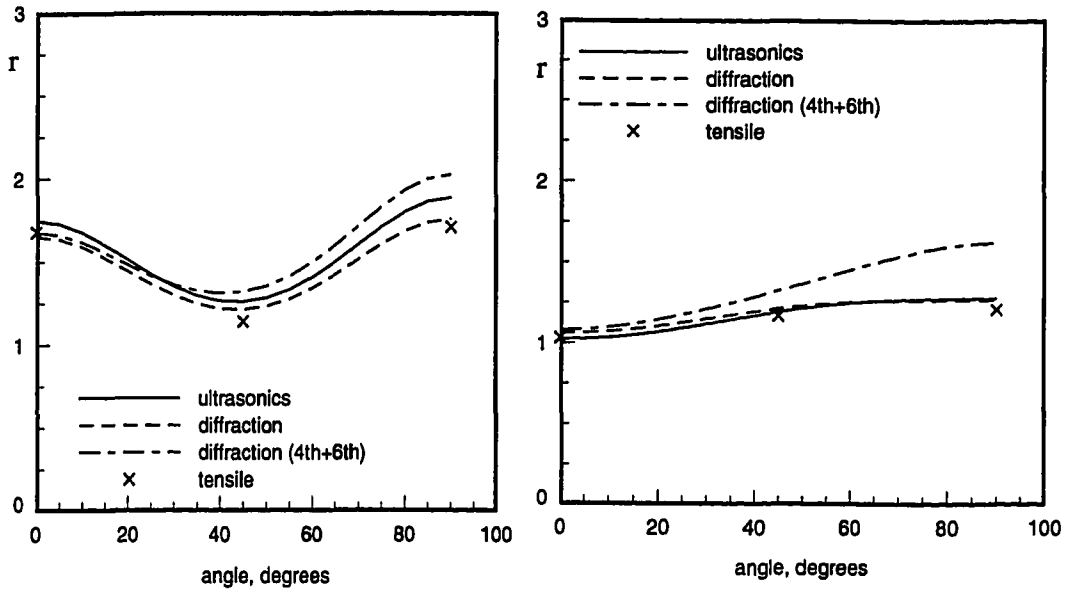


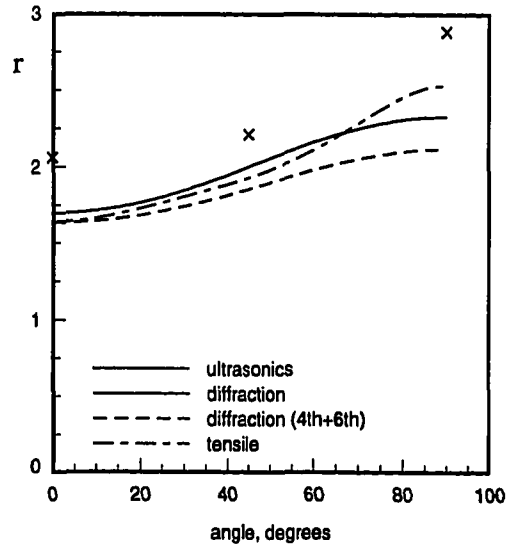
Fig. 5.36 Improvements in prediction of angular variation of  $r$ -values for

- (a) IF2
- (b) IF5
- (c) BH5
- (d) IF6



(a)

(b)



(c)

Fig. 5.37 The effects of 6th order coefficients on predictions of r-values for  
 (a) AKDQ2  
 (b) HSLA1  
 (c) IF9

be beneficial. Figure 5.38 shows the plot of  $C_6^{11} - C_4^{11} (W_{600} - W_{400})$  on the 10 steel samples examined by neutron diffraction. The solid line is the line of  $C_6^{11} - C_4^{11}$  corresponding to the ideal orientation {111} components (see Table. 5.7) with its slope being 1.5 (i.e.  $C_6^{11}/C_4^{11}=1.5$ ). The slope of the best-fit line through the measured data is about 1.42. Such a small difference between the slopes of the ideal line and the measured line indicates the strength of the {111} components in these steels which accounts for their near ideal textures. This is consistent with the findings by Sakata et al. (82) who observed almost identical trends on the 18 deep drawing quality steels that they studied. It is evident that the higher the volume fraction of the grains with {111} components, the larger is the experimental slope, and that this will be closer to that of the ideal line. The small difference that is seen between the slopes is probably due to the presence of other non-{111} components such as {100} components. In fact, the data for HSLA1 seems to be further from the ideal line than is the case for the rest of the steels, since its main texture components consist of {100} orientations. The data in Fig. 5.38 suggests that {111} components strongly contribute to the  $C_6^{11}$  coefficient, and since {111}<uvw> sets the level of normal anisotropy (i.e.  $\bar{r}$ ),  $C_6^{11}$  should correlate with this anisotropy as well.

Figure 5.39a confirms this suggestion where a strong correlation is observed between  $C_6^{11}$  and the  $\bar{r}$  as measured by the tensile test on the 10 samples examined. The correlation coefficient is 92% (1% significance level is 76.5%). Therefore,  $C_6^{11}$  is very similar to  $C_4^{11}$  in terms of its relation to the normal anisotropy. Although this is true for all of the steels, since 6 out of the 10 steels examined are IF samples,  $C_6^{11}$  may be more important in these steels than in the others. In fact the absolute value of this coefficient is generally higher in IF steels than in AKDQ2 or HSLA1 steels and it explains the improvement that was seen in  $\bar{r}$  for IF steels after the 6th order coefficients were included in the RC model. This is also in agreement with the results published in reference (82). The absolute value of  $C_6^{11}$  varied

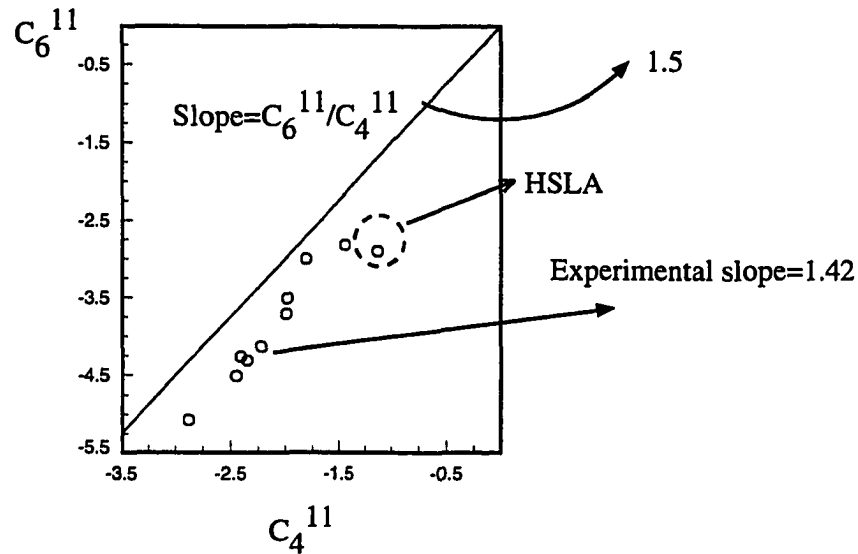


Fig. 38 Plots of  $C_6^{11}$ - $C_4^{11}$ , experimentally and ideally

from 3.71-5.07 for IF8 to IF2, as opposed to 2.90-3.51 in HSLA1 to HS1 steels within the 10 samples which were examined by neutron diffraction.

The other 6th order coefficients  $C_6^{12}$  and  $C_6^{13}$  show correlations with the tensile data, although these are less significant than for  $C_6^{11}$ . Figures 5.39b and c show the correlations between  $C_6^{12}$  and  $\Delta r$  and  $\delta r$ . The correlation coefficients are 79% and 72% (1% significance levels are 79.8 and 83.4%), respectively. As was the case for the effects of  $C_6^{11}$  on  $\bar{r}$ , the inclusion of  $C_6^{12}$  contributes to a better prediction of the planar anisotropy and anisotropy in the rolling plane,  $\delta r$ .  $C_6^{13}$ , whose magnitude is almost constant in these steels and falls in a narrow range between -0.4 to -0.7, shows a correlation only with  $\delta r$ , which is less significant than that of  $C_6^{12}$  (68%, where the 1% significance level is 83.4%).

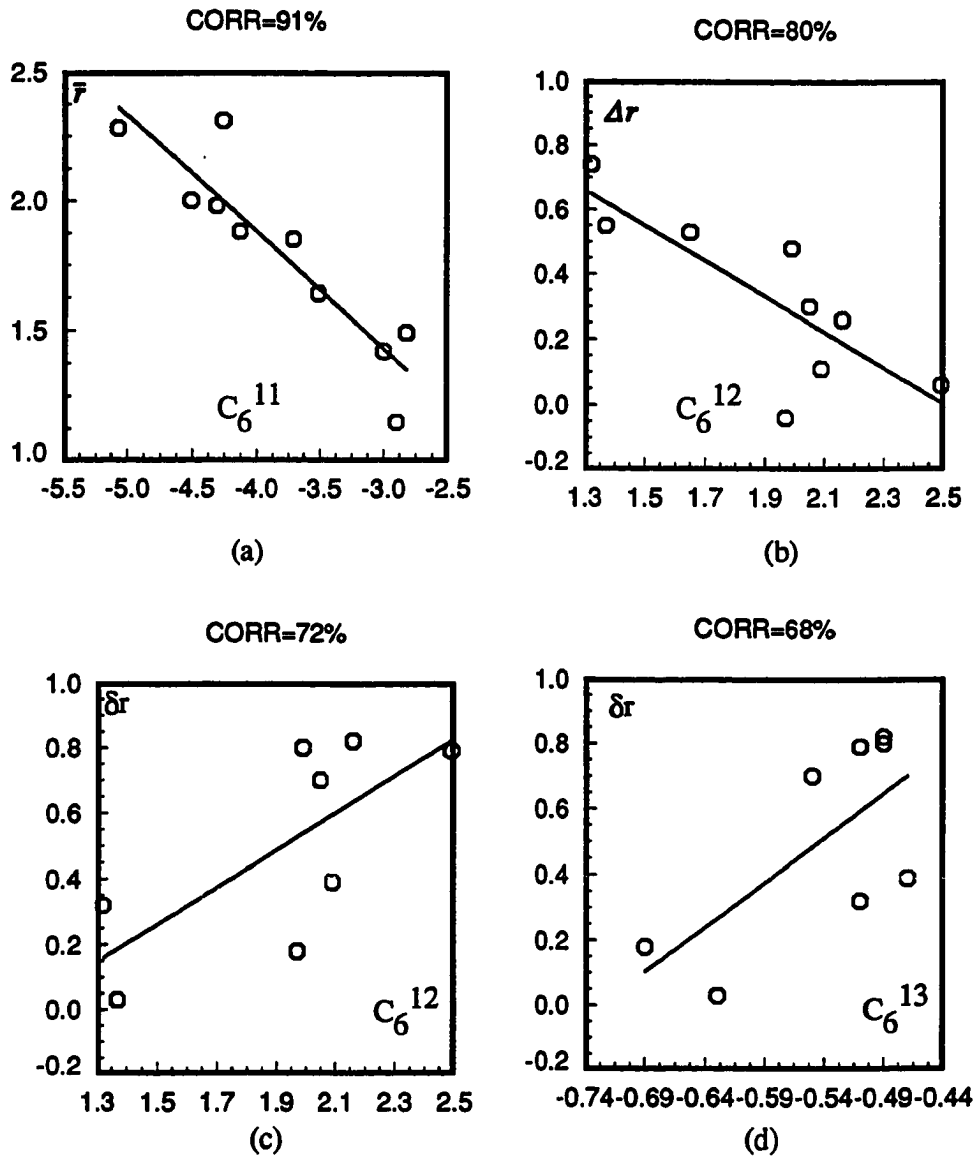


Fig. 5.39 The experimental correlations between 6th order coefficients and tensile data

(a)  $C_6^{11}$  -  $\bar{F}$

(b)  $C_6^{12}$  -  $\Delta r$  and (c)  $C_6^{12}$  -  $\delta r$

(d)  $C_6^{13}$  -  $\delta r$

$C_6^{14}$  shows no significant correlations at all with the tensile data. This coefficient is the smallest in the group particularly for non-IF samples (0.06 to -0.01 in AKDQ2 to HSLA1) although it is much larger for IF samples (-0.8-0.8 in IF5 to IF9). Lack of any significant correlation between  $C_6^{14}$  and the tensile data is somewhat surprising, since this coefficient is responsible for all of the angular variation of r-values corresponding to the  $\{111\}\langle uvw \rangle$  components. Examination of the ideal ODC's corresponding to the  $\{111\}\langle uvw \rangle$  in Table 5.7 shows that for these components, only  $C_6^{14}$  is non-zero and without it, r would essentially be constant in the plane of the sheet.

Nevertheless, the empirical data shown here indicate that only  $C_6^{11}$  and  $C_6^{12}$  (and to a lesser extent  $C_6^{13}$ ) correlate significantly with the plastic properties, and that they play the most important role in a better convergence of the series expansion technique. The effect of  $C_6^{14}$  is apparently small. However, since its magnitude is larger for IF steels, it may yet be needed, since the Taylor factors of the same order (i.e.  $m_6^{14}$ ) are probably still important in the analysis. Also of interest here is the good correlation between  $\bar{V}$  and  $W_{600}$  and  $\Delta V$  and  $W_{620}$  with correlations of 90 and 94% respectively (1% significance for these two is 83.4%), as shown in Figs. 5.40a and b. The good correlations here indicate that there is an empirical basis for future efforts to expand the EMAT technology so as to empirically include the effects of these two parameters ultrasonically.

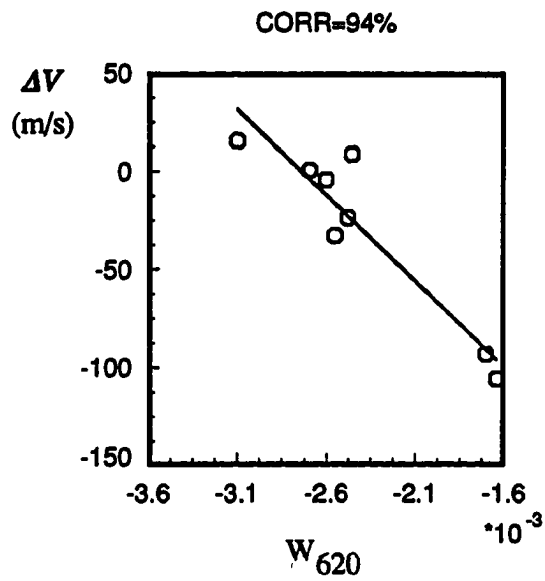
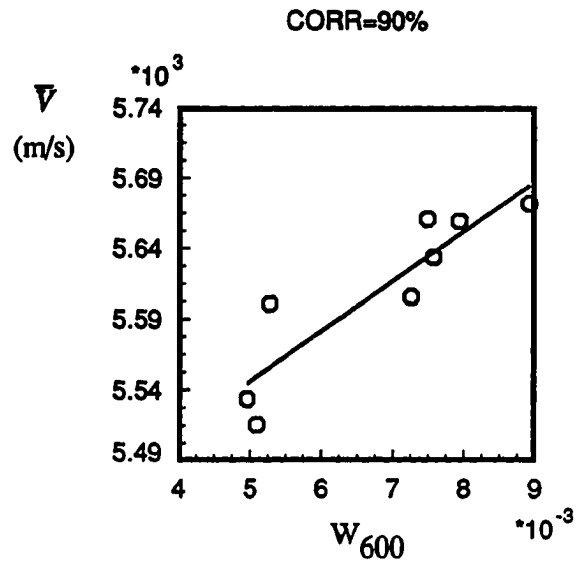


Fig. 5.40 The experimental correlations between ultrasonic velocity and 6th order coefficients: (a)  $W_{600} - \bar{V}$   
(b)  $W_{620} - \Delta V$

## CHAPTER 6

### CONCLUSIONS

As stated in Chapter 1, the major objective of the present study has been to investigate the capabilities and accuracy of the present ultrasonic instrument, Ultra-Form, in a more controlled manner than was done previously as reported in reference (2). In addition to the industrial interest in pursuing future development of an on-line nondestructive measurement of  $r$ -values, this work was primarily motivated by the desire to further explain the agreement which was obtained between the ultrasonic data and the traditional tensile test data which were taken in 1990 (Fig. 1.8). This agreement was excellent for steels with  $\bar{r}$ -values less than 1.8, but the ultrasonic data gave systematically lower values for steels with  $\bar{r}$ 's greater than 1.8. A number of candidate explanations of this data were considered. These included: 1) Inadequacies of the experimental correlation of Mould and Johnson or alternatively, lack of a suitable deformation model that can use ultrasonic information as input, 2) Limitations of ultrasonics in quantifying crystallographic texture and its lack of sensitivity to the particular texture of high  $r$  steels due to the truncation of texture coefficients of 6th order and higher, 3) Limitations and errors inherent in traditional tensile tests, 4) Lack of reproducibility of ultrasonic measurements in the observed  $r$  range due to an instrumentation inaccuracies.

In order to determine the relative importance of the aforementioned factors, four major areas were chosen for consideration: 1) The accuracy and reproducibility of ultrasonic measurements, 2) The sensitivity of these measurements to the microstructure of the steel sheets (texture), 3) The factors affecting the relative value of the ultrasonic predictions of plastic properties, 4) The comparison of an alternative deformation model to that of the empirical

correlations of Mould and Johnson (Eqns. 1.8 and 1.9), which had previously been used to predict  $r$ -values(2).

Towards this end, experimental research study was conducted which included ultrasonic measurements of velocities on 26 lifts of commercially produced drawing quality, low carbon steels (10 per lift leading to ~260 measurements total, on samples 20 x 20 in. ( 50 x 50 cm) cut out of each lift). The experimental investigations also included tensile measurements on the steels (one per lift) and neutron diffraction measurements (one per lift for 10 selected lifts). Theoretical research was conducted to investigate various plastic deformation models reported in the literature, which have been used to predict plastic properties from diffraction or ultrasonic data as input. The theoretical investigation also included gaining an improved understanding of the forming process as viewed by industry (i.e. the auto and steel industries) and the problems of where the ultrasonic technique can be of advantage. The following sections present the general conclusions drawn from the results of these investigations which were described in Chapters 1-5 of this thesis.

### **6.1 The Accuracy and Repeatability of Ultrasonic Measurements**

The repeatability data (presented in Section 5.6, Chapter 5) point to an excellent electromagnetic coupling that exists between EMAT transducers and the sheets (a typical repeatability error in velocity measurements was 0.01% with 95% confidence). In terms of the future on-line usage of EMAT's, this data is promising. Moreover, the observed uncertainties in predicted  $r$ -values (which are due to the inherent electronic error in Ultra-Form) are smaller (~ 0.2% in average  $r$  with 95% confidence) than the variations of properties throughout the lifts which the ultrasonic technique predicted (~0.4 to 0.8%). These variations are due to the nonuniformities of the texture which is caused by the roll milling process itself. Again, this points to a good sensitivity of the ultrasonic technology in detecting small

changes in texture which is important from the perspective of an on-line control of plastic properties.

From an operational standpoint, the ultrasonic technique provided a convenient method for measuring properties rapidly. The time involved in measuring properties throughout the lifts was approximately 30-40 minutes per lift (leisurely). Considering the man-hours involved in conducting a tension test, the significance of this savings in time can be appreciated only by those who are involved in the routine quality control checks of r-values in industrial laboratories. The signal processing technique employed in Ultra-Form proved to be quite sound, although the frequency selection routine (Eqn 5.1 in Chapter 5) needs to be modified for sheets with sharper textures such as those of IF steels.

### 6.2 Sensitivity To the Microstructure (Texture)

The experimental correlations obtained between various ultrasonic parameters (i.e. velocity, texture coefficients) and the tensile parameters (tensile measurements of plastic properties) show significant correlation coefficients for all of the mentioned parameters as presented in Table 5.6 of Section 5.7 in Chapter 5. These data included correlations between parameters that indicate normal anisotropy ( $\bar{V}$ ,  $\bar{E}$ ,  $W_{400}$  and  $\bar{r}$ ) and parameters that indicate planar anisotropy ( $\Delta E$ ,  $W_{440}$  and  $\Delta r$ ). Of importance here is also the correlation between  $W_{420}$  and  $\delta r$ . The latter coefficient is more difficult to measure accurately since the difference between velocities at 0 and 90 degrees are small for sheets that show exhibit  $\delta r$  values (e.g. AKDQ steels). Similarly, previous error analysis of tensile measurements of r-values indicates that the error for  $\delta r$  is also large when determined by the tensile technique. In view of these error considerations (and the fact that the ultrasonic measurements are also not error-free), the significant correlation observed between  $W_{420}$  and  $\delta r$  is an important result.

Generally, however, all of these data indicate a good sensitivity of the ultrasonic technology to changes in the texture of the sheet. This was also observed in the repeatability data discussed in the previous section.

### **6.3 The Factors that Affect the Ultrasonic Predictions of Plastic Properties**

#### **6.3.1 Effects of Coatings**

The evidence presented by this study (Section 5.5.3), supports the fact that the effects of galvanizing on ultrasonic predictions of plastic properties (particularly  $\bar{\tau}$ ) is negligible. This conclusion is only true for the range of the coating thicknesses used here, 0.1-1.1 mils (0.002-0.02 mm), which is the typical range for automotive applications. Much larger thicknesses will require a correction scheme to compensate for the slowing effects of coatings on the ultrasonic velocities.

#### **6.3.2 Effects of Accurate Set of Elastic Constants**

By far the most important factor that affects the ultrasonic predictions of plastic properties is the accuracy of the set of elastic constants to be employed in the calculations (Eqn. 4.19). These should be indicative of the chemical composition of the steels whose properties are to be measured. With regard to this matter, the data presented in Section 5.8.2 indicate that of all the texture coefficients, the ultrasonic prediction of  $W_{400}$  is most sensitive to the variations among the reported sets of elastic constants (which are caused by variations in chemical composition of single crystals and differences in experimental procedures used by various sources) in the literature. Since this parameter correlates strongly with the normal

---

anisotropy, ultrasonic predictions of  $\bar{r}$  and  $\bar{E}$  will be affected the most. The prediction of  $\bar{E}$ , however, exhibits a less sensitivity to these variations than that of  $\bar{r}$ . The reason for this is that the change in  $\bar{E}$  is offset by a larger (simultaneously opposite) change in the ultrasonic calculation of  $W_{400}$ . The error in the ultrasonic  $\bar{r}$  can be significant, (as much as 0.54). The results of this work indicate that an experimental measurement of the current elastic constants of the material under ultrasonic investigation should be performed in advance. Independent experimental measurements of Young's modulus (by Modul-r instrument) and texture coefficients (by X-ray diffraction technique) seem to be an excellent way of achieving this goal as was reported in reference (61).

### 6.3.3 Effects of Early Truncation of Higher Order ODC's

The prediction of elastic properties such as Young's modulus (by the series expansion technique) is only sensitive to the 4th order coefficients (i.e.  $W_{4mn}$ ). The reason for this lies in the fact that the truncation of the series expansion of elastic properties depends on the rank of the elastic constant tensor, which is 4, and thus the truncation is exact at this level. However, for the case of plastic properties, in addition to the 4th order ODC's, the 6th order coefficients also affect the predictions of  $\bar{r}$ ,  $\Delta r$  and  $\delta r$ . The results of simulations of ideal texture components (Table 5.13, Section 5.9.3) show that although the effects of inclusion of the 6th order coefficients in the calculations is relatively small (e.g. 0.1-0.2 in  $\bar{r}$ ), these do improve the predictions of the series expansion technique for both the normal anisotropy as well as the planar anisotropy. Empirical data obtained using ultrasonics and neutron diffraction confirm the results of simulations, particularly for IF steels. The latter are quite consistent with the fact that the sharpness of texture in these steels (due to their particular processing practices) requires for more ODC's to be included in the calculations in order to provide

a better description of the anisotropy of their texture-dependent properties.

The empirical data obtained in this study demonstrate that the coefficient  $W_{600}$  correlates well (91% correlation coefficient) with the tensile measurements of  $\bar{r}$  and that it is essentially responsible for all the improvements obtained in the prediction of this parameter (when the 6th order coefficients are included).  $W_{620}$  also correlates well with  $\Delta r$  and  $\delta r$  and thus contributes to a better prediction of the planar anisotropy of the r-values (80% and 72% correlation coefficients respectively). The coefficient  $W_{640}$  exhibits only a weak correlation with  $\delta r$  (68%), while  $W_{660}$  shows no correlation at all with the tensile data, although its magnitude is larger for the IF steels than for any other steel studied. In terms of future measurements of 6th order coefficients by the ultrasonic technology, strong correlations exist between the diffracted measured values of  $W_{600}$  and the ultrasonic average velocity,  $\bar{V}$ , and the values of  $W_{620}$  and  $\Delta V$ , which is promising (90% and 94% correlation coefficients, respectively).

#### 6.4 Choice of Modeling in Ultrasonic Predictions of Plastic Properties

This is an important element in the accurate ultrasonic prediction of r-values. The series expansion-based, relaxed constraint model (60), which was used in this study provided a significant improvement over the empirical correlations of Mould and Johnson. One of its strengths lies in its ability to accurately take into account the empirical observations regarding the degree of competition between the pertinent glide planes in a mixed slip mode (between the {110} and {112} planes). This situation usually occurs during the deformation of the single crystals of bcc iron. The decision as to which glide plane is dominant during the slip process is carried out by selecting the proper stress ratio, (the CR factor). The results obtained from this study (Section 5.9.1.2) confirm the experimental findings reported in ref-

erence (61) where CR's of 0.95 and 1 worked well for IF steels where the relative lack of interstitials caused this factor to be larger than for the non-IF steels (CR of 0.9 worked well for the latter steels). Another advantage of this model is its ability to obtain the individual  $r$ -values (i.e. at 0, 45 and 90 degrees with respect to the rolling direction). Its predictions of properties proved to be quite close to the tensile data, generally within the error bands of the tension test (Section 5.9.4).

The results in this study indicate that the Mould-Johnson correlation (in its original functional form) should not be used for the ultrasonic prediction of  $\bar{r}$ . The reason is that the ultrasonic calculation of Young's modulus is sensitive to the accuracy of the elastic constants which in turn should be representative of the particular chemical composition of the steels under study. The original functional form of the Mould-Johnson correlation (i.e. Eqn. 1.8) was obtained on steels which had different chemical compositions and microcleanliness than those of the steels used in the present research (and thus different elastic constants). This is the reason for the fact that this correlation's predictions of  $\bar{r}$  when compared with those of the tensile measurements, shows a systematic underestimation of this parameter by a margin which is not acceptable (particularly for IF steels). This is also consistent with the results of the earlier study shown in Fig. 1.8 which goals has been one of the impetuses of the present study. This conclusion, however, does not state that the use of Eqn. 1.8, as it is, should be avoided when it is carried out in the Modul-r instrument. Unlike the ultrasonic technique, the  $r$ -value predictions by this instrument is insensitive to the effects of chemistry and microcleanliness of the steels.

**BIBLIOGRAPHY**

1. K. Kawashima, T. Hyogushi and T. Akagi, Journal Of Nondestructive Evaluation, 12 , 71 (1993).
  2. R.B. Thompson, D. D. Bluhm, G.A. Alers, K.Forouraghi, H.D. Skank and S.J. Wormely, Journal Of Nondestructive Evaluation, 12, 45 (1993).
  3. A.V. Clark, N. Izvorski, Y. Berlinsky, Y. Cohen, and D.V. Mitrakovic, and S.R. Schaps, Journal Of Nondestructive Evaluation, 12, 33 (1993).
  4. M. Hirao, H.Fukuoka, K.Fujisawa, and R.Murayama, Journal Of Nondestructive Evaluation, 12, 27 (1993).
  5. M. Borsutzki, C. Thoma, W. Bleck and W. Theiner, Stahl u. Eisen, 113, 93 (1993)
  6. H. J. Kopineck, R. Loffel and H-B. Otten, Journal Of Nondestructive Evaluation, 12 , 13 (1993).
  7. H. Richter and H. W. Tamler, Applied Technology, 46 (1994).
  8. R. Joshi, F. Hatt and D. Lefebvre, Proceedings of International Body Engineering Conference, IBEC (94): Advanced Technology and Processes, 10 12 (1994).
  9. J. R. Newby, STAMPING DESIGN thru MAINTENANCE, Society of Manufacturing Engineers, Dearborn, MI (1983).
  10. S. P. Keeler, MECHANICS OF SHEET METAL FORMING, Plenum Press, New York London, 1978.
  11. T. Leverton, A. Scoores, and M. Karima Proceedings of International Body Engineering Conference, IBEC (93): Body Assembly and Manufacturing, 99 (1993).
  12. W. F. Hosford and W.A. Backofen: Fundamentals of Deformation Processing, 9th Sagamore Conf. AMRA, Syracuse University Press, Syracuse, 259 (1964).
  13. Report of IDDRG (working Group 2), Sheet Metal Industries, 44, 523 (1967)
  14. P. G. Nelson and J. Winlock, Bulletin ASTM, 53 (1949).
  15. W. T. Lankford, S. C. Snyder and J. A. Bauscher, Trans. ASM, 42, 1197 (1950).
  16. D. J. Blickwede, Trans. ASM, 61, 653 (1968).
-

17. S. P. Keeler and W. A. Backofen, ASM Trans. Quart., 56, 25 (1963).
  18. M. Gensomer, Trans. ASM, 36, 30 (1946).
  19. D. V. Wilson and Y. A. Konnan, Acta. Met., 12, 617 (1964).
  20. B. I. Edelson and W. M. Baldwin, Jr., ASM Trans. Quart., 55, 230 (1962).
  21. W. B. Morrison, ASM Trans. Quart., 59, 824 (1966).
  22. P. B. Mellor and A. Parmor, MECHANICS OF SHEET METAL FORMING, Plenum Press, New York-London, 1978.
  23. R. L. Whiteley, Trans. ASM, 52, 154 (1960).
  24. R. L. Whitely, D. E. Wise and D. J. Blickwede, Sheet Metal Industries, 38, 349 (1961).
  25. R.L. Whiteley, and D. E. Wise, Flat Rolled Products III, Interscience, New York, 1962.
  26. M. Atkinson and I. M. Maclean, Sheet Metal Industries, 38, 349 (1961).
  27. Y. C. Liu and G.A. Alers, Trans. Met.Soc. AIME 236, 489 (1966).
  28. E.P.Papadakis, Trans. Met.Soc. AIME 236, 1609 (1966).
  29. C. A. Stickle and P.R. Mould, Met.Trans. 1, 1303 (1970).
  30. P.R. Mould and T.E. Johnson,Jr, Sheet Metal Industries, 328 (1973).
  31. R. J. Roe, J.Appl.Phys. 31, 2069 (1966).
  32. H.J.Bunge, Mathematische Methoden der Texturanalyse, Akademie-Verlag, Berlin, 1969.
  33. G. T. Davies, D.J. Goodwill and R.S. Kallend, Met.Trans.3, 1677 (1972).
  34. R. B. Thompson, J. F. Smith and S.S.Lee in NDE of Microstructure for Process Control, ASM, Metals Park, 7, 1985.
  35. G.A. Alers, B.R. Tittmann and R.B. Thompson, unpublished results.
  36. R. B. Thompson, S. S. Lee and J. F. Smith, Ultrasonics, 25, 133 (1987).
  37. R. B. Thompson, S. S.Lee, J. F. Smith and G. C. Johnson, Met.Trans., 20A, 243 (1989).
-

38. M.Hirao, H. Fukuoka, K.Fujisawa and R.Murayama in Elastic Waves and Ultrasonic Nondestructive Evaluation, (North-Holland, Amsterdam, 319, (1990).
  39. R. Murayama, K. Fujisana, H. Fukuoka, M. Hirao and S. Yonehara, Proc. IEEE Ultrasonic Symp 2, 1159 (1989).
  40. D. Daniel, K. Sakata and J.J. Jonas Iron and Steel Inst. Jap.Int., 31, 696 (1991).
  41. G. I. Taylor, J.Inst.Met., 62, 307 (1938).
  42. W. F. Smith, Structure and Properties of Engineering Alloys, McGraw-Hill, Inc. , New-York (1993).
  43. American Iron and Steel Institute, Guidelines for Automotive Applications, Committee of Sheet Steel Producers, Washington, DC.
  44. S. Mishra and C. Darmann, International Metals Reviews, 27, 307 (1982).
  45. W. B. Hutchinson, Proceedings of The 10th International Conference on Textures of Materials, ICOTOM, 10, 1 (1993).
  46. W. B. Hutchinson, International Metals Reviews, 29, 25 (1984).
  47. R. Pradhan, SAE Paper No. 910290, 1991.
  48. I. Kovch, T. Owens, R. Thompson, SAE Technical Paper, No. 900715, 1990.
  49. K. Araki, K. Nakaoka, M. Abe, N. Ohashi, Sheet Metal Forming and Energy Conservation, American Society of Metals, Metals Park, Ohio, 1976.
  50. W. B. Hutchinson, Sheet Metal Industries, 146 (1983).
  51. F. Reis, LTV Steel Company, private communications, 1993.
  52. S. Mishra, Transactions of The Indian Institute of Metals, 36, 106 (1983).
  53. D. B. Knorr, H. Weiland and J. A. Szpunar, Applied Technology, 32 (1994).
  54. W. A. Sands, Introduction to Crystallography, Benjamin, Inc. NewYork, 1969.
  55. W. B. Hutchinson, An Introduction to Textures in Materials, Chameleon Press Ltd., London.
-

56. H. J. Bunge and C. Esling, Quantitative Texture Analysis, Deutsche Gesellschaft fur Metallkunde, 1982.
  57. P. R. Morris and A. J. Heckler, Advances in X-ray Analysis, 11, 454 (1962).
  58. W. Bleck, R. Grobterlinden, U. Lotter and C. P. Reip, Steel Research, 62, 580 (1991).
  59. H. J. Bunge and W. T. Roberts, J. Appl. Cryst., 2, 116 (1969).
  60. D. Daniel, Ph. D. thesis, McGill University, 1989.
  61. D. Daniel and J. J. Jonas, Metall. Trans., 21, 331 (1990).
  62. R. H. Goodenow and J. F. Held, Metall. Trans., 1, 2507 (1970).
  63. J. L. Duncan, E. Coni and W. Johnson J. Aust. Inst. Met., 12, 127 (1967).
  64. J. S. H. Lake, D. J. Willis and H. G. Fleming Metall. Trans. A, 19A, 2805 (1988).
  65. Y.C.Liu. Metall. Trans. A, 14A, 1199 (1983)
  66. P. I. Welch, L.Ratke and H. G. Bunge, Sheet Metal Industries, 171 (1983).
  67. Annual Book of ASTM Standards, Vol 3.01, E 517 555 (1990).
  68. K. Yoshida and K. Miyauchi, MECHANICS OF SHEET METAL FORMING, Plenum Press, NewYork-London, 1978.
  69. J. S. H. Lake and J. T. Flanagan, J. Applied Metalworking, 4, 164 (1986).
  70. H. M. Ledbetter and R. P. Reed, J. Phys. Chem. Ref. Data, 2 531 (1973).
  71. R. Hill, Proc. Phys. Soc. LXV, A65, 349 (1952).
  72. G. Y. Chin, W. L. Mammel, Trans. Metallurg. Soc. AIME 245, 1211 (1969).
  73. C. M. Sayers, J. Phys., D15 2157 (1982)
  74. M. Hirao, K. Aoki and H. Fukuoka, J. Acoust. Soc. AM, 81 1434 (1987).
  75. C. S. Barret, Structure of Metals, McGraw-Hill, New York 1952.
  76. P. Franciosi, Acta Metall., 31 1331 (1983).
-

77. G. Y. Chin, Metallurgical Transactions, **3**, 2213 (1972).
78. M. Hirao, N. Hara and H. Fukuoka, J. Acoust. Soc. Am., **84**, 667 (1988).
79. Technical Guide to Bethlehem's EG Sheet, Bethlehem Steel Corporation, Bethlehem, Pa.
80. Y. Li, Ph. D. Thesis, Iowa State University, Ames, Iowa, 1990.
81. S. J. Wormley, K. Forouraghi, Y. Li, R. B. Thompson and E. P. Papadakis, in Review of Progress in Quantitative Nondestructive Evaluation, **9**, 951 (1990).
82. K. Sakata, D. Daniel and J. J. Jonas, Textures and Microstructures, **11**, 41 (1989).